

RD-A162 419

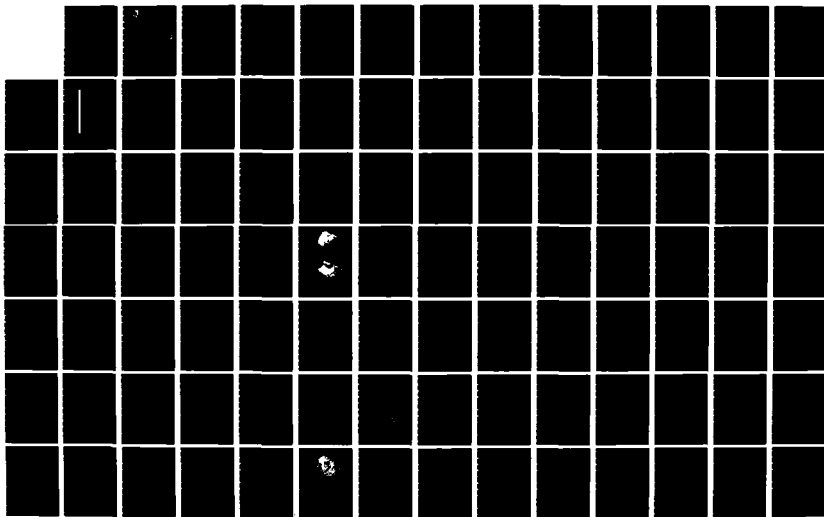
COASTAL AND INLET PROCESSES NUMERICAL MODELING SYSTEM
FOR OREGON INLET NORTH CAROLINA(U) COASTAL ENGINEERING
RESEARCH CENTER VICKSBURG MS S R VENULAKONDA ET AL
SEP 85 CERC-RR-85-6

1/2

UNCLASSIFIED

F/G 8/3

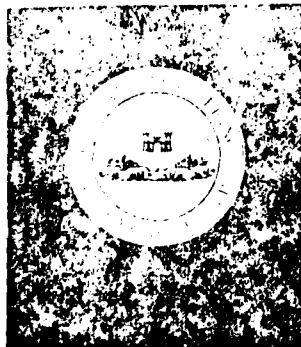
NL





US Army Corps
of Engineers

AD-A162 419



DTIC FILE COPY

TECHNICAL REPORT CERC-85-6

12

COASTAL AND INLET PROCESSES NUMERICAL MODELING SYSTEM FOR OREGON INLET, NORTH CAROLINA

by

S. Rao Vemulakonda, Abhimanyu Swain, James R. Houston
Paul D. Farrar, Lucia W. Chou, Bruce A. Ebersole

Coastal Engineering Research Center

DEPARTMENT OF THE ARMY
Waterways Experiment Station, Corps of Engineers
PO Box 631, Vicksburg, Mississippi 39180-0631

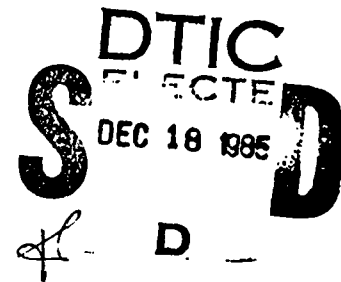


September 1985
Final Report

Approved For Public Release, Distribution Unlimited

Prepared for

US Army Engineer District, Wilmington
Wilmington, North Carolina 28402



85 12 17 111

Destroy this report when no longer needed. Do not return
it to the originator.

The findings in this report are not to be construed as an official
Department of the Army position unless so designated
by other authorized documents.

The contents of this report are not to be used for
advertising, publication, or promotional purposes.
Citation of trade names does not constitute an
official endorsement or approval of the use of
such commercial products.

Unclassified

SECURITY CLASSIFICATION OF THIS PAGE (When Data Entered)

REPORT DOCUMENTATION PAGE		READ INSTRUCTIONS BEFORE COMPLETING FORM
1. REPORT NUMBER Technical Report CERC-85-6	2. GOVT ACCESSION NO. AD-A162419	3. RECIPIENT'S CATALOG NUMBER
4. TITLE (and Subtitle) COASTAL AND INLET PROCESSES NUMERICAL MODELING SYSTEM FOR OREGON INLET, NORTH CAROLINA		5. TYPE OF REPORT & PERIOD COVERED Final report
7. AUTHOR(s) S. Rao Vemulakonda, Abhimanyu Swain James R. Houston, Paul D. Farrar Lucia W. Chou, Bruce A. Ebersole		6. PERFORMING ORG. REPORT NUMBER
9. PERFORMING ORGANIZATION NAME AND ADDRESS US Army Engineer Waterways Experiment Station Coastal Engineering Research Center PO Box 631, Vicksburg, Mississippi 39180-0631		8. CONTRACT OR GRANT NUMBER(s)
11. CONTROLLING OFFICE NAME AND ADDRESS US Army Engineer District, Wilmington PO Box 1890 Wilmington, North Carolina 28402		10. PROGRAM ELEMENT, PROJECT, TASK AREA & WORK UNIT NUMBERS
14. MONITORING AGENCY NAME & ADDRESS (if different from Controlling Office)		12. REPORT DATE September 1985
		13. NUMBER OF PAGES 110
		15. SECURITY CLASS. (of this report) Unclassified
		15a. DECLASSIFICATION/DOWNGRADING SCHEDULE
16. DISTRIBUTION STATEMENT (of this Report) Approved for public release; distribution unlimited.		
17. DISTRIBUTION STATEMENT (of the abstract entered in Block 20, if different from Report)		
18. SUPPLEMENTARY NOTES Available from National Technical Information Service, 5285 Port Royal Road, Springfield, Virginia 22161.		
19. KEY WORDS (Continue on reverse side if necessary and identify by block number)		
Coastal processes	Numerical models	Tides
Dredge disposal	Numerical simulation	Waves
Hydraulic structures--evaluation	Oregon Inlet (North Carolina)	Wave-induced
Hydrodynamics-mathematical models	Sediment transport	currents
Inlets	Storm surge	
20. ABSTRACT (Continue on reverse side if necessary and identify by block number)		
Oregon Inlet is a large tidal inlet through the barrier island system of North Carolina. In 1970, Congress authorized the Manteo (Shallowbag) Bay project which had provisions to stabilize Oregon Inlet with two jetties, deepen the ocean bar channel to 20 ft, and bypass across the inlet sand intercepted by the jetties. This report describes the results of a numerical study to consider coastal and inlet processes in the region surrounding the inlet under existing and planned project conditions. To accomplish the objectives of the study, a		

(Continued)

DD FORM 1 JAN 73 1473

EDITION OF 1 NOV 65 IS OBSOLETE

Unclassified

SECURITY CLASSIFICATION OF THIS PAGE (When Data Entered)

Unclassified

SECURITY CLASSIFICATION OF THIS PAGE(When Data Entered)

20. ABSTRACT (Continued).

system of numerical models called Coastal and Inlet Processes (CIP) Numerical Modeling System was developed. It included models for wave propagation, wave-induced currents and setup, sediment transport within and beyond the surf zone, and profile response (onshore-offshore transport). Results from a separate study on numerical simulation of tides and storm surge for Oregon Inlet were utilized in the present investigation.

As a test for an extreme event, the Ash Wednesday storm of March 1962 was simulated with the profile response model. There was good agreement between the calculated erosion amounts of the shore-normal profiles for Bodie and Pea Islands (on either side of Oregon Inlet) and values measured in the field.

As an alternative to the stabilization of the entrance channel by construction of two jetties, a nonstructural solution proposed by the Department of the Interior was evaluated using the profile response model. The solution involved disposal of the dredged material from the entrance channel in the near-shore region with the idea that the material would be dispersed shoreward by wave action at a rate sufficient to prevent dredging-induced beach erosion. The results of the model indicated that on the average only 25 percent of the disposed material migrated toward the shore in a year. This migration was insufficient to prevent dredging-induced beach erosion.

In order to perform an ocean bar channel dredging analysis, the US Army Engineer District, Wilmington (SAW), needed to know the period of time that dredges of the CURRITUCK and ATCHAFALAYA/MERMENTAU classes could operate in the entrance channel under the influence of waves. To study this problem, the wave propagation model was run allowing for wave-current interactions. Using the model results, SAW determined the limiting wave heights for dredging operations to be deepwater significant heights of 3.0 and 4.0 ft, respectively, for the two classes of dredges.

The CIP system was used to study the erosion and accretion in the entrance channel as well as the lateral movement of the channel in the presence of the south jetty alone, simulating a construction sequence in which the south jetty was built before the north jetty. To accomplish this the longshore sediment transport model simulated an average year's wave climate and tide, using the results of the wave, wave-induced current, and tide models. The results of the simulation showed that during the year a total of 1,055,990 cu yd of material was trapped in the entrance channel, whereas a total of 660,000 cu yd of material was eroded between the southern boundary of the channel and the south jetty. It was determined that the entrance channel could move on the average about 150 ft per year toward the south jetty.

Unclassified

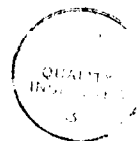
SECURITY CLASSIFICATION OF THIS PAGE(When Data Entered)

PREFACE

The study described herein was authorized by the US Army Engineer District, Wilmington. All elements of the investigation were conducted at the US Army Engineer Waterways Experiment Station (WES) from July 1980 to September 1984. Personnel working on the study were in the Wave Dynamics Division (WDD), Hydraulics Laboratory (HL), under the direction of Mr. Henry B. Simmons, Chief, HL, Dr. Robert W. Whalin, former Chief, WDD, and Mr. C. Eugene Chatham, Jr., acting Chief, WDD, during July 1980 to June 1983. Effective July 1, 1983, WDD and its personnel were combined with and transferred to the Coastal Engineering Research Center (CERC) of WES which was under the supervision of Dr. Whalin, former Chief, CERC. Currently CERC is under the direction of Mr. Charles C. Calhoun, Jr., Acting Chief. Dr. James R. Houston, Chief, Research Division, was Project Manager for the study from 1980 to 1983, and Dr. S. Rao Vemulakonda was Project Manager from 1983 to 1984.

The study was performed by Drs. Houston, S. Rao Vemulakonda, Abhimanyu Swain, Mrs. Lucia W. Chou, and Messrs. Paul D. Farrar and Bruce A. Ebersole. Numerical computations associated with this work were performed on the CRAY 1 computers of the Air Force Weapons Laboratory, Kirtland AFB, New Mexico, and Boeing Computer Services. This report was edited by Mrs. Shirley A. J. Hanshaw, Publications and Graphic Arts Division, WES.

COL Tilford C. Creel, CE, and COL Robert C. Lee, CE, were Commanders and Directors of WES during the preparation of this report. COL Allen F. Grum, USA, was Director of WES during the publication of this report. Mr. Fred R. Brown and Dr. Whalin were Technical Directors.



Accession For	
NTIS CRA&I	<input checked="checked" type="checkbox"/>
DTIC TAB	<input type="checkbox"/>
Unannounced	<input type="checkbox"/>
Justification	
By	
Distribution /	
Availability Codes	
Dist	Availability of Special
A-1	

CONTENTS

	<u>Page</u>
PREFACE	1
LIST OF TABLES	2
LIST OF FIGURES	2
CONVERSION FACTORS, NON-SI TO SI (METRIC) UNITS OF MEASUREMENT	5
PART I: INTRODUCTION	7
Background	7
Purpose	7
PART II: NUMERICAL MODELS	8
Introduction	8
Wave Propagation Model	11
Wave-Induced Current and Setup Model	20
Tidal and Storm Surge Models	43
Sediment Transport Models	45
Profile Response (Onshore-Offshore) Model	54
PART III: APPLICATIONS	68
Ash Wednesday Storm	68
Evaluation of Nonstructural Solution	68
Wave-Current Interaction	76
Single Jetty Evaluation	81
PART IV: SUMMARY AND CONCLUSIONS	89
REFERENCES	91
PLATES 1-13	
APPENDIX A: NOTATION	A1

LIST OF TABLES

<u>No.</u>		<u>Page</u>
1	Percentage of Dumped Material Transported into the Active Surf Zone in 1 Year	75
2	Selected Wave Characteristics from 20-Year Hindcast of WESWIS . .	83
3	Volume of Materials Trapped in the Oregon Inlet Channel	86
4	Volume of Materials Eroded between the South Jetty and the South Channel Boundary	86

LIST OF FIGURES

<u>No.</u>		<u>Page</u>
1	Location Map	6
2	Numerical grid for Oregon Inlet simulation	10

LIST OF FIGURES

No.		Page
3	Wave climate for Oregon Inlet: $\theta_o = 45$ deg	17
4	Wave climate for Oregon Inlet: $\theta_o = 0$ deg	18
5	Wave climate for Oregon Inlet: $\theta_o = -45$ deg	19
6	Definition sketch for the wave-induced current model	22
7	Cell notation	26
8	Setup and free gravity wave	34
9	Wave setup	34
10	Velocity in offshore direction	35
11	Longshore velocity	35
12	Wave setup, WES calculations	37
13	Velocity in offshore direction, WES calculations	37
14	Longshore velocity, WES calculations	38
15	Comparison of numerical solution for setup with experimental data	38
16	Comparison of numerical and analytical solutions for longshore current for plane beach	40
17	Effect of mixing parameter P on the numerical solution for longshore current for plane beach	40
18	Topography used for Oregon Inlet numerical model simulation	42
19	Mean water levels from Oregon Inlet numerical model simulation	42
20	Velocity vector plot for Oregon Inlet simulation	43
21	Numerical grids used for tidal and storm surge computations	44
22	Ebb currents for existing conditions	46
23	Ebb current for 2,500-ft jetty spacing	47
24	Schematization of beach profile at time t	56
25	Comparison of experimental and calculated onshore-offshore profiles, Test 1	61
26	Comparison of experimental and calculated onshore-offshore profiles, Test 2	62
27	Comparison of experimental and calculated onshore-offshore profiles, Test 3	63
28	Comparison of experimental and calculated onshore-offshore profiles, Test 4	64
29	Comparison of calculated and measured beach profiles for Leadbetter Beach, California, 1980	65
30	Comparison of calculated and measured shore-normal profiles for New River Inlet, North Carolina (dredged disposal sand movement)	66
31	Comparison of calculated and measured final profiles for New River Inlet, North Carolina	67
32	Comparison of calculated and measured shore-normal erosion for Bodie Island during 1962 Ash Wednesday storm	69
33	Comparison of calculated and measured shore-normal erosion for Pea Island during 1962 Ash Wednesday storm	69
34	Location of nearshore disposal area	71
35	Effect of ebb current magnitude on wave amplification (no jetties)	77
36	Dependence of wave amplification on wave period	77
37	Effect of jetty spacing on wave steepness ($H/L = 0.057$ for no jetties)	78

LIST OF FIGURES

<u>No.</u>		<u>Page</u>
38	Ebb currents for 3,500-ft jetty spacing	79
39	Ebb currents for 5,000-ft jetty spacing	80
40	Location of entrance channel	84
41	Flow cross sections at beginning and end of 1-year simulation	88

CONVERSION FACTORS, NON-SI TO SI (METRIC)
UNITS OF MEASUREMENT

Non-SI units of measurement used in this report can be converted to SI
(metric) units as follows:

<u>Multiply</u>	<u>By</u>	<u>To Obtain</u>
cubic feet per second per foot	0.0929	cubic metres per second per metre
cubic yards	0.7645	cubic metres
feet	0.3048	metres
miles (US statute)	1.609	kilometres
square miles	2.5899	square kilometres

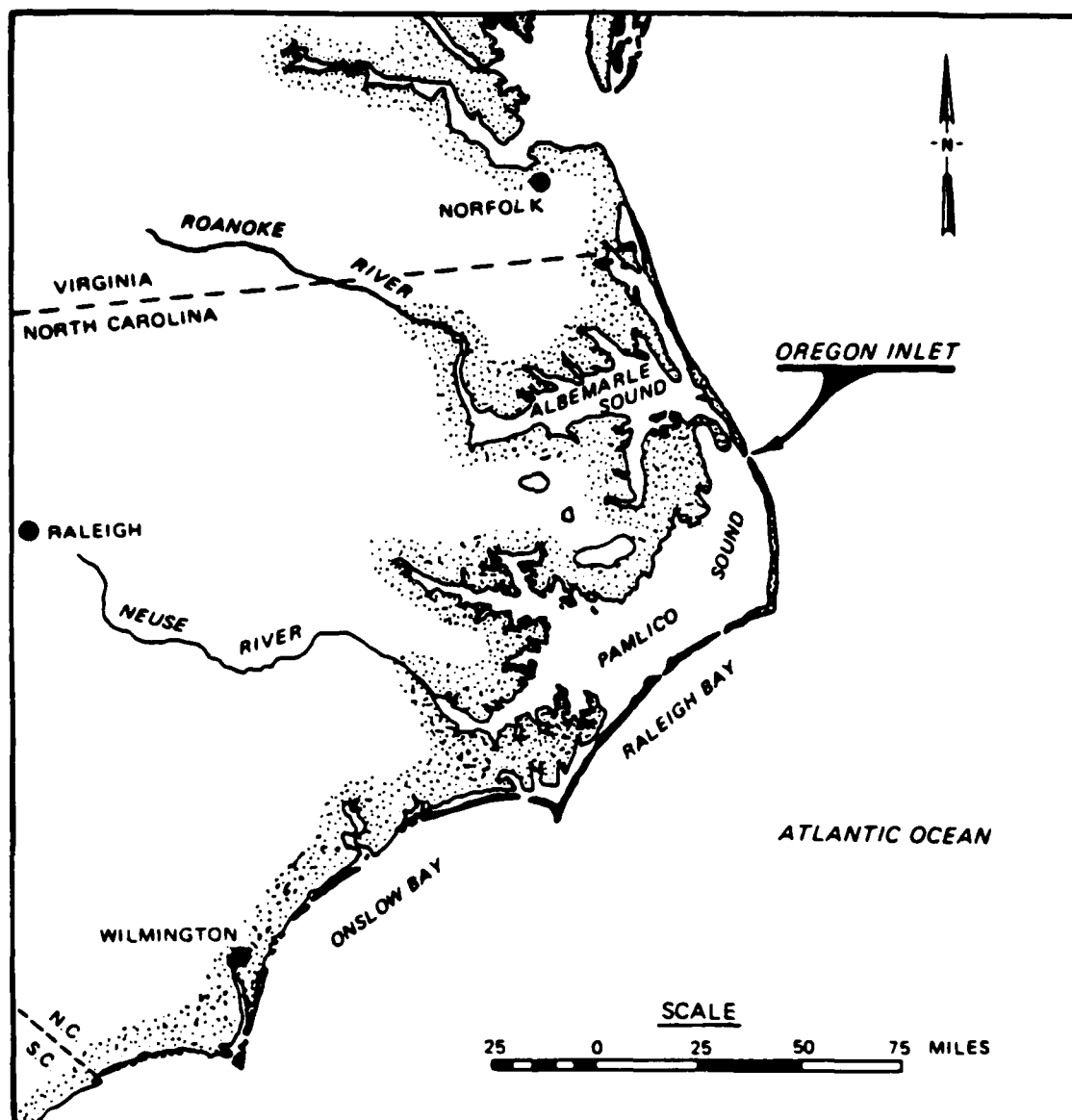


Figure 1. Location map

COASTAL AND INLET PROCESSES NUMERICAL MODELING SYSTEM FOR
OREGON INLET, NORTH CAROLINA

PART I: INTRODUCTION

Background

1. Oregon Inlet is a large inlet through the Outer Banks barrier island system of North Carolina. It is located about 85 miles* south of Cape Henry, Virginia, and about 40 miles north of Cape Hatteras in Dare County, North Carolina (Figure 1). The inlet is the only existing breach in the barrier island system of North Carolina between the Virginia-North Carolina state line and Cape Hatteras. The shorelines immediately north of Oregon Inlet comprise a portion of the Cape Hatteras National Seashore Recreation Areas, and the shorelines immediately south are administered by the US Fish and Wildlife Service as the Pea Island Wildlife Refuge.

2. The Manteo (Shallowbag) Bay, North Carolina, project was authorized by Congress in 1970 and included provisions for the stabilization of Oregon Inlet with dual jetties and the deepening of the ocean bar channel to 20 ft. In addition, there were provisions for bypassing across the inlet sand intercepted by the jetties.

Purpose

3. The purpose of this study was to develop a set of numerical models called Coastal and Inlet Processes (CIP) Numerical Modeling System to simulate coastal and inlet processes in the vicinity of Oregon Inlet, North Carolina. The models would be required to handle wave, current, and sediment transport processes of importance in the area and be computationally efficient enough to allow simulations of practical engineering utility.

* A table of factors for converting non-SI to SI (metric) units is presented on page 5.

PART II: NUMERICAL MODELS

Introduction

4. Although in recent years there has been considerable interest in the use of numerical models to simulate coastal processes, models have not been developed that can handle all of the complexities of an actual inlet system. In addition, existing numerical models that consider parts of the overall problem can consider only small idealized problems and not actual spatially large and complex problems.

5. In order to simulate coastal processes, models must be able to consider the propagation of waves over a complex bathymetry, the generation of wave-induced currents (littoral and rip currents), the circulation of tidal and storm surge currents, the littoral transport of sediment, and the response of profiles to wave action by the onshore-offshore transport of sediment. The models must be able to simulate processes over a relatively large area and resolve strong gradients in certain areas (e.g. within surf zone areas).

6. The models described in this report use the finite difference method for computations. In order to cover a large region but still maintain high resolution in desired areas, the models use a smoothly varying grid that allows cells to be small in certain areas (e.g., surf zone or inlet) and large in others (e.g., ocean or sound). A piecewise reversible transformation (analogous to that used by Wanstrath 1977) is used independently in the x and y directions to map the variable grid into a uniform grid used in the computational space. The transformation has the following form:

$$x = a_p + b_p \alpha_1^c \quad (1)$$

$$y = a_q + b_q \alpha_2^c \quad (2)$$

where a_p , b_p , c_p , a_q , b_q , and c_q^* are arbitrary constants for regions p

* For convenience, symbols and abbreviations are listed in the Notation (Appendix A).

and q in the x and y directions, respectively, and α_1 and α_2 are coordinates in the computational space. This transformation allows all derivatives to be centered in the computational space. Many stability problems commonly occurring in variable grid schemes are eliminated when using this transformation since the real space grid is smoothly varying with the coordinate and its first derivative being continuous at the boundaries between regions.

7. The partial differential equations are solved by finite difference integration on a grid of spatial points. A right-handed coordinate system is used with the x -coordinate increasing in the offshore direction and the y -coordinate increasing along the shoreline with the ocean to the right. The partial derivative of an arbitrary variable s in domain p is

$$\frac{\partial s}{\partial x} = \frac{1}{\mu_x} \frac{\partial s}{\partial \alpha_1} \quad (3)$$

where

$$\mu_x = \frac{\partial x}{\partial \alpha_1} = b_p c_p \alpha_1^{c_p - 1} \quad (4)$$

Similarly

$$\frac{\partial s}{\partial y} = \frac{1}{\mu_y} \frac{\partial s}{\partial \alpha_2} \quad (5)$$

where

$$\mu_y = \frac{\partial y}{\partial \alpha_2} = b_q c_q \alpha_2^{c_q - 1} \quad (6)$$

If the grid in the x -, y -coordinate system is to have even grid spacing, all values of μ_x and μ_y will be constant (1 if $\Delta\alpha_1 = \Delta x$ and $\Delta\alpha_2 = \Delta y$). The constants a_p , b_p , c_p , a_q , b_q , and c_q for all the domains and the values of μ_x and μ_y at grid cell faces and centers are determined using an interactive computer program called MAPIT.

8. Figure 2 shows the variable finite difference numerical grid used by all of the numerical models presented in this report to calculate coastal and inlet processes at Oregon Inlet. The grid has 4,158 cells and covers an area of approximately 60 square miles with grid cells having side lengths as small as 100 ft. If a uniform grid were used with 100-ft grid cells, approximately 170,000 grid cells would be required. Since the computational time requirements of the numerical models presented in this report generally increase with

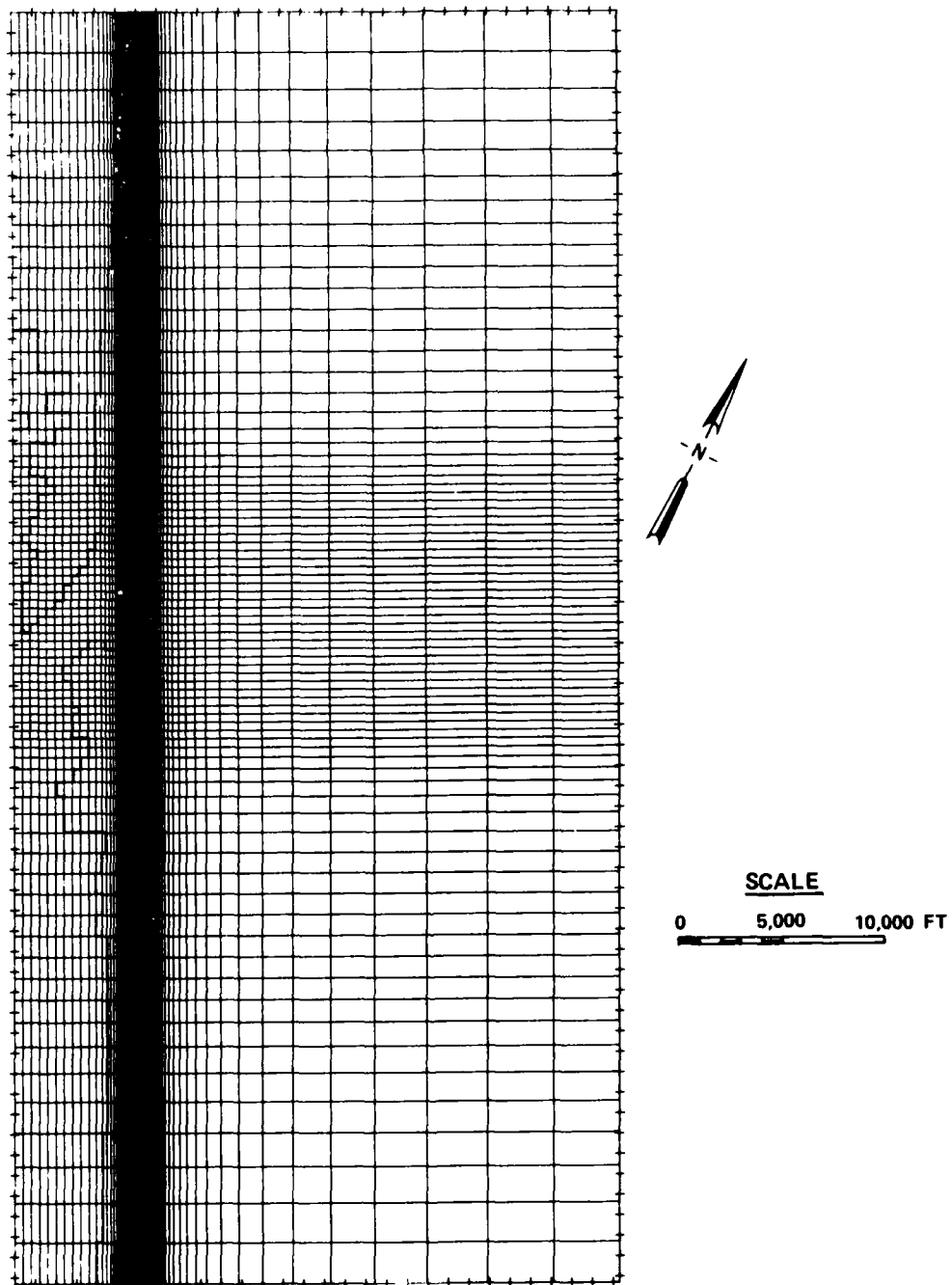


Figure 2. Numerical grid for Oregon Inlet simulation

the number of grid cells to approximately the 1.5 power, a regular grid with 100-ft cells would require almost 250 times as much computational time as the variable grid shown in Figure 2.

9. The grid shown in Figure 2 covers a portion of Pamlico Sound, approximately 12 miles of ocean coastlines on Bodie and Pea Islands north and south of Oregon Inlet, and a section of the Atlantic Ocean extending out to the 60-ft mean low water (MLW) contour. The ocean boundary of the grid is far enough from the inlet to be in a region where the contours are straight and parallel. Thus all the effects of bathymetric complexities on waves and currents are included in the grid computations.

Wave Propagation Model

10. The wave climate at Oregon Inlet is available through the Waterways Experiment Station Wave Information Study (WESWIS). Twenty-year hindcast data were obtained at a water depth of 60 ft off the coast of Oregon Inlet. The development of a wave propagation numerical model was necessary to propagate waves over the complex bathymetry around the inlet and to determine wave-current interactions in the vicinity of the inlet.

11. The traditional method of propagating waves over the nearshore region is wave ray tracing, in which the paths of individual wave rays are propagated from deeper water to shore. One disadvantage of ray tracing is the difficulty of converting a large number of wave rays into arrays of wave heights, wave numbers, and directions of propagation for specific grid points. Such arrays are needed by the numerical models that calculate wave-induced currents and sediment transport. It is difficult to convert a wave ray field into arrays providing information at specific grid points because it is not possible to know a priori where individual rays will propagate and thus where rays must be started in order to go through given points. Another disadvantage of wave ray tracing is that wave-current interaction calculations cannot be made, since ray theory assumes that energy cannot cross wave orthogonals. This eliminates the possibility of currents sweeping wave energy across orthogonals.

12. In order to eliminate the problems of wave ray tracing, a numerical model was developed to calculate wave propagation on a gridded system. The model considers the same system of differential equations considered by Noda

et al. (1974) and Ebersole and Dalrymple (1980). However, to improve stability, some of the solution techniques employed to solve these differential equations were different from those used by previous investigators. The models used by Noda et al. (1974) and Ebersole and Dalrymple (1980) typically had stability problems when the angle of incidence of the waves was large or the bathymetry was complex. The model described in this report was developed also to perform calculations on a uniformly variable grid. This allowed the wave calculations to be performed on the same grid as wave-induced current and sediment transport calculations.

13. In order to determine the angle of wave propagation θ , use is made of the irrotationality of the wave number vector \vec{k} :

$$\vec{V} \times \vec{k} = 0 \quad (7)$$

When vertical propagation is ignored

$$\frac{\partial k_x}{\partial y} - \frac{\partial k_y}{\partial x} = 0 \quad (8)$$

where

$$k_x = k \cos \theta \quad (9)$$

$$k_y = k \sin \theta \quad (10)$$

$$k = \left| \vec{k} \right| \quad (11)$$

and θ is the angle of wave propagation. Equation 8 becomes

$$\cos \theta \frac{\partial \theta}{\partial x} + \sin \theta \frac{\partial \theta}{\partial y} - \cos \theta \frac{1}{k} \frac{\partial k}{\partial y} + \sin \theta \frac{1}{k} \frac{\partial k}{\partial x} = 0 \quad (12)$$

14. In order to conserve wave frequency when a current is present

$$\omega_o = \omega + \vec{k} \cdot \vec{V} \quad (13)$$

where ω_o is a constant equal to $2\pi/T_o$, T_o is the period of wave when there is no current, ω is the radian frequency as it appears to a stationary observer, and \vec{V} is the current velocity vector. Substituting for ω , using

Equations 9 and 10, and defining $\vec{V} = U\hat{i} + V\hat{j}$ yields

$$\omega_o = \left[gk \tanh(kd) \right]^{1/2} + Uk \cos \theta + Vk \sin \theta \quad (14)$$

where g is the acceleration due to gravity, and d is the local water depth.

15. Taking the differential of Equation 14 yields

$$\frac{1}{k} \frac{\partial k}{\partial x} = \frac{\partial \theta}{\partial x} \frac{(U \sin \theta - V \cos \theta)}{A} - \left[\frac{\frac{\partial U}{\partial x} \cos \theta + \frac{\partial V}{\partial x} \sin \theta}{A} \right] - \left[\frac{(\omega_o - Uk \cos \theta - Vk \sin \theta)}{A \sinh(2kd)} \frac{\partial d}{\partial x} \right] \quad (15)$$

where

$$A = \frac{1}{2} \left[1 + \frac{2kd}{\sinh(2kd)} \right] \left(\frac{\omega_o}{k} - U \cos \theta - V \sin \theta \right) + U \cos \theta + V \sin \theta$$

Likewise

$$\frac{1}{k} \frac{\partial k}{\partial y} = \left[\frac{\partial \theta}{\partial y} \frac{(U \sin \theta - V \cos \theta)}{A} \right] - \left(\frac{\frac{\partial U}{\partial y} \cos \theta + \frac{\partial V}{\partial y} \sin \theta}{A} \right) - \left[\frac{(\omega_o - Uk \cos \theta - Vk \sin \theta)}{A \sinh(2kd)} \frac{\partial d}{\partial y} \right] \quad (16)$$

16. By substitution of Equations 15 and 16 into Equation 12

$$\begin{aligned} & \frac{\partial \theta}{\partial x} \left[\cos \theta + \frac{\sin \theta (U \sin \theta - V \cos \theta)}{A} \right] + \frac{\partial \theta}{\partial y} \\ & \times \left[\sin \theta - \frac{\cos \theta (U \sin \theta - V \cos \theta)}{A} \right] \\ & + \cos \theta \left[\frac{\frac{\partial U}{\partial y} \cos \theta + \frac{\partial V}{\partial y} \sin \theta}{A} + \frac{\omega_o - Uk \cos \theta - Vk \sin \theta}{A \sinh(2kd)} \frac{\partial d}{\partial y} \right] \\ & - \sin \theta \left[\frac{\frac{\partial U}{\partial x} \cos \theta + \frac{\partial V}{\partial x} \sin \theta}{A} + \frac{\omega_o - Uk \cos \theta - Vk \sin \theta}{A \sinh(2kd)} \frac{\partial d}{\partial x} \right] = 0 \end{aligned} \quad (17)$$

Height equation

17. The conservation of energy is given by

$$\frac{\partial E}{\partial t} + \frac{\partial}{\partial x_i} \left\{ E \left[V_i + (C_g)_i \right] \right\} + S_{i,j} \frac{\partial V_j}{\partial x_i} = 0, \quad i = 1, 2 \quad (18)$$

where

E = wave energy density and is equal to $\rho g H^2 / 8$

ρ = density of water

H = wave height

$S_{i,j}$ = "radiation stress"

as defined by Longuet-Higgins and Stewart (1964). Writing Equation 18 in terms of H and assuming a steady-state wave field ($\partial E / \partial t = 0$) gives

$$\begin{aligned} \frac{\partial H}{\partial x} (U + C_g \cos \theta) + \frac{\partial H}{\partial y} (V + C_g \sin \theta) + \frac{H}{2} \frac{\partial}{\partial x} (U + C_g \cos \theta) \\ + \frac{H}{2} \frac{\partial}{\partial y} (V + C_g \sin \theta) + \frac{H}{2} \left(\bar{\sigma}_{xx} \frac{\partial U}{\partial x} + \bar{\sigma}_{yx} \frac{\partial U}{\partial y} + \bar{\sigma}_{xy} \frac{\partial V}{\partial x} + \bar{\sigma}_{yy} \frac{\partial V}{\partial y} \right) = 0 \end{aligned} \quad (19)$$

The dimensionless radiation stresses are given by

$$\bar{\sigma}_{xx} = \frac{S_{xx}}{E} = \left(2n - \frac{1}{2} \right) \cos^2 \theta + \left(n - \frac{1}{2} \right) \sin^2 \theta \quad (20)$$

$$\bar{\sigma}_{yy} = \frac{S_{yy}}{E} = \left(2n - \frac{1}{2} \right) \sin^2 \theta + \left(n - \frac{1}{2} \right) \cos^2 \theta \quad (21)$$

$$\bar{\sigma}_{xy} = \bar{\sigma}_{yx} = \frac{S_{xy}}{E} = \frac{S_{yx}}{E} = \frac{n}{2} \sin 2\theta \quad (22)$$

where

$$n = \frac{C_g}{C} = \frac{1}{2} \left[1 + \frac{2kd}{\sinh(2kd)} \right] \quad (23)$$

Finite difference equations

18. Equations 3 and 5 are substituted into Equation 17, and all terms are written in centered finite difference form.

$$\begin{aligned}
& \frac{\theta_{i+1,j} - \theta_{i-1,j}}{2\mu_{x;i,j} \Delta\alpha_1} \left[\cos \theta + \frac{\sin \theta (U \sin \theta - V \cos \theta)}{A} \right]_{i,j} + \frac{\theta_{i,j+1} - \theta_{i,j-1}}{2\mu_{y;i,j} \Delta\alpha_2} \\
& \times \left[\sin \theta - \frac{\cos \theta (U \sin \theta - V \cos \theta)}{A} \right]_{i,j} + \cos \theta_{i,j} \\
& \times \left[\frac{\left(\frac{\partial U}{\partial y} \cos \theta + \frac{\partial V}{\partial y} \sin \theta \right)}{A} + \frac{\left(\omega_o - Uk \cos \theta - Vk \sin \theta \right)}{A \sinh(2kd)} \frac{\partial d}{\partial y} \right]_{i,j} - \sin \theta_{i,j} \\
& \times \left[\frac{\left(\frac{\partial U}{\partial x} \cos \theta + \frac{\partial V}{\partial x} \sin \theta \right)}{A} + \frac{\left(\omega_o - Uk \cos \theta - Vk \sin \theta \right)}{A \sinh(2kd)} \frac{\partial d}{\partial x} \right]_{i,j} = 0
\end{aligned} \tag{24}$$

where $\Delta\alpha_1$ and $\Delta\alpha_2$ are the constant grid spacings in α_1 , α_2 space. All values of d , U , and V are known at the start of computation for θ . If all values of θ on rows i and $i+1$ are known, then Equation 24 can be solved for all values on row $i-1$. When this has been done, the next row can be solved. To find $\theta_{i-1,j}$ it is first necessary to find $k_{i,j}$. Since $\theta_{i,j}$ is already known, Equation 12 can be solved by Newton-Raphson iteration for $k_{i,j}$.

19. Substitution of Equations 3 and 5 into Equation 19 yields

$$\begin{aligned}
& \frac{H_{i+1,j} - H_{i-1,j}}{2\mu_{x;i,j} \Delta\alpha_1} \left(U + C_g \cos \theta \right)_{i,j} + \frac{H_{i,j+1} - H_{i,j-1}}{2\mu_{y;i,j} \Delta\alpha_2} \left(V + C_g \sin \theta \right)_{i,j} \\
& + \left[\frac{H}{2} \frac{\partial}{\partial x} (U + C_g \cos \theta) + \frac{H}{2} \frac{\partial}{\partial y} (V + C_g \sin \theta) \right. \\
& \left. + \frac{H}{2} \left(\bar{\sigma}_{xx} \frac{\partial U}{\partial x} + \bar{\sigma}_{yx} \frac{\partial U}{\partial y} + \bar{\sigma}_{xy} \frac{\partial V}{\partial x} + \bar{\sigma}_{yy} \frac{\partial V}{\partial y} \right) \right]_{i,j} = 0
\end{aligned} \tag{25}$$

At this point in the computation, all values of U , V , d and θ are known, making possible the calculation of all values of k , n , $\bar{\sigma}$, and C_g as well. If all of the values of H in rows i and $i+1$ are known, then all values of H in row $i-1$ can be found, which then allows the determination of values of H in the next row. The values of H in the two

outermost rows of the model grid are specified initially from wave input data, allowing computation of values on all other rows.

Model use

20. Wave climate data were provided at the boundary of the computational grid (Figure 2) by WESWIS. With the wave height, period, and direction of propagation prescribed at the ocean boundary, the wave propagation model determines wave heights, directions of propagation, and wave numbers at all 4,158 grid points in the computational grid. If the wave height at any grid cell is greater than 0.78 of the local water depth, the model assumes that the wave is breaking and, based upon nonsaturated wave-breaking theory, sets the breaking wave height equal to 0.78 of the water depth.

21. Figures 3, 4, and 5 demonstrate the application of the wave model to Oregon Inlet (existing conditions). Each of these figures corresponds to a particular wave condition in deep water and shows the region near the inlet channel and shoals. The wave height and the period in deep water are the same for the three cases and are equal to 2.175 ft and 6.0 sec, respectively. The wave direction in deep water is given by $\theta_o = 45, 0, \text{ and } -45 \text{ deg}$, respectively, for the three cases where θ_o is the angle the wave propagation direction makes with the normal to the shoreline. A uniform grid with $\Delta x = \Delta y = 240 \text{ ft}$ was used for these runs. In each figure, the depth contours are represented by dashed lines, the wave height contours by solid lines, and the wave directions by vectors. Figure 3 represents waves propagating approximately in the direction of the channel. The waves are refracted onto the shoals, on either side of the channel, where they eventually break. As a result, very little wave energy is propagated up the channel. Figure 4 shows the inlet response for waves incident normal to the shoreline. Again the waves refract onto both shoals and break. There is a decrease in wave height just outside the shoals. Figure 5 illustrates a condition where the waves are obliquely incident, in a direction approximately normal to the channel. Waves converge on the near shoal, but note how they refract around the far shoal and eventually converge with reformed waves propagating across the channel. The computational requirements for the wave model were very modest. For the 4,158-cell variable grid, the cost per run was under \$4.00.

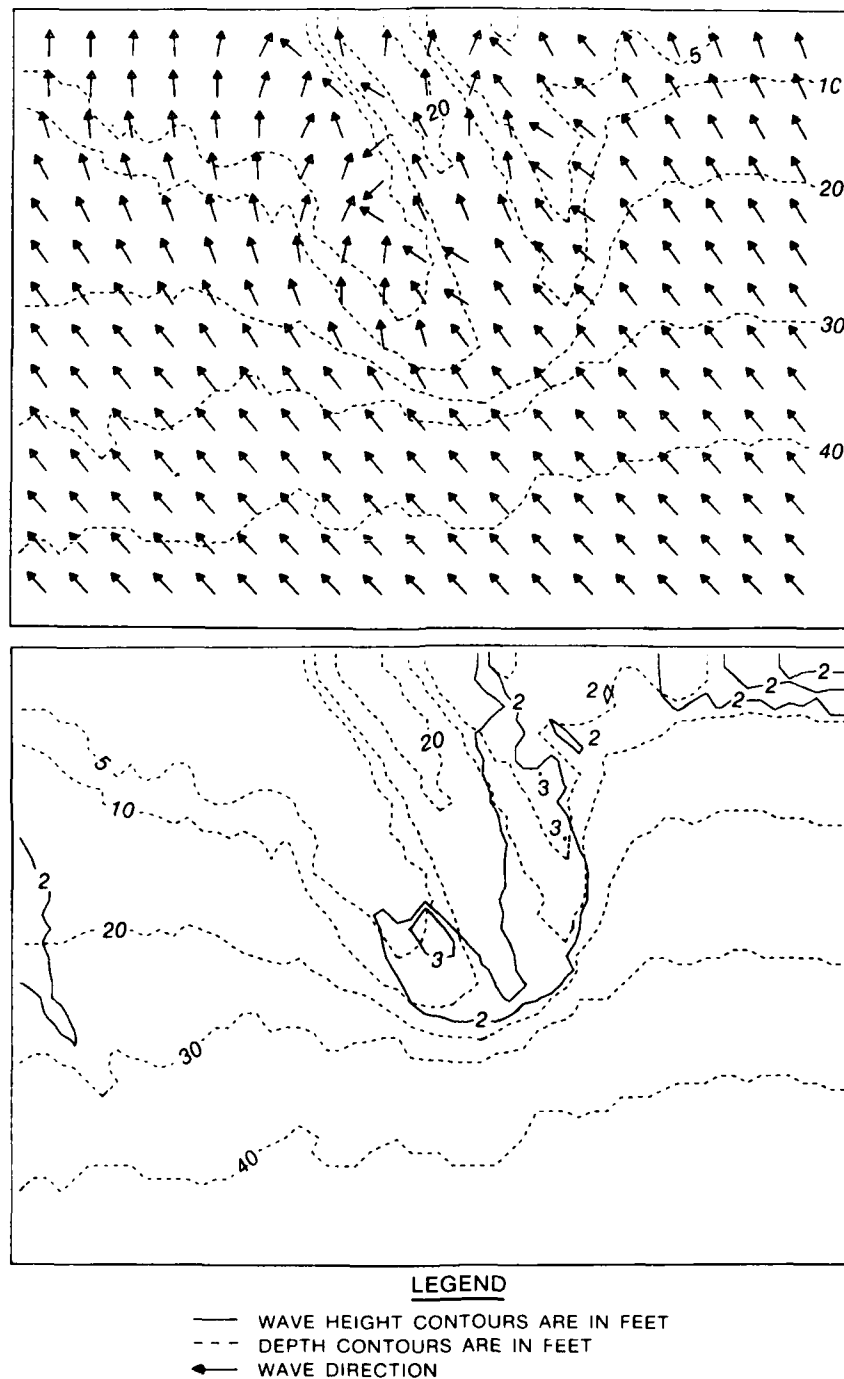


Figure 3. Wave climate for Oregon Inlet: $\theta_0 = 45$ deg

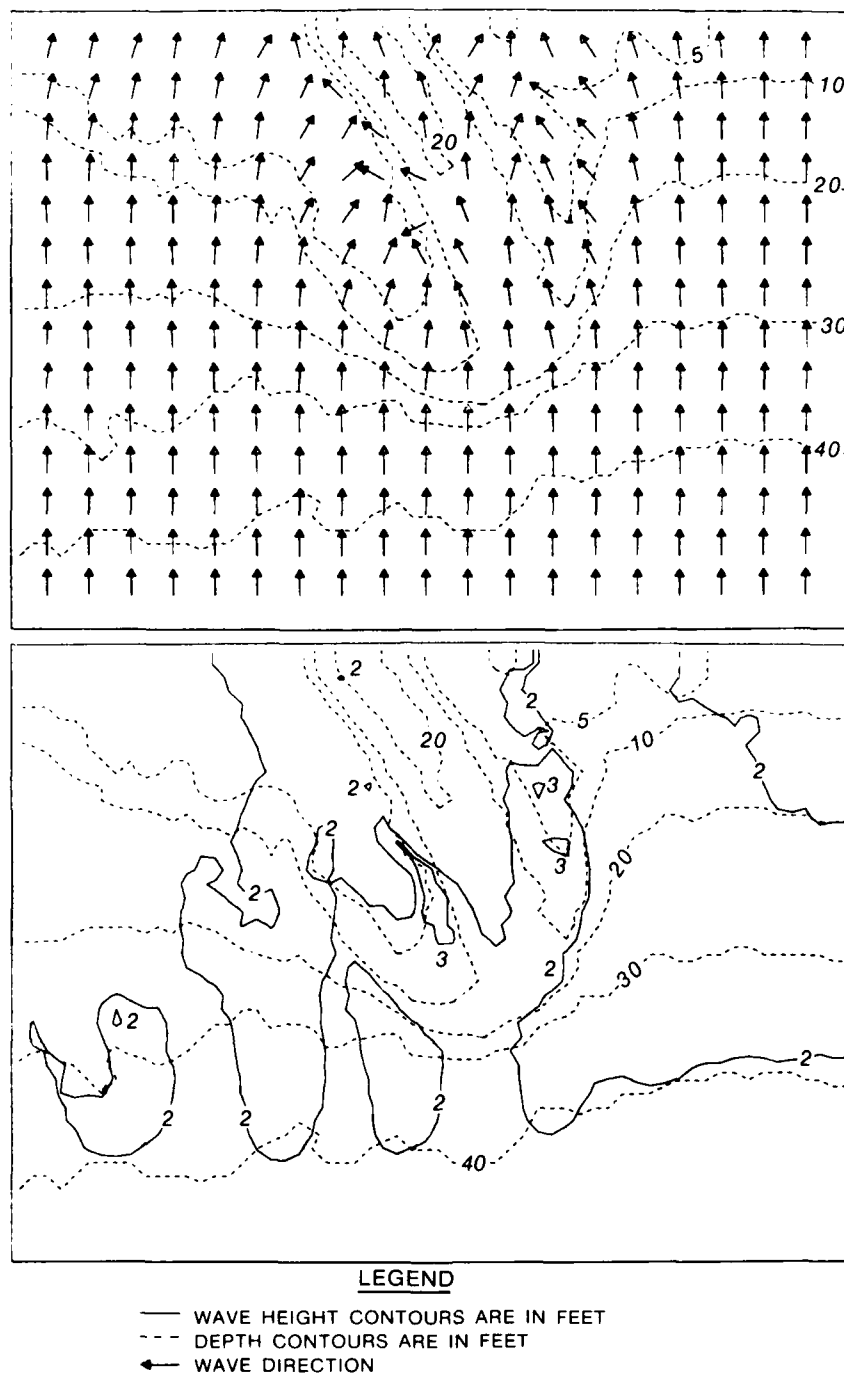


Figure 4. Wave climate for Oregon Inlet: $\theta_0 = 0$ deg

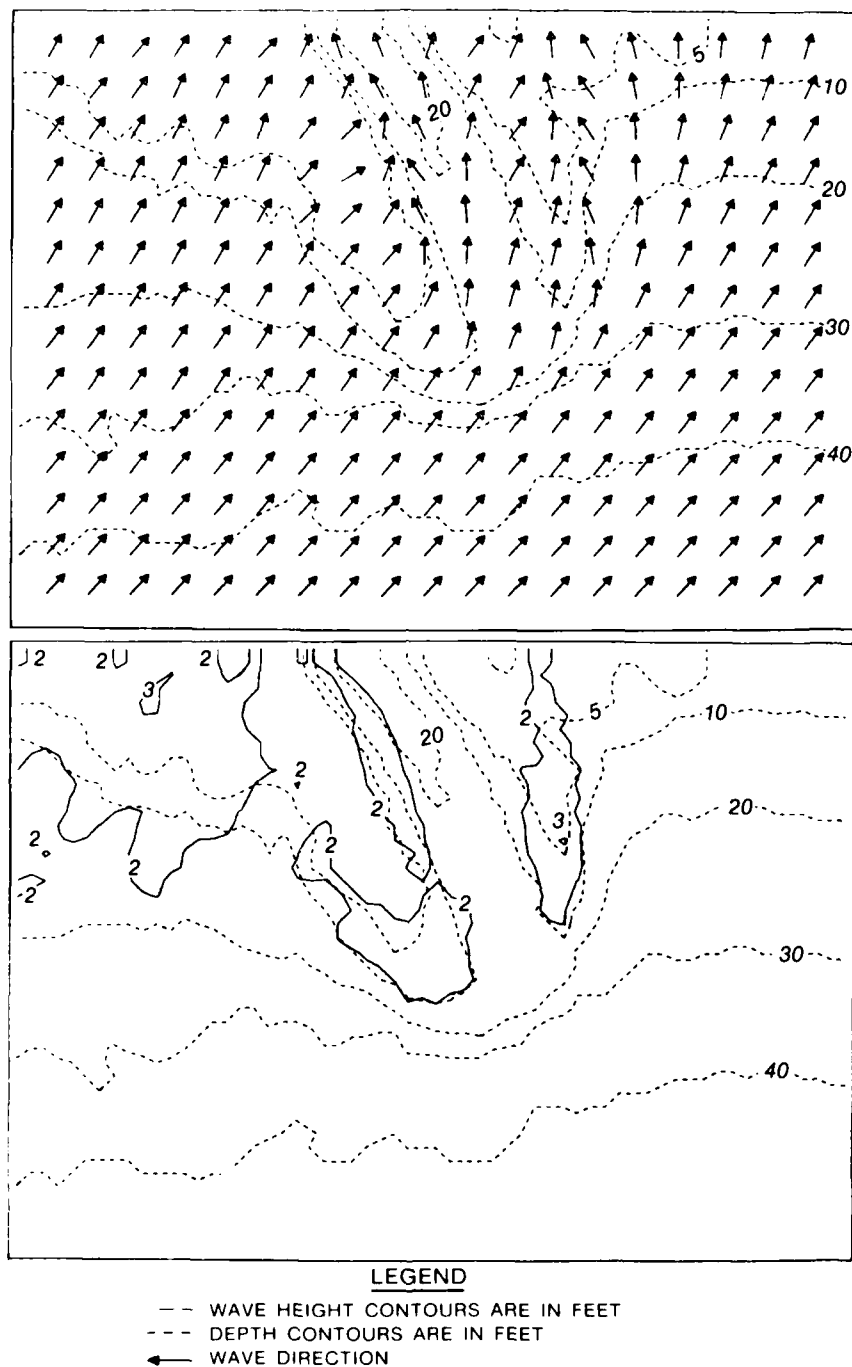


Figure 5. Wave climate for Oregon Inlet: $\theta_o = -45$ deg

Wave-Induced Current and Setup Model

22. When waves break, they generate currents (e.g., littoral and rip currents) and changes in the mean water level (setup and setdown). Since these currents are the main transport mechanism for sediment on a coastline, they must be simulated in detail in order to model coastal processes. The theory of the generation of wave-induced currents was developed by Bowen (1969), Thornton (1970), and Longuet-Higgins (1970). Numerical models have been developed to determine wave-induced currents (Noda 1974, Birkemeier and Dalrymple 1975, Liu and Lennon 1978). These models typically either consider only simple and idealized situations, such as plane beaches and periodic bathymetries, or neglect terms of the governing equations involving unsteadiness, advection, and/or lateral mixing.

23. In recent years, Ebersole and Dalrymple (1980) developed a wave-induced current model that solves equations that include terms for unsteady flow, advection, and lateral mixing. The model was applied to fairly small problems with relatively simple bathymetries. It used a simple explicit finite difference computational scheme and grid cells of uniform size. Stability was obtained by Ebersole and Dalrymple by using a time-step such that the Courant number was less than 1.0.

24. Since the Oregon Inlet region that required modeling was relatively large, it was important to develop a model that had a variable grid and was extremely efficient computationally. One solution technique that is extremely efficient is the alternating direction implicit (ADI) finite-difference method. ADI schemes are not limited (as are explicit schemes) to a Courant number less than 1 to maintain stability. Courant numbers of 5 to 10 or higher are typically used. In view of the similarity between the equations that govern wave-induced currents and currents produced by long waves (e.g., tides), a wave-induced current model was developed in this study by modifying an existing, well tested Waterways Experiment Station (WES) long-wave numerical model known as WIFM (WES Implicit Flooding Model) (Butler 1980). WIFM is a finite-difference numerical model that employs an ADI computational scheme and in addition uses grid cells of variable sizes.

25. WIFM was modified to calculate wave-induced currents and setup by adding radiation stress terms that are the driving mechanism for wave-induced currents. In addition, the friction and mixing terms used in WIFM were

modified to conform to the formulations normally used in wave-induced current models. A velocity, as opposed to discharge, version of WIFM that included nonlinear advective terms was used.

Equations of motion

26. The hydrodynamic equations used in the model for wave-induced currents and setup may be derived from the Navier-Stokes equations (Phillips 1969). It is assumed in the derivation that the fluid is homogeneous and incompressible, and the vertical accelerations are negligible so that the pressure distribution is hydrostatic. By integrating the three-dimensional form of the equations in the vertical direction and applying appropriate boundary conditions, the depth-averaged two-dimensional form of the equations of motion and continuity are obtained. These equations are derived by time-averaging over the wave period. The momentum equations (Figure 6) are

$$\frac{\partial U}{\partial t} + U \frac{\partial U}{\partial x} + V \frac{\partial U}{\partial y} + g \frac{\partial \bar{\eta}}{\partial x} + \frac{1}{\rho d} \tau_{bx} + \frac{1}{\rho d} \left(\frac{\partial S_{xx}}{\partial x} + \frac{\partial S_{xy}}{\partial y} \right) - \frac{1}{\rho} \frac{\partial \tau_{xy}}{\partial y} = 0 \quad (26)$$

$$\frac{\partial V}{\partial t} + U \frac{\partial V}{\partial x} + V \frac{\partial V}{\partial y} + g \frac{\partial \bar{\eta}}{\partial y} + \frac{1}{\rho d} \tau_{by} + \frac{1}{\rho d} \left(\frac{\partial S_{xy}}{\partial x} + \frac{\partial S_{yy}}{\partial y} \right) - \frac{1}{\rho} \frac{\partial \tau_{xy}}{\partial x} = 0 \quad (27)$$

The continuity equation is

$$\frac{\partial \bar{\eta}}{\partial t} + \frac{\partial}{\partial x} (Ud) + \frac{\partial}{\partial y} (Vd) = 0 \quad (28)$$

Here U and V are the depth-averaged horizontal velocity components at time t in the x and y directions, respectively; $\bar{\eta}$ is the mean free surface displacement; ρ is the mass density of sea water; $d = \bar{\eta} + h$ is the total water depth where h is the local still-water depth; τ_{bx} and τ_{by} are the bottom friction stresses in the x and y directions, respectively; S_{xx} , S_{xy} , and S_{yy} are the radiation stresses which arise because of the excess momentum flux due to waves; and τ_{xy} is the lateral shear stress due to turbulent mixing. Note that when the still-water level is zero, the condition $\bar{\eta} > 0$ is called "setup" and $\bar{\eta} < 0$ is called "setdown."

27. The numerical model uses a linear formulation for friction (Longuet-Higgins 1970). Thus,

$$\tau_{bx} = \rho c \left| u_{orb} \right| > U \quad (29)$$

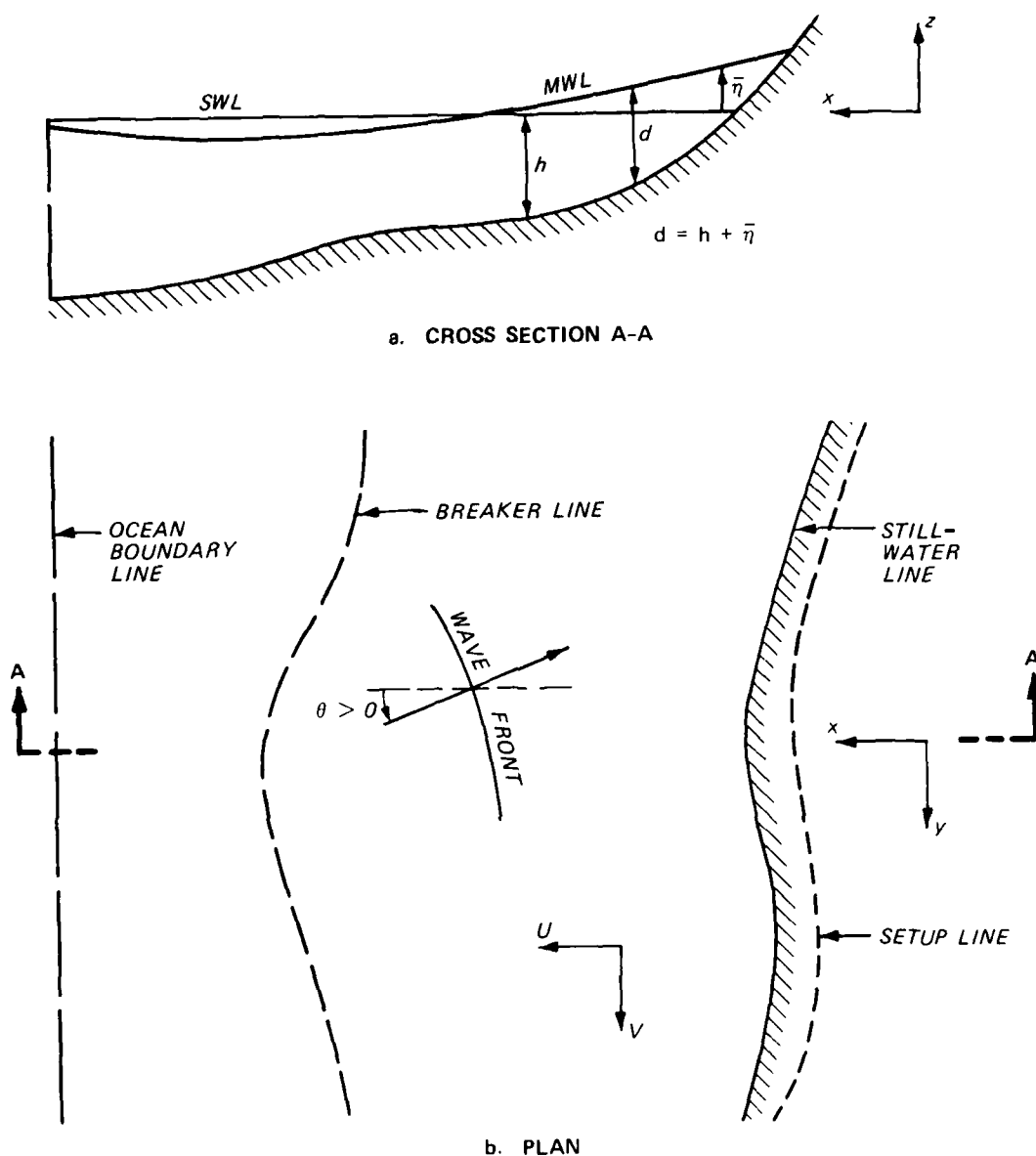


Figure 6. Definition sketch for the wave-induced current model

$$\tau_{by} = \rho c \langle |u_{orb}| \rangle V \quad (30)$$

where c is a drag coefficient (of the order of 0.01) and $\langle |u_{orb}| \rangle$ is the time average, over one wave period, of the absolute value of the wave orbital velocity at the bottom. Equations 29 and 30 are based on the assumption that the velocity components U and V of the current are small compared with the wave orbital velocity. From linear wave theory,

$$\langle |u_{orb}| \rangle = \frac{2H}{T \sinh kh} \quad (31)$$

where H is the local wave height, T is the wave period, and k is the local wave number. The numerical model can be adapted easily in the future to other formulations for friction such as nonlinear friction.

28. As mentioned previously, the radiation stresses are of major importance since they furnish the "driving" forces for wave-induced currents and setup. For monochromatic waves, they are defined by Equations 20, 21, and 22 in terms of the local wave climate variables H , k , and θ which are obtained from the wave propagation model described previously.

29. In the numerical model, the coordinate scheme is chosen such that x is positive in the offshore direction and y is approximately in the alongshore direction (Figure 6). An eddy viscosity formulation is chosen for the lateral shear. The eddy viscosity is assumed to be anisotropic. Denoting ϵ_x and ϵ_y as the eddy viscosities in x and y directions, respectively, in general, ϵ_y is assumed to be a constant and ϵ_x a function of x and y . Accordingly,

$$\tau_{xy} = \rho \left(\epsilon_y \frac{\partial U}{\partial y} + \epsilon_x \frac{\partial V}{\partial x} \right) \quad (32)$$

For field applications, the eddy viscosity ϵ_x is chosen according to the following relation given by Jonsson et al. (1974):

$$\epsilon_x = \frac{H^2 g T}{4 \pi^2 h} \cos^2 \theta \quad (33)$$

This represents twice the value used by Thornton (1970). It was believed that for field situations Equation 33 represented the eddy viscosities more realistically than the relation suggested by Longuet-Higgins (1970) for plane beaches. The value of ϵ_y was in general taken to be equal to the value of ϵ_x at the deepest part (usually near the offshore boundary) of the numerical grid. The numerical model is flexible enough to permit other formulations for eddy viscosity in the future, as our understanding improves.

30. Using the variable grid formulation discussed previously, the momentum equations become:

$$\begin{aligned}
& U_t + \frac{1}{\mu_x} UU_{\alpha_1} + \frac{1}{\mu_y} VU_{\alpha_2} + \frac{g}{\mu_x} \bar{\eta}_{\alpha_1} + \frac{1}{\rho d} \tau_{bx} + \frac{1}{\rho d} \left[\frac{1}{\mu_x} (S_{xx})_{\alpha_1} + \frac{1}{\mu_y} (S_{xy})_{\alpha_2} \right] \\
& - \epsilon_x \frac{1}{\mu_y} \frac{1}{\mu_x} V_{\alpha_2 \alpha_1} - \epsilon_y \frac{1}{\mu_y} \left[\frac{1}{\mu_y} U_{\alpha_2 \alpha_2} + \left(\frac{1}{\mu_y} \right)_{\alpha_2} U_{\alpha_2} \right] - \frac{1}{\mu_x \mu_y} (\epsilon_x)_{\alpha_2} V_{\alpha_1} = 0 \quad (34)
\end{aligned}$$

$$\begin{aligned}
& V_t + \frac{1}{\mu_x} UV_{\alpha_1} + \frac{1}{\mu_y} VV_{\alpha_2} + \frac{g}{\mu_y} \bar{\eta}_{\alpha_2} + \frac{1}{\rho d} \tau_{by} + \frac{1}{\rho d} \\
& \times \left[\frac{1}{\mu_x} (S_{xy})_{\alpha_1} + \frac{1}{\mu_y} (S_{yy})_{\alpha_2} \right] - \epsilon_x \frac{1}{\mu_x} \left[\frac{1}{\mu_x} V_{\alpha_1 \alpha_1} + \left(\frac{1}{\mu_x} \right)_{\alpha_1} V_{\alpha_1} \right] \\
& - \epsilon_y \frac{1}{\mu_x} \frac{1}{\mu_y} U_{\alpha_1 \alpha_2} - \frac{1}{\mu_x^2} (\epsilon_x)_{\alpha_1} V_{\alpha_1} = 0 \quad (35)
\end{aligned}$$

The continuity equation becomes:

$$\bar{\eta}_t + \frac{1}{\mu_x} (Ud)_{\alpha_1} + \frac{1}{\mu_y} (Vd)_{\alpha_2} = 0 \quad (36)$$

where the subscripts t , α_1 , and α_2 indicate partial derivatives with respect to time, α_1 , and α_2 , respectively, and the grid expansion coefficients μ_x and μ_y are defined by Equations 4 and 6. Note that in obtaining Equations 34, 35, and 36, the assumptions made in paragraph 29 were used.

31. The nonlinear advective terms in the equations of motion often pose stability problems. These terms are handled in the present model by using a special scheme which will be described in the next paragraph. The eddy viscosity terms can cause difficulties also during the numerical computation. The finite difference schemes selected in the model and the formulation for eddy viscosity adopted in the model minimize such difficulties and stability problems provided that time and space steps and eddy viscosity coefficients are properly selected for the phenomena being simulated.

Computational techniques

32. In order to solve the problem under consideration on a digital computer, the differential equations (Equations 34-36) have to be expressed in a finite difference form. In the present case, an alternating direction, implicit, finite difference scheme is employed. In view of the presence of

the nonlinear advective terms, a particular implicit scheme known as the Stabilizing Correction (SC) scheme is used. The basic idea of this scheme is as follows. The time level is indicated by a superscript r . The scheme involves variables at three time levels. The values of the variables at time levels $r-1$ and r are known from previous computations or prescribed initial conditions. To advance the solution from time level r to the new time level $r+1$, an intermediate time level solution denoted by the superscript $*$ is introduced. Equations 34-36 are operated in a two-step procedure. In the first step, the rectangular grid is swept in the $x(\alpha_1)$ direction, advancing the solution from time level r to $*$. Next, the grid is swept in the $y(\alpha_2)$ direction, advancing the solution from time level $*$ to $r+1$. The two sweeps together constitute a full time-step Δt .

33. Before details of the double sweep technique are discussed, the notation used for individual cells of the rectangular grid will be defined. Let Δx and Δy denote the cell dimensions in real space in the x and y directions, respectively. These dimensions may vary from cell to cell. Let the corresponding dimensions in computational space be $\Delta \alpha_1$ and $\Delta \alpha_2$. These dimensions are the same for all the cells in the grid. Let m and n denote indices corresponding to the center of an arbitrary cell (Figure 7). All the variables except the velocities U and V are defined at the cell centers. Velocities U and V are defined at cell faces $m+(1/2)$ and $n+(1/2)$, respectively. In the x -sweep, the x -momentum equation is centered about the cell face $m+(1/2)$, and the continuity equation is centered about the center of the cell. The two equations are solved, using in the process the result $U^* = U^{r+1}$. At the end of this sweep, $\bar{\eta}^*$ and U^{r+1} are known. Next the grid is swept in the y direction. In this sweep, the y -momentum equation is centered about the cell face $n+(1/2)$ and the continuity equation about the cell center. Upon solving the two equations, the values $\bar{\eta}^{r+1}$ and V^{r+1} for each cell are obtained. Thus the two sweeps together complete the solution for $\bar{\eta}^{r+1}$, U^{r+1} , and V^{r+1} .

34. Even though the SC scheme has been described so far in terms of the x -, y -coordinate system for convenience, in reality the technique must be applied to the equations of motion in the computational α_1 , α_2 space. After the application of the technique, the following finite difference equations result. (Hereafter the bar over η is dropped for convenience.)

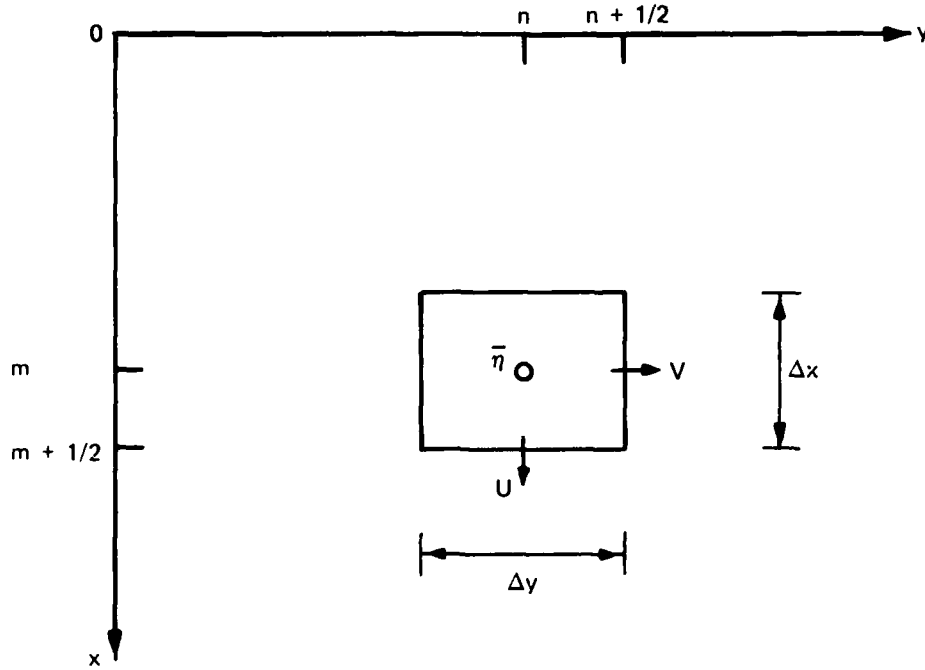


Figure 7. Cell notation

For the $\alpha_1(x)$ -sweep (taken along a grid cell column parallel to the α_1 -axis),

$$\begin{aligned}
 & \frac{1}{2\Delta t} \left(U^{r+1} - U^{r-1} \right) + \frac{U^r}{2\mu_x \Delta \alpha_1} \delta_{2\alpha_1}(U^r) + \frac{\bar{V}^r}{2\mu_y \Delta \alpha_2} \delta_{2\alpha_2}(U^r) \\
 & + \frac{g}{2\mu_x \Delta \alpha_1} \delta_{\alpha_1}(\eta^* + \eta^{r-1}) + \frac{c \left| \overline{u_{orb}} \right|^r U^{r+1}}{\bar{d}} + \frac{1}{\rho \bar{d}} \\
 & \times \left[\frac{1}{\mu_x \Delta \alpha_1} \delta_{\alpha_1} \left(S_{xx}^r \right) + \frac{1}{2\mu_y \Delta \alpha_2} \delta_{2\alpha_2} \left(\bar{S}_{xy}^r \right) \right] - \bar{\epsilon}_x \frac{1}{\mu_y} \frac{1}{\mu_x} \frac{1}{\Delta \alpha_2 \Delta \alpha_1} \delta_{\alpha_2 \alpha_1}(V^r) \\
 & - \bar{\epsilon}_y \left[\frac{1}{\left(\mu_y \Delta \alpha_2 \right)^2} \delta_{\alpha_2 \alpha_2}(U^r) + \frac{1}{2\mu_y (\Delta \alpha_2)^2} \delta_{\alpha_2} \frac{1}{\mu_y} \delta_{2\alpha_2}(U^r) \right] \\
 & - \frac{1}{2\mu_x \mu_y} \frac{1}{\Delta \alpha_2 \Delta \alpha_1} \delta_{2\alpha_2} \left(\bar{\epsilon}_x \right) \delta_{\alpha_1} \left(\bar{\eta}^r \right) = 0
 \end{aligned} \tag{37}$$

at $(n, m + 1/2)$

$$\frac{1}{2\Delta t} \left(\eta^* - \eta^{r-1} \right) + \frac{1}{2\mu_x \Delta \alpha_1} \delta_{\alpha_1} \left(U^{r+1} \bar{d}^r + U^{r-1} \bar{d}^r \right) + \frac{1}{\mu_y \Delta \alpha_2} \delta_{\alpha_2} \left(V^{r-1} \bar{d}^r \right) = 0 \quad \text{at } (n, m) \quad (38)$$

In the above equations, a single bar represents a two-point average and a double bar a four-point average. The difference operator δ_{α_i} is defined as

$$\delta_{\alpha_i}(Z) = Z_{\alpha_{i+1/2}} - Z_{\alpha_{i-1/2}} \quad (39)$$

for any variable Z . The definition may be extended to the operators $\delta_{2\alpha_i}$ and $\delta_{\alpha_i \alpha_j}$.

35. Equations 37 and 38 may be rearranged so that the unknown quantities are to the left and the known quantities are to the right, as follows:

$$-a_m \eta_{n,m}^* + \bar{a}_{m+1/2} U_{n,m+1/2}^{r+1} + a_{m+1} \eta_{n,m+1}^* = B_{m+1/2} \quad (40)$$

$$-a_{m-1/2} U_{n,m-1/2}^{r+1} + \eta_{n,m}^* + a_{m+1/2} U_{n,m+1/2}^{r+1} = A_m \quad (41)$$

where

$$a_m = a_{m+1} = \frac{g \Delta t}{(\mu_x)_{m+1/2} \Delta \alpha_1} \quad (42)$$

$$\bar{a}_{m+1/2} = 1 + \frac{2\Delta t c \langle \overline{u_{orb}} \rangle_{n,m+1/2}^r}{\bar{d}_{n,m+1/2}^r} \quad (43)$$

$$\begin{aligned}
B_{m+1/2} = U^{r-1} + \Delta t \left\{ - \frac{U^r}{\mu_x \Delta \alpha_1} \delta_{2\alpha_1} (U^r) - \frac{\bar{v}^r}{\mu_y \Delta \alpha_2} \delta_{2\alpha_2} (U^r) \right. \\
\left. - \frac{g}{\mu_x \Delta \alpha_1} \delta_{\alpha_1} (\eta^{r-1}) - \frac{2}{\rho d} \left[\frac{1}{\mu_x \Delta \alpha_1} \delta_{\alpha_1} (S_{xx}^r) + \frac{1}{2\mu_y \Delta \alpha_2} \delta_{2\alpha_2} (\bar{S}_{xy}^r) \right] \right. \\
\left. + 2\bar{\epsilon}_x \frac{1}{\mu_y \mu_x} \frac{1}{\Delta \alpha_2 \Delta \alpha_1} \delta_{\alpha_2 \alpha_1} (v^r) + 2\bar{\epsilon}_y \left[\frac{1}{(\mu_y \Delta \alpha_2)^2} \delta_{\alpha_2 \alpha_2} (U^r) \right. \right. \\
\left. \left. + \frac{1}{2\mu_y (\Delta \alpha_2)^2} \delta_{\alpha_2} \left(\frac{1}{\mu_y} \right) \delta_{2\alpha_2} (U^r) \right] \right. \\
\left. + \frac{1}{\mu_x \mu_y} \frac{1}{\Delta \alpha_2 \Delta \alpha_1} \delta_{2\alpha_2} \left(\bar{\epsilon}_x \right) \delta_{\alpha_1} \left(\frac{1}{v} \right) \right\} \text{ at } (n, m+1/2)
\end{aligned} \quad (44)$$

$$a_{m\pm 1/2} = \frac{\Delta t}{(\mu_x)_m \Delta \alpha_1} \bar{d}_{n, m\pm 1/2}^r \quad (45)$$

$$A_m = \eta^{r-1} - \frac{\Delta t}{\mu_x \Delta \alpha_1} \delta_{\alpha_1} (U^{r-1} \bar{d}^r) - \frac{2\Delta t}{\mu_y \Delta \alpha_2} \delta_{\alpha_2} (v^{r-1} \bar{d}^r) \text{ at } (n, m) \quad (46)$$

$$\bar{v}_{n, m+1/2}^r = \frac{1}{4} \left(v_{n-1/2, m}^r + v_{n+1/2, m}^r + v_{n-1/2, m+1}^r + v_{n+1/2, m+1}^r \right) \quad (47)$$

36. Consider the set of cells for which the index n is constant and equal to N . Suppose at the upper boundary cell ($m = M$), the velocity $U_{N, M+1/2}$ is always known. Similarly, suppose at the lower boundary cell ($m = L$) the water level $\eta_{N, L}$ is always known. Then the set of equations for all the cells can be written in the following matrix form if the common subscript N is dropped:

$$\begin{bmatrix}
 \bar{a}_{M+1/2} & a_{M+1} & 0 & 0 & \dots & 0 \\
 -a_{M+1/2} & 1 & a_{M+3/2} & 0 & \dots & 0 \\
 0 & -a_{M+1} & \bar{a}_{M+3/2} & a_{M+2} & \dots & 0 \\
 & & & & \dots & \\
 & & & & \dots & \\
 & & & & \dots & \\
 0 & 0 & 0 & \dots & -a_{L-1/2} & 1
 \end{bmatrix}
 \begin{bmatrix}
 U_{M+1/2}^{r+1} \\
 \eta_{M+1}^* \\
 U_{M+3/2}^{r+1} \\
 . \\
 . \\
 U_{L-1/2}^{r+1} \\
 \eta_L^*
 \end{bmatrix}
 =
 \begin{bmatrix}
 \hat{B}_{M+1/2} \\
 A_{M+1} \\
 B_{M+3/2} \\
 . \\
 . \\
 B_{L-1/2} \\
 \hat{A}_L
 \end{bmatrix}
 \quad (48)$$

where

$$\hat{B}_{M+1/2} \equiv B_{M+1/2} + a_M \eta_M^*$$

$$\hat{A}_L \equiv A_L - a_{L+1/2} U_{L+1/2}$$

37. Since the first matrix on the left hand side of Equation 48 is tri-diagonal, the above matrix equation can be solved by recursion. In general, the recursion relations may be written as

$$\eta_m^* = -P_m U_{m+1/2}^{r+1} + Q_m \quad (49)$$

$$U_{m-1/2}^{r+1} = -R_{m-1} \eta_m^* + S_{m-1} \quad (50)$$

where

$$\begin{aligned} P_m &= \frac{a_{m+1/2}}{T1} & Q_m &= \frac{A_m + a_{m-1/2} S_{m-1}}{T1} \\ R_m &= \frac{a_{m+1}}{T2} & S_m &= \frac{B_{m+1/2} + a_m Q_m}{T2} \end{aligned} \quad (51)$$

$$T1 = 1 + a_{m-1/2} R_{m-1}$$

$$T2 = \bar{a}_{m+1/2} + a_m P_m$$

38. Since in FORTRAN computer language fractional indices are not possible, a new integer index system is adopted in the program. Thus all the variables defined at the center and the faces $m+1/2$ and $n+1/2$ of a cell n,m will be designated by the integer indices N,M . The only exceptions are the expansion coefficients μ_x and μ_y which are defined at cell centers and faces. For these the following index system is adopted. For example, μ_x at the center of cell n,m is designated by the index $2M-1$, whereas μ_x at the face $m+1/2$ is denoted by the index $2M$, and similarly for μ_y . Using this new notation, the expanded form of the recursion coefficients for the $\alpha_1(x)$ -sweep may be written as follows:

$$P_M = \frac{\Delta t \bar{d}_{N,M}^r}{(\mu_x)_{2M-1} \Delta \alpha_1 T1} \quad (52)$$

$$Q_M = \frac{A_M + \frac{\Delta t \bar{d}_{N,M-1}^r}{(\mu_x)_{2M-1} \Delta \alpha_1} S_{M-1}}{T1} \quad (53)$$

$$R_M = \frac{g \Delta t}{(\mu_x)_{2M} \Delta \alpha_1 T2} \quad (54)$$

$$S_M = \frac{B_M + \frac{g \Delta t}{(\mu_x)_{2M} \Delta \alpha_1} Q_M}{T_2} \quad (55)$$

where

$$T_1 = 1 + \frac{\Delta t \bar{d}_{N,M-1}^r}{(\mu_x)_{2M-1} \Delta \alpha_1} R_{M-1} \quad (56)$$

$$T_2 = 1 + \frac{2 \Delta t c \left| \overline{u_{orb}} \right|_{N,M}^r}{\bar{d}_{N,M}^r} + \frac{g \Delta t}{(\mu_x)_{2M} \Delta \alpha_1} P_M \quad (57)$$

Using the same notation, the solution (Equations 49 and 50) may be written as

$$\eta_{N,M}^* = -P_M U_{N,M}^{r+1} + Q_M \quad (58)$$

$$U_{N,M-1}^{r+1} = -R_{M-1} \eta_{N,M}^* + S_{M-1} \quad (59)$$

For any given N , the recursion coefficients P , Q , R , and S are computed, using Equations 52-57, in succession between the boundaries in the direction of increasing $\alpha_1(x)$. The values of these coefficients at the boundaries depend on the types of boundary conditions encountered. Once all the coefficients for a given N have been determined, the values of η^* and U^{r+1} for all the cells in the column are computed, using Equations 58 and 59, in the direction of decreasing $\alpha_1(x)$. By continuing to progress to the next higher value of N , the whole grid is swept in the $\alpha_1(x)$ -direction.

39. The development of the finite difference equations and the recursion relations for the $\alpha_2(y)$ sweep is similar to that for the $\alpha_1(x)$ sweep. In this case, using the same notation as before, the recursion coefficients may be written as

$$P_N = \frac{\Delta t \bar{d}_{N,M}^r}{(\mu_y)_{2N-1} \Delta \alpha_2 T1} \quad (60)$$

$$Q_N = \frac{A_N + \frac{\Delta t \bar{d}_{N-1,M}^r}{(\mu_y)_{2N-1} \Delta \alpha_2} S_{N-1}}{T1} \quad (61)$$

$$R_N = \frac{g \Delta t}{(\mu_y)_{2N} \Delta \alpha_2 T2} \quad (62)$$

$$S_N = \frac{B_N + \frac{g \Delta t}{(\mu_y)_{2N} \Delta \alpha_2} Q_N}{T2} \quad (63)$$

where

$$T1 = 1 + \frac{\Delta t \bar{d}_{N-1,M}^r}{(\mu_y)_{2N-1} \Delta \alpha_2} R_{N-1} \quad (64)$$

$$T2 = 1 + \frac{2 \Delta t c \langle |u_{orb}| \rangle^r_{N,M}}{\bar{d}_{N,M}^r} + \frac{g \Delta t}{(\mu_y)_{2N} \Delta \alpha_2} P_N \quad (65)$$

The corresponding solution may be expressed as

$$\eta_{N,M}^{r+1} = -P_N v_{N,M}^{r+1} + Q_N \quad (66)$$

$$v_{N-1,M}^{r+1} = -R_{N-1} \eta_{N,M}^{r+1} + S_{N-1} \quad (67)$$

Initial and boundary conditions

40. An initial condition of rest was used in the wave-induced current and setup model. Thus $\bar{\eta}$, U , and V were zero at the start of the calculations. Radiation stress gradients were then gradually built up to their full values over a number of time-steps. The gradual buildup helped avoid transients caused if the system were "shocked" by the sudden application of radiation stress gradients. The solution was stopped when a steady state was reached. Although the model has the capability to allow flooding of dry land, wave setup was not great enough to cause flooding of the grid cells used for Oregon Inlet. Thus along the shoreline a "no flow" (wall) condition was assumed at the still-water line, and no flooding of the beach was allowed. For the lateral boundaries, a flux type boundary condition was used. That is, the flux at a boundary cell was made equal to that at the next interior cell.

41. On the offshore boundary, it is common practice to use conditions of either "no flow" (wall) or constant elevation. However, both of these conditions are highly reflective; and, as a result, the transients that develop during the start-up of the numerical solution tend to bounce back and forth between the offshore and nearshore boundaries and take a long time to damp out. Figure 8 shows a typical transient developed for such a case. These transients are evident in the results (Figure 9) presented by Ebersole (1980). They produce significant problems in sediment transport models. For example, for fixed wave conditions a steady state should develop such that there is no on- or offshore movement of water along a straight coastline. If transients are present that reflect between the coastline and the offshore boundary, a steady condition of no flow in the on- or offshore direction is not achieved. If steady state is assumed, cells will have small but steady currents in on- and offshore directions that will produce steady erosion and deposition.

42. To eliminate the problem with transients, a radiation boundary condition was used in the wave-induced current and setup model. This condition allowed transients to propagate out of the computational grid.

43. The radiation boundary condition was tested by considering a simple plane beach. Ebersole (1980) noticed oscillations in the wave setup at the beach (Figure 9), in the velocity in the offshore direction (Figure 10) and in the longshore velocity (Figure 11). Considering similar wave conditions, the model described in this report was run with the radiation boundary condition.

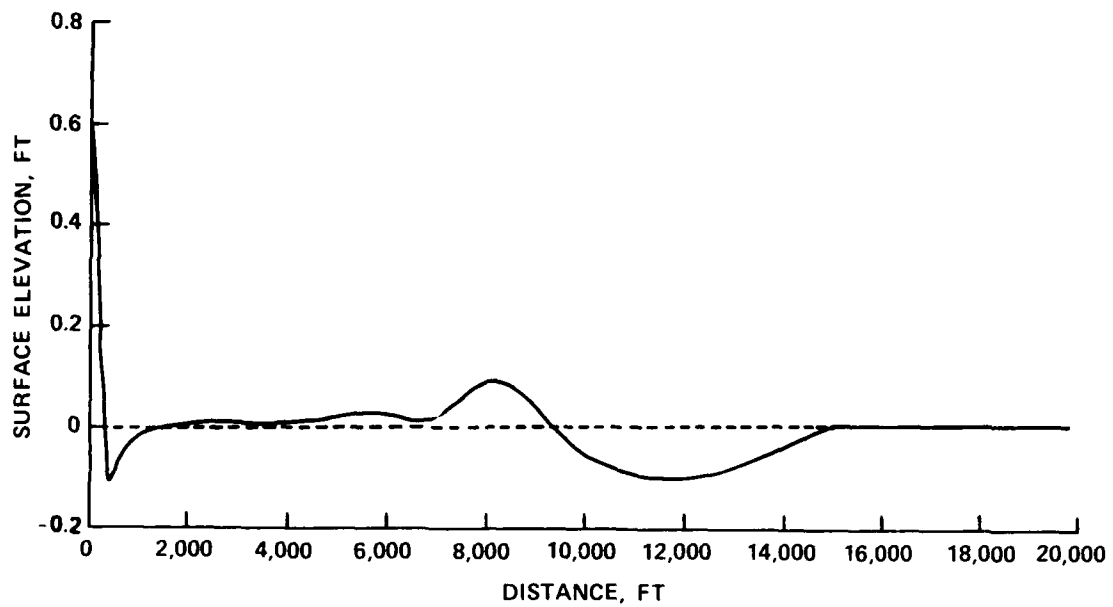


Figure 8. Setup and free gravity wave

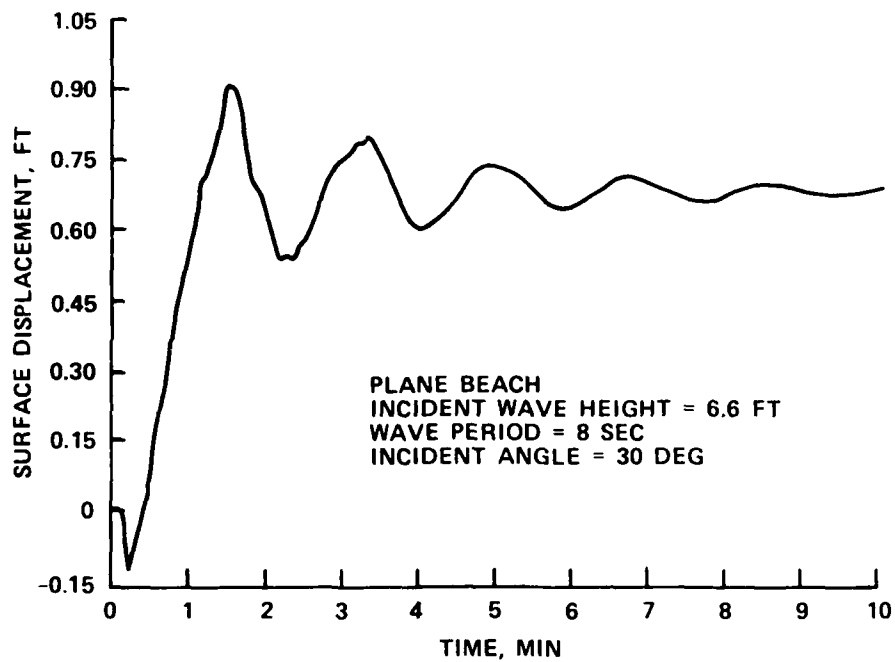


Figure 9. Wave setup (Ebersole and Dalrymple 1980)

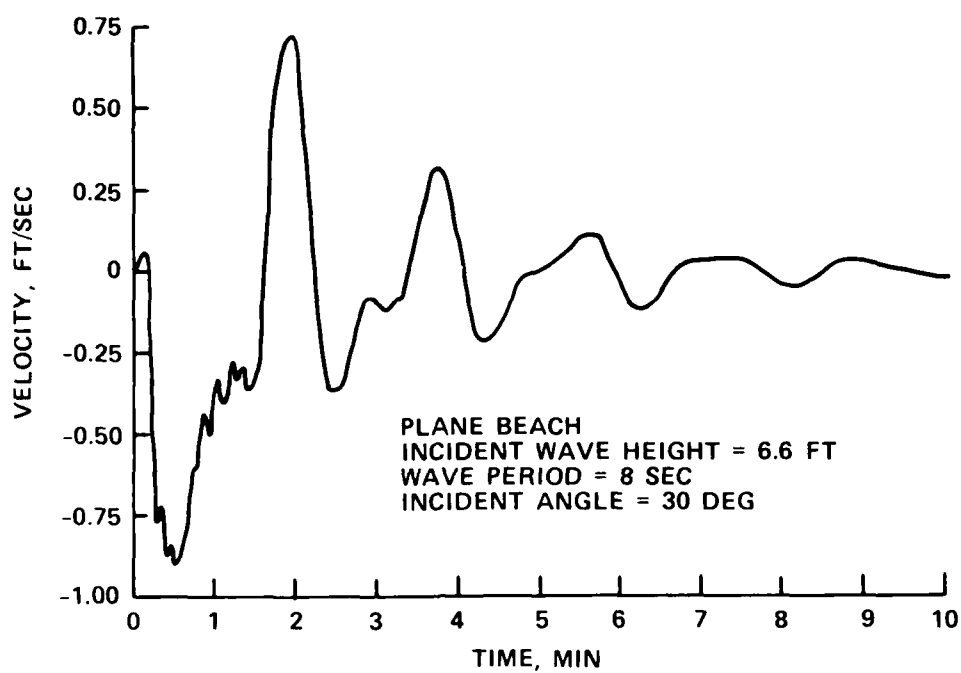


Figure 10. Velocity in offshore direction
(Ebersole and Dalrymple 1980)

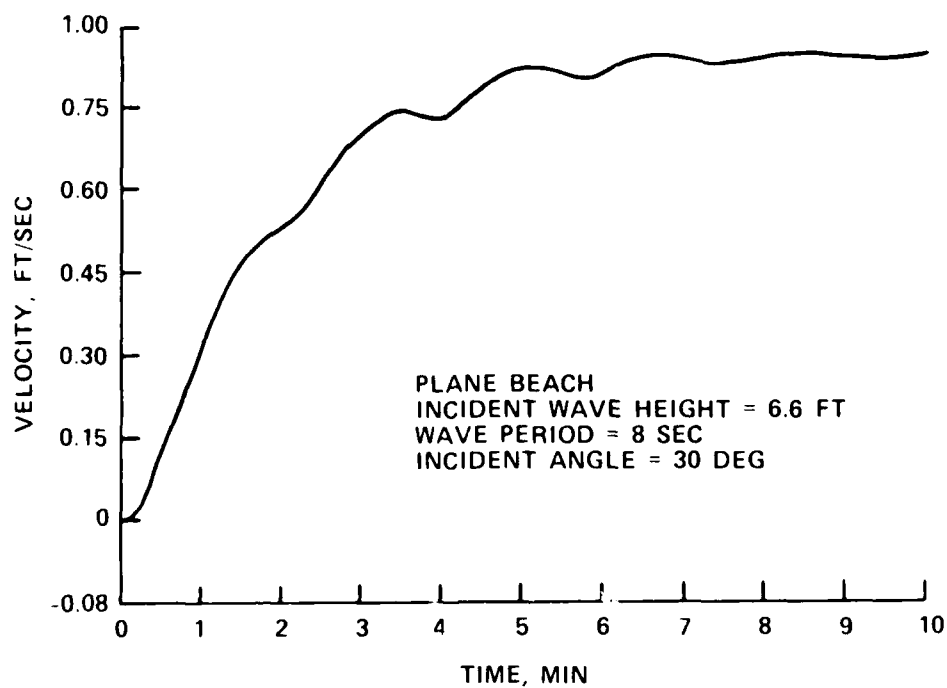


Figure 11. Longshore velocity (Ebersole and Dalrymple 1980)

Wave setup reached a steady-state (non-oscillating) value after approximately 7-8 min (Figure 12), the velocity in the offshore direction reached a steady zero value (velocity should be exactly zero) after approximately 7-8 min (Figure 13), and the longshore current reached a steady value after 11-12 min (Figure 14). These tests demonstrated how well the radiation boundary condition worked.

Model tests

44. The wave-induced current and setup model was tested by considering plane beach problems where either laboratory data or analytic solutions were available. The first test considered wave setup and was run for a case of normal wave incidence on a plane smooth laboratory beach. The laboratory tests were conducted by Bowen, et al. (1968). Waves with a period of 1.14 sec and deepwater wave height of 6.45 cm were propagated on a 1 on 12 beach slope. The numerical model used a 50 by 3 variable rectangular grid which represented the entire 40-m-long laboratory flume. Walls were used for the lateral boundaries as well as the offshore boundary in order to correspond to the laboratory situation. The solution allowed for the effect of setup on the wave heights in the surf zone. The solution was an iterative process since the setup depends upon wave heights which in turn depend upon setup. As the solution proceeded, the wave heights for cells in the surf zone were computed for each time-step by using $H = \gamma(h + \bar{\eta})$, where $\bar{\eta}$ is the setup and γ is a breaking index. The radiation stresses were changed accordingly. As suggested by Bowen, et al. (1968), a γ of 1.15 was used. A spin-up time of $10\Delta t$ was used.

45. A comparison of the steady-state setup values from the numerical model (after $150 \Delta t$) with those observed by Bowen, et al. (1968) is shown in Figure 15. There is excellent agreement in the offshore region. In the surf zone, the numerical model predicts higher setups than observed. This is not surprising since the numerical model did not allow flooding and runup. The slope of the mean water line in the surf zone is very similar in the laboratory measurements and numerical model results (Figure 15).

46. A second test case considered was that of waves approaching a plane beach at an angle. The deepwater angle of approach θ was 20 deg, the deepwater wave height was 10 ft, and the period was 12 sec. A plane beach with a constant bottom slope of 1 on 30 was used. A drag coefficient c of 0.01 and a breaking index γ of 0.82 were used. Lateral mixing and advection were

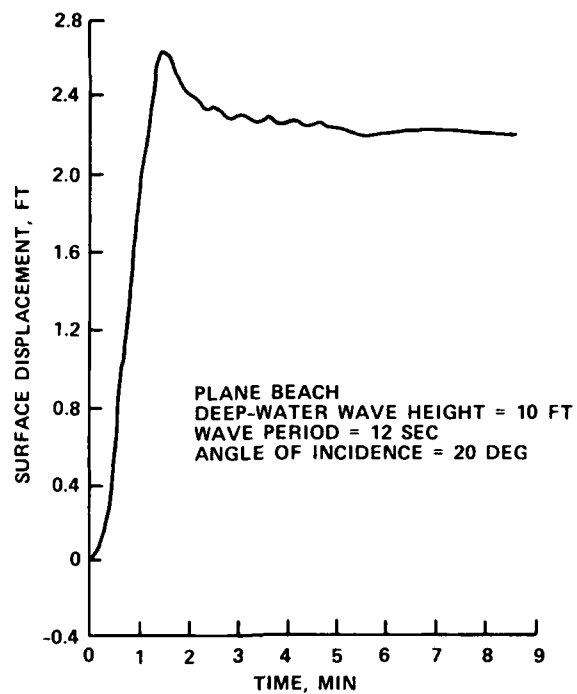


Figure 12. Wave setup, WES calculations

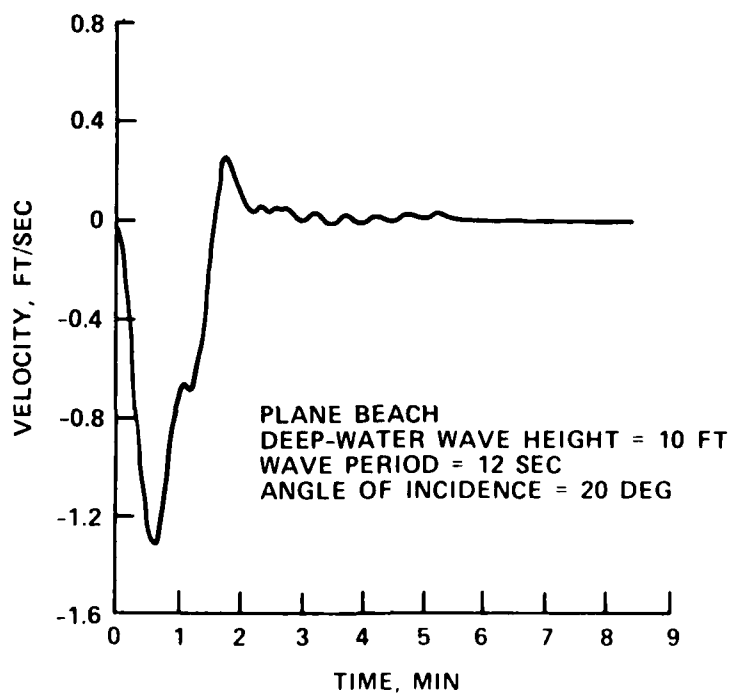


Figure 13. Velocity in offshore direction, WES calculation

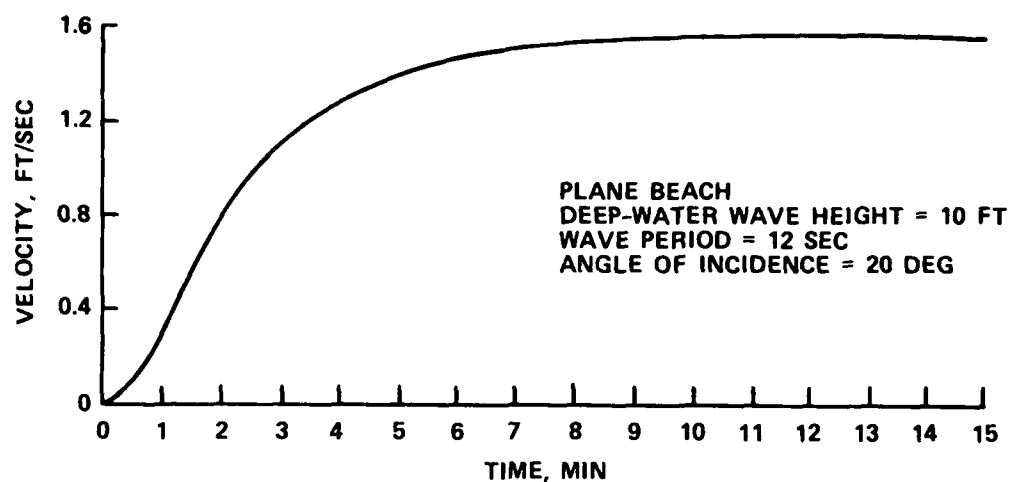


Figure 14. Longshore velocity, WES calculations

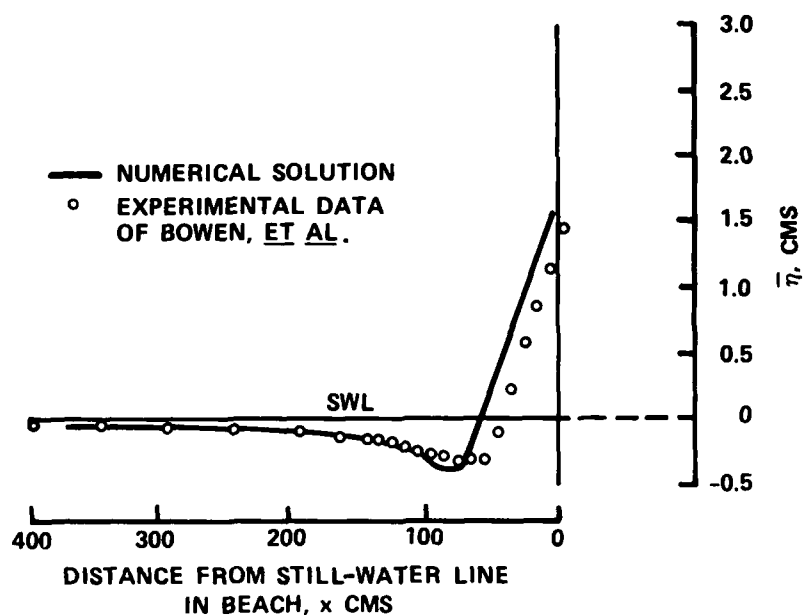


Figure 15. Comparison of numerical solution for setup with experimental data

neglected in the calculations to allow comparisons with an analytical solution of Longuet-Higgins (1970). Using a 100 by 6 uniform grid with $\Delta x = \Delta y = 60$ ft, and a time-step of 0.5 sec, a steady-state longshore velocity distribution was obtained after a time of $800 \Delta t$. Next, the same case was rerun

with a finer grid ($\Delta x = \Delta y = 30$ ft) and a time-step of 0.25 sec. Figure 16 shows a comparison between the numerical model calculations for longshore current and the analytical solution of Longuet-Higgins (1970). As the cell size and time-step are reduced, the numerical solution approaches the analytical solution of Longuet-Higgins. The grid cell size and time-step would have to approach zero for the solutions to agree identically, since the Longuet-Higgins analytical solution has an infinite gradient at the breaker line that only can be resolved with infinitely small grid cells. Of course, when lateral mixing is considered, the infinite gradient disappears. Figure 17 shows the effect of lateral mixing on the numerical solution for longshore velocity distribution. The mixing parameter P was defined by Longuet-Higgins (1970) as

$$P = \frac{\pi}{Y} \frac{N \tan \beta}{c} \quad (68)$$

where $\tan \beta$ is the bottom slope of the plane beach and N is an empirical coefficient which varies between 0 and 0.016. $P = 0$ corresponds to no lateral mixing. Figure 17 presents the numerical solution for P between 0.01 and 0.4. For completeness, the analytical solution of Longuet-Higgins for $P = 0$ is also shown in the figure. Based upon laboratory data, Longuet-Higgins suggested that P varies generally in the range of 0.1 to 0.4. Increasing values of P (therefore increasing lateral mixing) reduce the magnitude of the peak velocity, move the location of the peak velocity closer to the shoreline, and increase the velocities offshore of the breaker line. Figure 17 demonstrates that the numerical solution does indeed exhibit the proper behavior.

47. To demonstrate an application of the wave-induced current and setup model to Oregon Inlet, a particular wave condition that occurred during the 1962 Ash Wednesday storm was selected. From the WESWIS, a wave with a height of 11.39 ft, period of 8.0 sec, and an angle θ of 51.1 deg in 60-ft depth was selected. This particular wave condition was selected since the angle of incidence is large, and thus it is a good test of the stability of the model for large angles of incidence and complex bathymetry. The wave propagation numerical model was used to calculate the wave height, direction of propagation, and wave number at every grid cell.

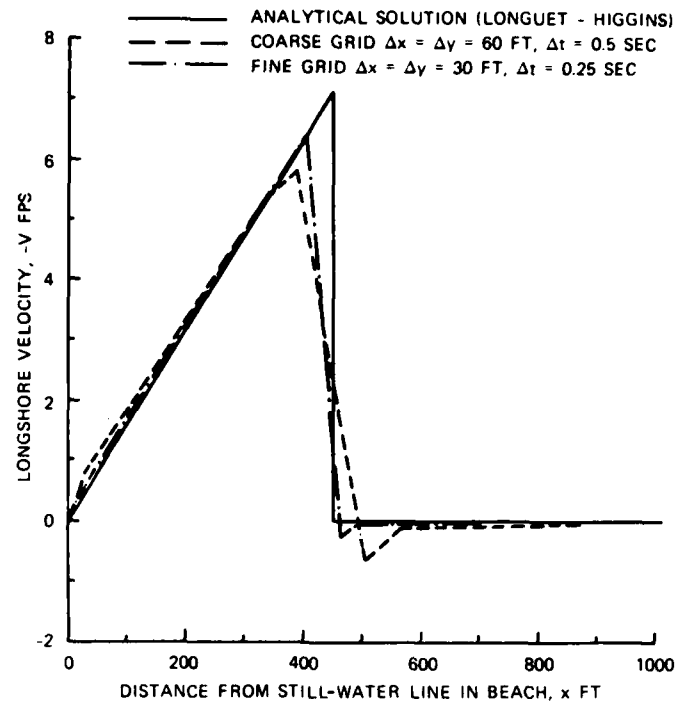


Figure 16. Comparison of numerical and analytical solutions for longshore current for plane beach

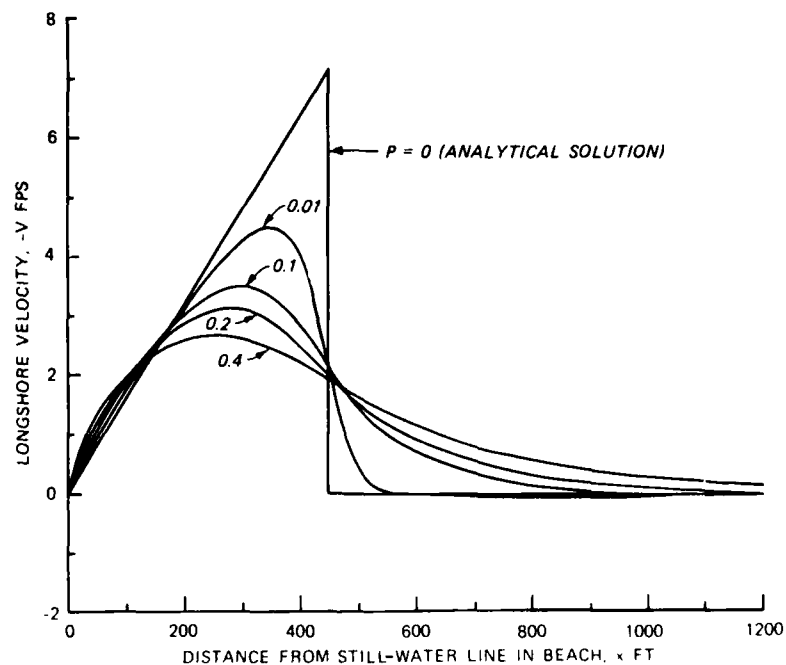


Figure 17. Effect of mixing parameter P on the numerical solution for longshore current for plane beach

48. A time-step of 18.0 sec and a drag coefficient c of 0.01 were used in the simulation. Figure 18 shows the bathymetry at Oregon Inlet. A steady-state condition was reached after a time of $67\Delta t$. Figure 19 shows the mean water levels (setup and setdown) and Figure 20 the velocities calculated by the model. The velocity vectors of Figure 18 are plotted just for every other cell in each coordinate direction to reduce the number of vectors and thus make velocity patterns more apparent. In addition, the plotting of velocities with magnitudes less than 0.1 ft/sec is suppressed.

49. Away from the inlet shown in Figures 18 and 19, the shoreline and the contours are approximately straight and parallel. Thus, there is a small setdown in the offshore area that is followed by a large setup. This is the expected setup and setdown pattern for a plane beach. The velocities shown in Figure 20 are mainly alongshore, and the velocity distribution is similar to that for a plane beach.

50. The setup, setdown, and velocity patterns are more complicated in the region of the inlet (the central part of the grid). Here the breaker line is farther offshore. The depth in the main channel decreases first and increases later in the direction of the inlet. Because of these factors, the water sets up around the inlet and tends to create a flow into the inlet through the various channels. A part of the main alongshore flow goes around the channels and shoals and thus bypasses the inlet.

51. Near the shoals, the patterns of mean water level and velocity are irregular. This is because the waves refract around the shoals and break, creating local setups and currents that do not necessarily conform to the general pattern. As the waves go toward the barrier islands, they sometimes re-form after breaking because the depth increases.

52. The central processor unit (CPU) time for running the Oregon Inlet grid to a steady-state condition was approximately 15.5 sec on a CRAY-1 computer. The total cost for the job, including program compilation, CPU time, and data file manipulation, was approximately \$10. Thus the wave-induced current and setup model is sufficiently efficient that it can be applied to large practical coastal and inlet problems. If instead of an alternating-direction implicit finite difference model that uses a variable grid (the model described in this report) an explicit finite difference model that uses a uniform grid were used in computations for Oregon Inlet, the computational requirements would have been approximately 3,000 times greater.

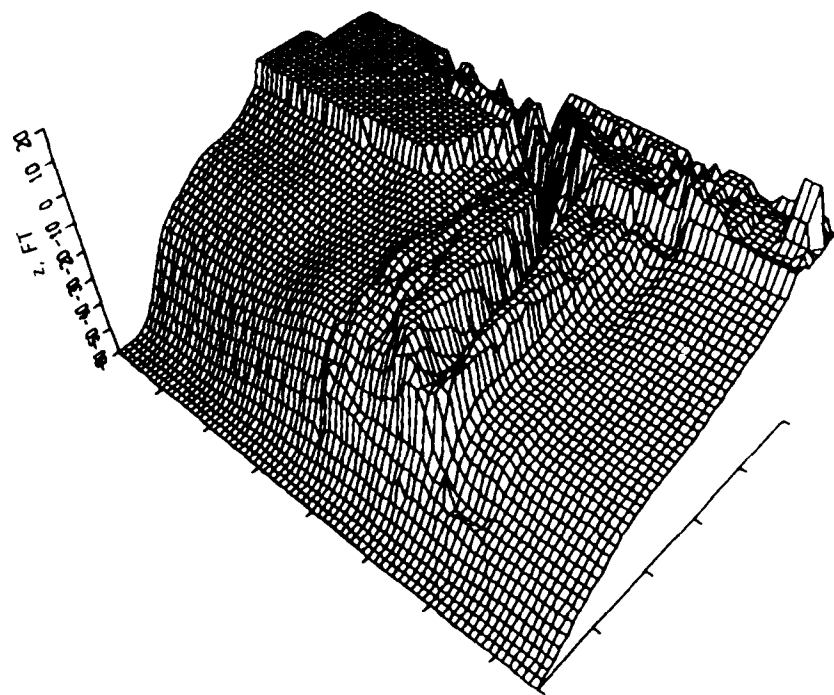


Figure 18. Topography used for Oregon Inlet numerical model simulation

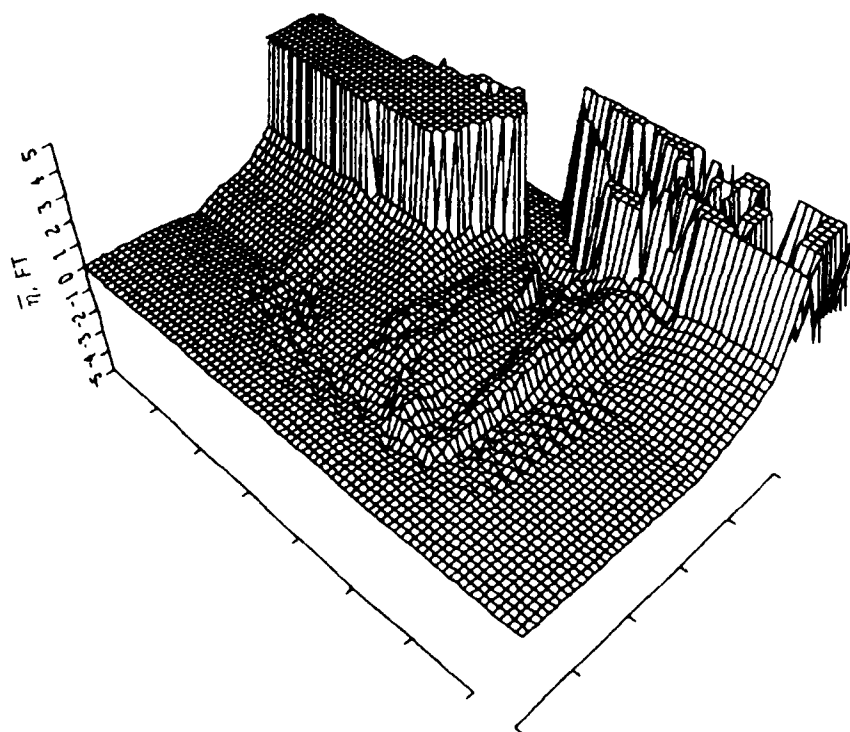


Figure 19. Mean water levels from Oregon Inlet numerical model simulation

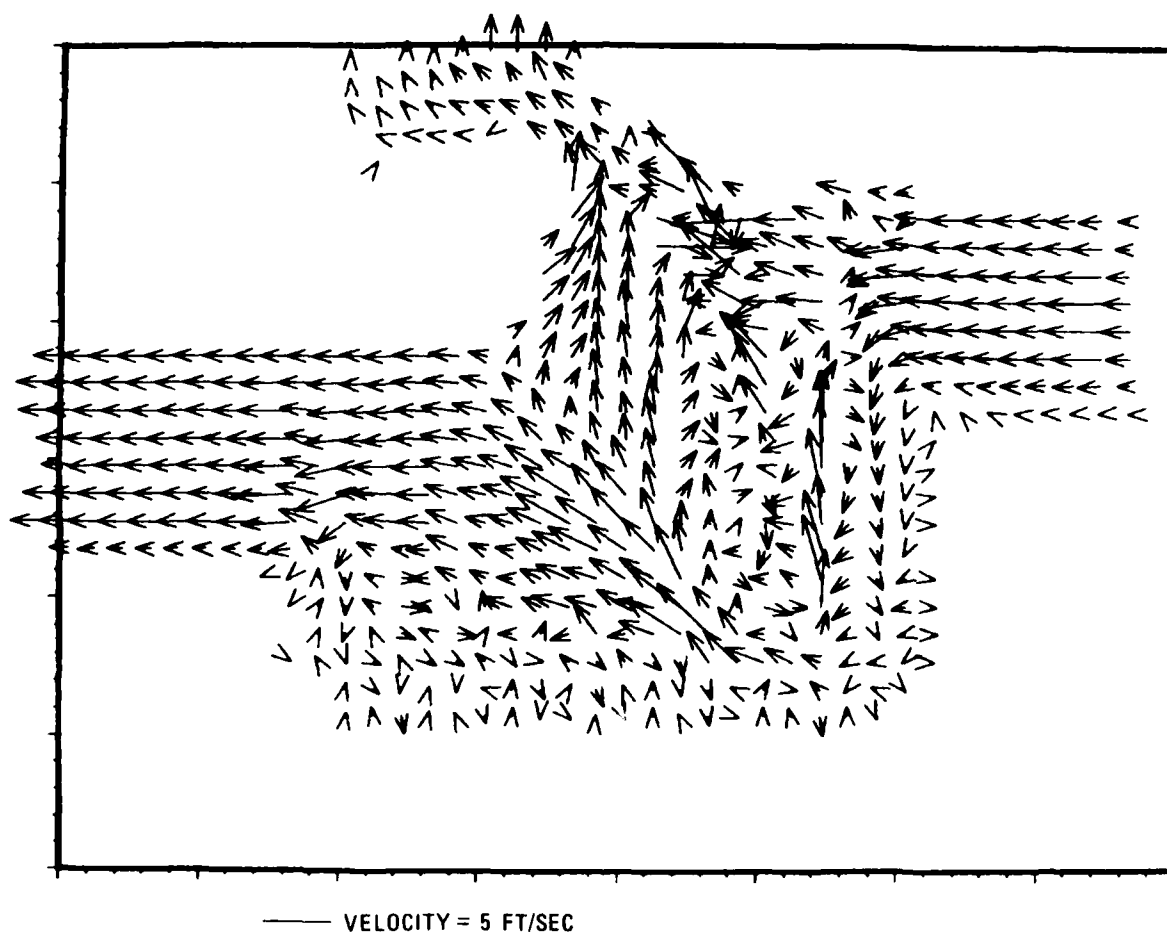


Figure 20. Velocity vector plot for Oregon Inlet simulation

Tidal and Storm Surge Models

53. Tidal and storm surge elevations and currents were determined using the WIFM model. These calculations were made in a separate WES study (Leenknecht, Earickson, and Butler 1984), and the results were provided for this study.

54. In order to perform tidal and storm surge calculations, a larger area must be modeled than that modeled by the CIP numerical modeling system. Figure 21 shows the limits of computational grids used for the tidal and storm surge computations. In addition, the limits of the shore processes grid used

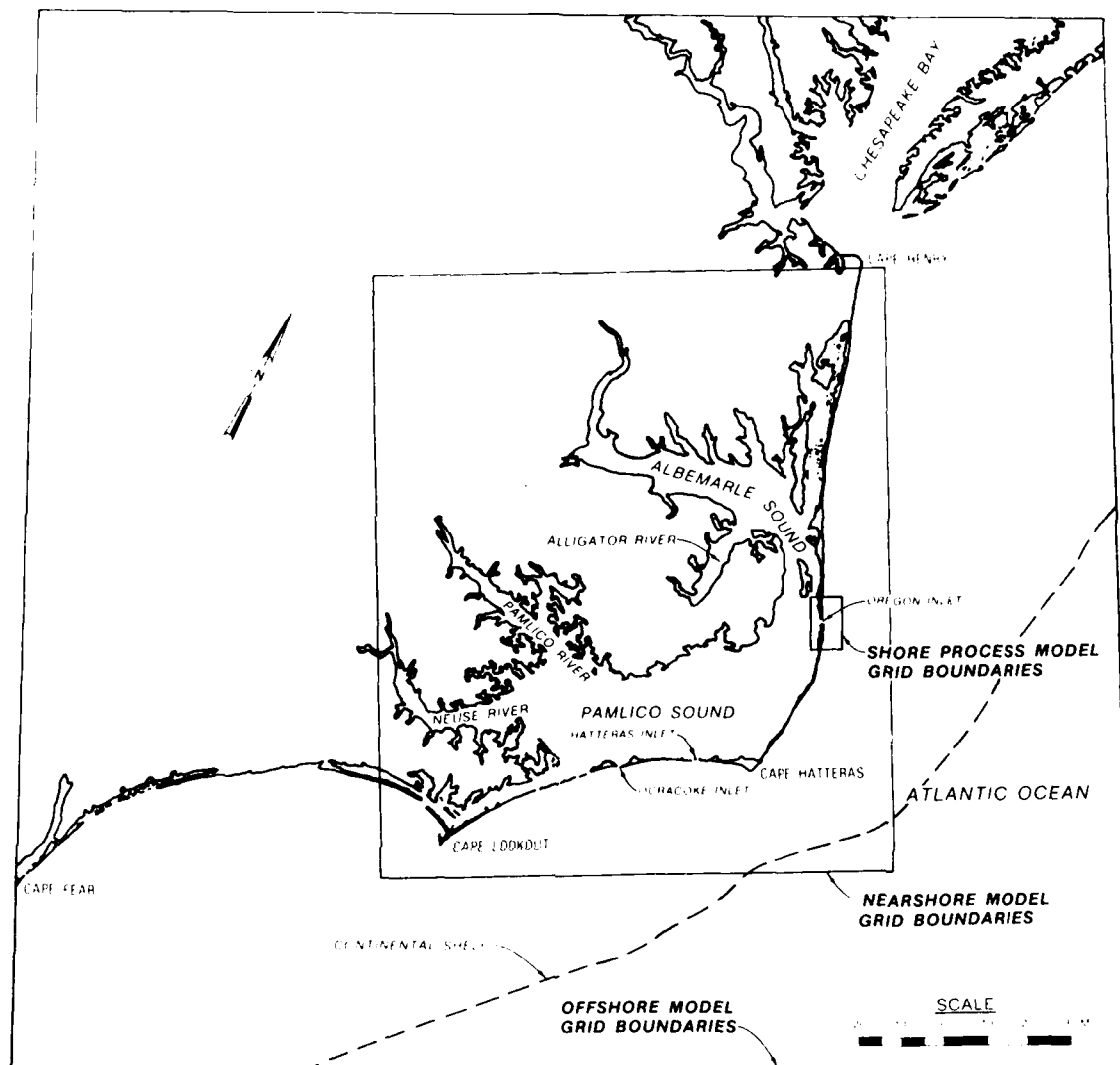


Figure 21. Numerical grids used for tidal and storm surge computations

in this study are shown. The storm surge ("offshore model") grid covers a very large area since it is necessary that the winds that produce the surge be modeled. Wind fields associated with storms can cover very large areas. The tidal grid ("nearshore model") covers a smaller area than the storm surge grid but a larger area than the shore processes grid. The tidal grid must cover a moderately large area in order to include all of the inlets that connect the sound areas with the ocean.

55. Tidal and storm surge computations performed on the grids shown in Figure 21 were used to provide boundary conditions for tidal and storm surge

computations performed on the shore processes grid. Figures 22 and 23 show typical tidal computations performed on the nearshore processes grid. The figures show mean ebb tidal currents for existing conditions and for two jetties with a 2,500-ft spacing. Only flows in the vicinity of the inlet are shown. Part of the ebb-tidal delta shoal was exposed at this time in the tidal cycle.

56. The numerical tide and surge model for Oregon Inlet (Leenknecht, Earickson, and Butler 1984) was used to simulate also storm surge elevations and currents for two storms of record, namely, Hurricane Donna (1960) and the 1962 Ash Wednesday storm. Results obtained for the 1962 Ash Wednesday storm were used in this study, as discussed in a later section.

Sediment Transport Models

Transport inside the surf zone

57. Inside the surf zone it is the wave breaking process that is primarily responsible for the transport of sediment. This process is quite complex and not well understood. There is even considerable disagreement on the primary mode (bed load or suspended load) of sediment transport in the surf zone (Komar 1978). Thus a model that determines transport in the surf zone must be empirical, to some degree, in its formulation.

58. The surf zone transport model developed in this study is based upon an energetics concept developed by Bagnold (1963) who reasoned that the wave orbital motion provides a stress that moves sediment back and forth in an amount proportional to the local rate of energy dissipation. Although there is no net transport as a result of this motion, the sediment is in a dispersed and suspended state so that a steady current of arbitrary strength will transport the sediment. Thus breaking waves provide the power to support sand in a dispersed state (bed and suspended load), while a superimposed current (littoral, rip, tidal) produces net sand transport.

59. Komar (1974) has given the following theoretical velocity distribution for a longshore current across the surf zone on a plane beach:

$$V = AX + B_1 X^P \quad \text{for } 0 < X < 1 \quad (69)$$

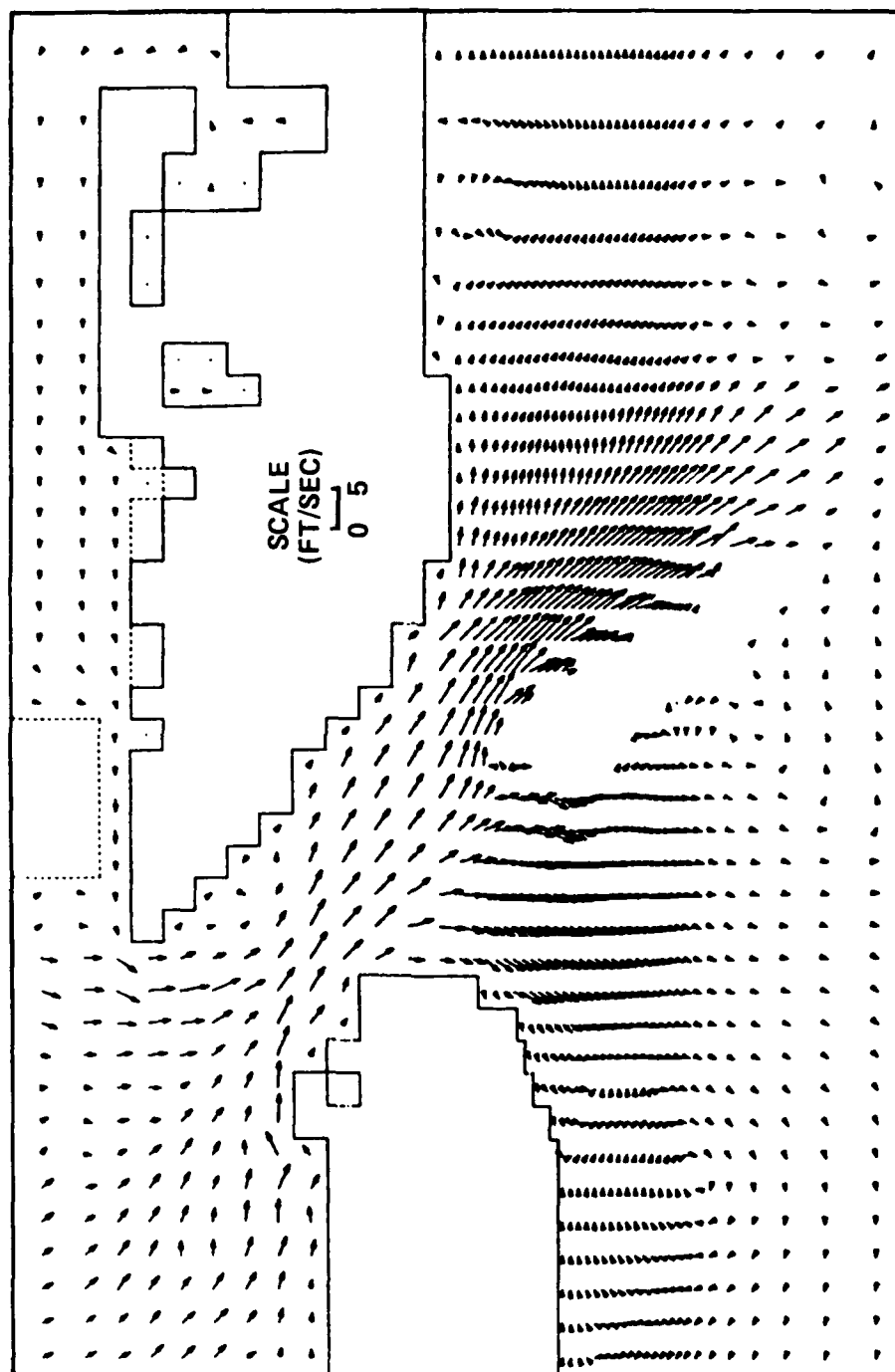


Figure 22. Ebb currents for existing conditions

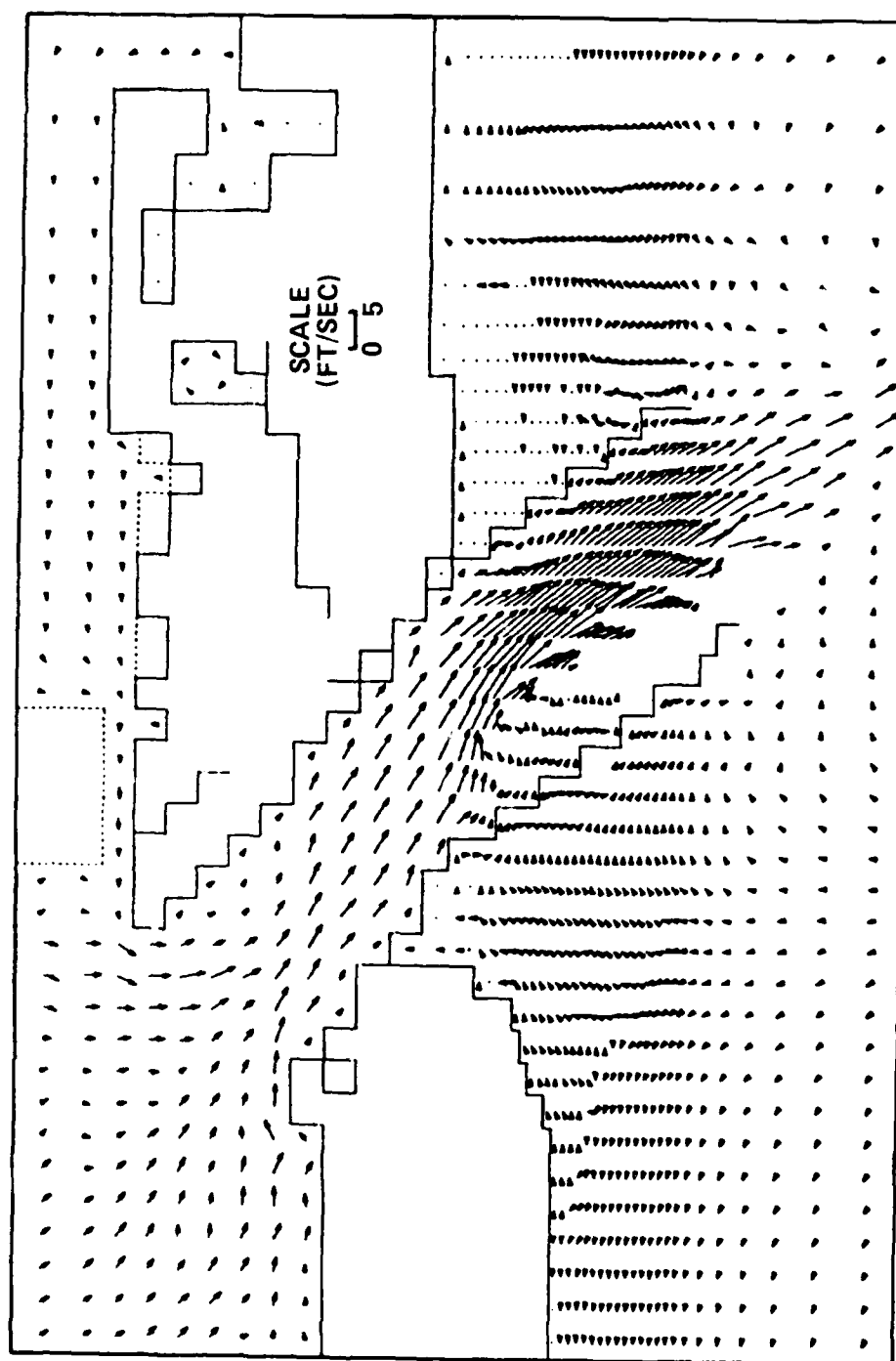


Figure 23. Ebb currents for 2,500-ft jetty spacing

where

$$V = \frac{v}{v_o} \quad \text{and} \quad X = \frac{x}{x_b} \quad (70)$$

v being the longshore current velocity at a distance x from the shoreline, x_b being the width of surf zone, and v_o being given by

$$v_o = \frac{5}{16} \gamma \zeta \sqrt{1 + \gamma} \sqrt{gh_b} \frac{\tan \beta}{c} \sin \theta_b \cos \theta_b \quad (71)$$

$$P_1 = -\frac{3}{4} + \sqrt{\frac{9}{16} + \frac{1}{\zeta P}} \quad (72)$$

$$P_2 = -\frac{3}{4} - \sqrt{\frac{9}{16} + \frac{1}{\zeta P}} \quad (73)$$

The coefficients in the solution are

$$A = \frac{1}{1 - 2.5 P \zeta} \quad (74)$$

$$B_1 = \frac{(P_2 - 1) A}{P_1 - P_2} \quad (75)$$

$$\zeta = \frac{1}{(1 + 0.375 \gamma^2)} \quad (76)$$

where $\tan \beta$ is the beach slope, P is the mixing parameter of Longuet-Higgins given by Equation 68, and γ is the breaker index. Using the above velocity distribution and noting that the total sediment transport rate Q_1 across the surf zone is given by

$$Q_1 = C_s \int_0^{x_b} v \, d \, dx \quad (77)$$

in which C_s is the average sediment concentration (dimensionless) across the surf zone, and d is the water depth, one may obtain the following result after integration:

$$Q_1 = C_s x_b^2 \frac{5\pi}{16} \gamma \zeta^2 \sqrt{1 + \gamma} \sqrt{gh_b} \left(\frac{\tan \beta}{c} \right) \sin \theta_b \cos \theta_b \tan \beta \left(\frac{A}{3} + \frac{B_1}{P_1 + 2} \right) \quad (78)$$

Equation 78 has the same functional form as Equation 4-50b of the Shore Protection Manual (SPM) (1984) if the group velocity at breaking is approximated by solitary wave theory and the units are converted as follows:

$$Q_1 = \frac{0.00642}{8} \rho g H_b^2 \sqrt{g h_b} (1 + \gamma)^{1/2} \sin \theta_b \cos \theta_b \quad (79)$$

The sediment concentration C_s can be obtained by equating Equations 78 and 79. That is,

$$C_s = \frac{0.0008 \rho g}{\zeta \left(\frac{\tan \beta}{c} \right) \left(\frac{A}{3} + \frac{B_1}{P_1 + 2} \right)} \left(\frac{H_b}{x_b} \right) \quad (80)$$

In computing C_s , the following relation for $(\tan \beta/c)$ is used:

$$\frac{\tan \beta}{c} = \frac{1.38}{\zeta} \frac{(1 - 2.5 P \zeta)}{\left[\frac{1}{2} + \frac{1}{2 P_1} \left(\frac{P_2 - 1}{P_1 - P_2} \right) \right] (1 + \gamma)^{1/2}} \quad (81)$$

Since for a particular wave condition H_b and x_b are known from the wave model, C_s is known for the surf zone.

Transport beyond the surf zone

60. Beyond the surf zone, waves are not breaking. Currents (tidal, littoral, rip) still transport sediment, but the sediment load is much smaller than the load in the surf zone. Waves still assist in providing power to support sand in a dispersed state. However, there is little turbulent energy dissipation, and frictional energy dissipated on the bottom represents most of the energy dissipation. Bed load is the primary mode of sediment transport beyond the surf zone according to Thornton (1972).

61. Since beyond the surf zone it is the tractive forces of currents (including wave orbital velocity currents) that produce sediment movement, a sediment transport by currents approach is taken. Again, since the complete physics of the problem is not completely understood, a semiempirical approach must be taken. In this study, the approach of Ackers and White (1973) is followed after appropriate modification for the influence of waves.

62. Ackers and White (1973) studied sediment transport due to currents. They used the results of 925 individual sediment transport experiments to

establish various empirical coefficients. The approach considers both suspended load and bed load. It is assumed that the rate of suspended load transport is dependent upon the total shear on the bed. Therefore, the shear velocity v_* is the important velocity for suspended load transport. Bed load transport, however, is assumed to depend upon the actual shear stress on individual sediment grains. Ackers and White (1973) assume that this stress is comparable with the shear stress that would occur on a plane granular surface bed with the same mean stream velocity. Thus the mean velocity of flow v is the important velocity for bed load transport.

63. Considering only currents (not waves), Ackers and White (1973) derived sediment transport rate in a dimensionless form. For convenience in practical application, this may be written as:

$$S = \frac{v}{(1-p)} D \left(\frac{v}{v_*} \right)^{n_1} \frac{C}{A^{m_1}} (F - A)^{m_1} \quad (82)$$

where

S = total sediment transport rate per unit width (vertically integrated combined bed and suspended sediment load) ($\text{ft}^3/\text{sec}/\text{ft}$)

D = sediment diameter which is exceeded in size by 65 percent (by weight) of the total sample

$$C = \exp \left[2.86 \ln Y - 0.4343 (\ln Y)^2 - 8.128 \right] \quad (83)$$

$$Y = D \left[\frac{g(s-1)}{v^2} \right]^{1/3} \quad (84)$$

s = mass density of sediment relative to that of the fluid

$$n_1 = 1.0 - 0.2432 \ln Y \quad (85)$$

$$m_1 = \frac{9.66}{Y} + 1.34 \quad (86)$$

$$F = \frac{v \left(\frac{v_*}{v} \right)^{n_1} \left(\sqrt{32} \log \frac{10 h}{D} \right)^{n_1-1}}{\left[g(s-1)D \right]^{1/2}} \quad (87)$$

$$A = \frac{0.23}{Y^{1/2}} + 0.14 \quad (88)$$

ν = kinematic viscosity of fluid

p = porosity of sediment

For values of Y greater than 60, C , n_1 , m_1 , and A have the values 0.025, 0, 1.5 and 0.17, respectively.

64. The Ackers and White formulation modified for waves has been used in the past to determine sediment transport within surf zone areas (e.g., Swart 1976, van de Graaff and van Overeem 1979, Willis 1978, and Swart and Fleming 1980). It would appear, however, to be questionable to assume that an approach developed to determine sediment transport by current action would be appropriate to handle sediment transport in an area where turbulence due to wave breaking is the major mechanism for placing sediment in a state that allows transport by currents. However, outside the surf zone where waves are nonbreaking, the influence of waves is to increase the velocity of flow felt by sediment grains. Thus it is reasonable to use in the latter region a current action approach that is modified to consider also the current action exerted on the bottom by waves.

65. Swart (1976) assumed that suspended load was the main sediment transported in the surf zone. Therefore, he modified the shear velocity to account for waves by increasing the shear velocity as follows:

$$(v_*)_{\text{waves and current}} = (v_*)_{\text{current}} \left[1 + \frac{1}{2} \left(\xi_1 \frac{u_o}{v} \right)^2 \right]^{1/2} \quad (89)$$

where

$$\xi_1 = C_1 (fw_1/2g)^{1/2} \quad (90)$$

$$C_1 = 18 \log \left(\frac{12h}{r_1} \right) \quad (91)$$

fw_1 = Jonsson's (1966) friction factor based on bed roughness r_1

u_o = wave orbital velocity

Equation 89 was originally developed by Bijker (1967) and modified by Swart (1974a).

66. Van de Graaff and van Overeem (1979) noted that within the surf zone both suspended and bed load are significant and thus concluded that Swart's approach was not correct. They proposed increasing the mean velocity of flow in addition to the shear velocity by using the following equation:

$$(v)_{\text{wave and current}} = (v)_{\text{current}} \left[1 + \frac{1}{2} \left(\xi_2 \frac{u_o}{v} \right)^2 \right]^{1/2} \quad (92)$$

where

$$\xi_2 = C_2 \left(\frac{f w_2}{2g} \right)^{1/2} \quad (93)$$

$$C_2 = 18 \log \left(\frac{10h}{D} \right) \quad (94)$$

$f w_2$ = Jonsson's friction factor with D as bed roughness

Equation 92 was developed also by Bijker (1967) and modified by Swart (1974a).

67. Beyond the surf zone where waves are nonbreaking, the waves do not increase the level of turbulence since turbulence is confined to a narrow boundary layer by the oscillating wave orbital velocities. Since the shear velocity is dependent upon the intensity of turbulence and thus the total energy degradation rather than the net traction on individual sediment grains, the shear velocity is not changed by wave action. With the wave-induced turbulence confined to a narrow boundary layer and the waves propagating essentially without energy loss, the effect of waves is to increase the traction on individual grains by increasing the mean velocity felt by the grains. Thus the mean velocity of flow must be increased according to Equation 92. However, the shear velocity must remain unchanged. Thus Equation 82 becomes

$$S = \frac{v}{1-p} D \left\{ \frac{v \left[1 + \frac{1}{2} \left(\xi_2 \frac{u_o}{v} \right)^2 \right]^{1/2}}{v_*} \right\}^{n_1} \frac{C}{A^{m_1}} (F - A)^{n_1} \quad (95)$$

with

$$F = \frac{\left\{ v \left[1 + \frac{1}{2} \left(\xi_2 \frac{u_o}{v} \right)^2 \right]^{1/2} \right\}^{1-n_1} v_*^{n_1} \left(\sqrt{32} \log \frac{10h}{D} \right)^{n_1-1}}{[g(s-1)D]^{1/2}} \quad (96)$$

Equations 95 and 96 were used in the present numerical study for calculating longshore transport beyond the surf zone.

Erosion and deposition

68. In this report we are considering only the transport of noncohesive sand sediments. These sediments have relatively large fall velocities and thus remain in suspension (as suspended or bed load) for only short periods of time unless a forcing function is continually in effect. Thus these sediments act differently from cohesive sediments that may move considerable distances before returning to the ocean floor. For cohesive sediments, the concentration of sediment at a particular location may depend upon more than just the local forcing function. It may also depend upon the concentrations at other locations and flow patterns. For example, large wave activity at one location can produce a large concentration of cohesive sediments. These sediments can then be carried to an area of low wave activity and still remain in suspension for a long period of time so that the concentration is high in an area of low wave activity.

69. In the case of noncohesive sediments, if a parcel of water with a high concentration of noncohesive sediment (e.g., as a result of large wave activity) enters a region of low wave activity, the material drops rapidly out of suspension, and a much smaller quantity of sediment is resuspended. Thus in any given grid cell (with dimensions larger than the typical horizontal distances that noncohesive sediments travel when they drop out of suspension), the quantity of sediment being transported is a function of the wave and current activity within the cell. If adjacent cells supply sediment to the cell in greater quantities than the wave and current activity in the cell can support, then part of the sediment deposits in the cell and only the sediment that can be transported by the local waves and currents within the cell are transported through the cell. Conversely, if the cell can transport greater quantities of material than is supplied by adjacent cells, then erosion must occur within the cell as bottom material supplies the additional required material. For example, if an offshore breakwater is built, sediment will deposit in its lee where wave activity is lower than in adjacent areas. If something increases wave convergence in an area, erosion will occur.

70. Since the rate of noncohesive sediment transport within a cell is dependent only upon wave and current conditions within the cell, transport can be modeled using a "box model." In this model, the transport in and out of

the four faces of a cell must be considered. If more material enters a cell than leaves, deposition of material occurs, and if more material leaves than enters, erosion of material occurs within the cell. If S_{out} is the total transport rate out of a cell and S_{in} is the total transport rate into a cell, then

$$\Delta h = \frac{(S_{in} - S_{out})\Delta t}{A_c(1 - p)} \quad (97)$$

where

Δh = change in the bed elevation of a cell

Δt = time-step

A_c = area of cell

p = porosity of sediment on bed

71. When applied to each grid cell of the grid shown in Figure 2, Equation 97 determines the erosion and deposition throughout the grid. It is assumed that there is no net erosion or deposition within all the boundary cells. S_{in} and S_{out} can be determined once the current and wave fields have been determined by the numerical models described earlier. Within the surf zone, both the sediment concentration C_s and the total water discharges (tidal and wave-induced) are used to compute S_{in} and S_{out} .

Profile Response (Onshore-Offshore) Model

Introduction

72. In addition to littoral and tidal transport, beach profiles respond to the wave climate through onshore-offshore transport of sediment. This onshore-offshore transport occurs at a much (orders of magnitude) slower rate than does littoral transport of sediment (Galvin 1983). However, although the gross littoral transport of sediment is very large at any point in the surf zone, the net deficit or surplus of sediment is usually fairly small. Conversely, the gross onshore-offshore transport of sediment is small, but the net deficit or surplus can be equal to the gross over short periods of time. For example, during a storm there may be offshore movement of sediment to an offshore bar. Although the total amount of sediment that moves to the bar is

small compared to the total gross yearly littoral transport, all of the sediment that is transported must be eroded from the nearshore area.

73. The onshore-offshore transport of sediment is not well understood. Attempts have been made in recent years to establish the equations governing onshore-offshore transport and solve them using numerical models. However, none of these attempts has produced a numerical model that can be used for reliable quantitative predictions of onshore-offshore transport. For example, Wang (1981) evaluated onshore-offshore models developed in recent years by Sunamura (1980), Dally (1980), and Yang (1981). Wang concluded that "Beach profile modeling is a quite recent endeavor. It is a difficult problem because the physical process is complicated and is not well understood. The three models introduced here are not at operational level and are not adequate for quantitative predictions."

74. Since the equations governing onshore-offshore transport are not completely known, in this study a numerical model is developed that is strongly based upon concepts developed by Swart of the Delft Hydraulics Laboratory, the Netherlands (Swart 1974a, 1974b, and 1976). Swart's concepts were extended to allow the model to consider a variable datum (time-varying tide), a variable wave climate, and onshore transport in addition to offshore transport (Swain and Houston 1983, 1984a, 1984b, and Swain 1984).

Governing equations

75. In his conceptual model, Swart divided a normal beach profile into three zones (Figure 24), each with its own transport mechanism. The first zone is a backshore above the limit of wave runup. If windblown sediment transport is neglected, there is no transport in this zone. The second zone is a developing profile (D-profile) where a combination of bed-load and suspended load transport takes place. The dividing point between these two zones is the highest location that waves reach on the beach. Since the tide datum and wave climate vary with time, this dividing point moves with time. The position of maximum runup was determined empirically by Swart and is given by the following equation (all units are metric):

$$h_o = 7650 D_{50} \left[1 - \exp \left(\frac{-0.000143 H_{mo}^{0.488} T^{0.93}}{D_{50}^{0.786}} \right) \right] \quad (98)$$

where

D_{50} = median particle diameter

H_{mo} = maximum wave height in the spectrum (equal to twice the significant wave height)

T = wave period

The third zone is the transition area seaward of the D-profile and landward of the point where sediment motion is initiated by wave action. Bed-load transport is normally the only transport in this zone. The point dividing the lower limit of the D-profile and the upper limit of the transition area was determined empirically by Swart, and the depth of this point is given by the following equation:

$$h_m = 0.0063 \lambda_o \exp \left(\frac{4.347 H_o^{0.473}}{T^{0.894} D_{50}^{0.093}} \right) \quad (99)$$

where λ_o is the deepwater wave length and H_o is the deepwater wave height.

76. The basic assumption in the theory of Swart is that the D-profile will eventually reach a stable situation under constant wave attack. This stable situation implies both an equilibrium form and position of the beach profile. By considering many small- and full-scale tests of profile development under wave attack, Swart was able to develop equations that determine the form and position of the equilibrium profile for different incident wave climates.

77. At every location "i" on the D-profile, Swart defines an onshore and offshore segment of the profile (Figure 24). The length of the onshore profile is represented schematically by the distance L_{1i} and the length of the offshore profile by L_{2i} . The length difference at each point i between the onshore and offshore sections of the D-profile, $(L_2 - L_1)_i$, is the key parameter used by Swart to characterize a profile. The value of this parameter when the profile is in equilibrium is defined as W_i . Swart thus represents the equilibrium profile by a "W-curve". He defines the W_i value at the still-water line as W_r which is given by the following equation:

$$\frac{\delta}{2W_r} \frac{H_o}{\lambda_o} = 1.51 \times 10^{-3} \left[D_o^{0.132} D_{50}^{-0.447} \left(\frac{H_o}{\lambda_o} \right)^{-0.717} \right]^{-2.38} + 0.11 \times 10^{-3} \quad (100)$$

where δ is the total depth of the D-profile (Figure 24). The variation of the ratio W_i/W_r over the D-profile determines the dimensionless form of the D-profile. Swart determined the following equation for W_i/W_r :

$$\frac{W_i}{W_r} = 0.7 \Delta_r + 1 + 3.97 \times 10^7 b D_{50}^2 \Delta_r^{1.36 \times 10^4} D_{50} \quad (101)$$

where

$$\Delta_r = \frac{h_m - \delta_{2i}}{\delta} = \begin{array}{l} \text{the dimensionless position in the} \\ \text{D-profile measured positively downward} \\ \text{from the still-water level} \end{array} \quad (102)$$

$b = 1$ for $\Delta_r > 0$, i.e., below the still-water level

$b = 0$ for $\Delta_r \leq 0$, i.e., above the still-water level

78. The transport rate $(S_y)_{it}$ (i refers to position on D-profile and t to time) was found by Swart (1976) to be given by the following equation:

$$(S_y)_{it} = (s_y)_m \frac{(s_y)_i}{(s_y)_m} \frac{W_t \delta_t X_b X_i}{\delta_{2i}} \exp(-X_b t) \quad (103)$$

where

$$(s_y)_m = \frac{D_{50}}{T} \exp \left\{ 10.7 - 28.9 \left[H_o^{0.78} \lambda_o^{0.9} D_{50}^{-1.29} \left(\frac{H_o}{h_m} \right)^{2.66} \right]^{-0.079} \right\} \quad (104)$$

$$\frac{(s_y)_i}{(s_y)_m} = \frac{4 \delta_{1i} \delta_{2i}}{\delta^2} \left[\frac{(y_2 - y_1)_{mo}}{W_{bm} + (y_2 - y_1)_{mo}} \right] \left[\frac{W_{bi} + (y_2 - y_1)_{io}}{(y_2 - y_1)_{io}} \right] \quad (105)$$

$$X_b = \left[\frac{(y_2 - y_1)_{io}}{W_{bi} + (y_2 - y_1)_{io}} \right] X_i \quad (106)$$

$$X_i = \frac{\delta(s_y)_i}{\delta_{1i} \delta_{2i}} \quad (107)$$

$$(y_2 - y_1)_{io} = W_i - (L_2 - L_1)_{io} \quad (108)$$

$$W_{bi} = \left(\frac{\delta_t}{\delta_{2i}} \right) W_t \quad (109)$$

Subscript *m* refers to middepth ($\delta_{1i} = 0.5\delta$), and subscript *o* refers to time $t = 0$. W_t is the difference in length between the transition distance for an equilibrium profile and the transition distance for an initial profile (Figure 24).

79. Although the Swart model is a two-dimensional onshore-offshore model, transport depends upon the angle at which waves attack the D-profile area. Oblique wave attack produces increased shear stress on the bed due to the presence of nearshore currents generated by the oblique wave attack. Swart found that $(s_y)_i$ increases when the three-dimensional effect of oblique wave attack is included. The increase is given by the following factor:

$$\left[1 + m_2 \left(\frac{v}{\xi_J u_o} \right)^{N_2} \right]^{4.5} \quad (110)$$

where

$$m_2 = 1.94 + 2.97 \sin \theta_b \quad (111)$$

θ_b = angle of wave incidence at breaking

$$\xi_J = C_h \left(\frac{fw}{2g} \right)^{1/2} \quad (112)$$

C_h = Chezy coefficient

fw = wave friction factor (Jonsson 1966)

u_o = wave orbital velocity at the bed

$$N_2 = 1.27 - 0.39 \sin \theta_b \quad (113)$$

The longshore current velocity v is computed using the following expression

$$v = \frac{5\pi}{16} \gamma \zeta \frac{\tan \beta}{c} (gh)^{1/2} \sin \theta \cos \theta \quad (114)$$

80. Every time the wave climate is changed, a new equilibrium profile (given by the W_i values) must be calculated. The existing profile at this particular time then becomes the initial profile used to determine the $(L_2 - L_1)_{i0}$ values at all points i . The rate of sediment transport $(S_y)_{it}$ is then determined at each point i and is modified to include the effects of oblique wave attack. This rate of transport varies with time exponentially. Thus, the profile begins initially to move toward an equilibrium profile at a fast rate, but the rate slows as the profile approaches an equilibrium profile. Actually, the time required to reach equilibrium is long compared to the time a typical wave condition exists. Thus, profiles are always moving toward equilibrium profiles but never fully reaching them.

Model testing

81. The profile response model was compared with laboratory tests of profile modification under wave attack and with prototype measurements of profile modification. Figures 25 through 28 show comparisons between beach profiles that were measured in experimental tests by Eagleson et al. (1963) and results of the profile response model. The solid lines are profiles calculated by the model, and the dashed lines are measured profiles. The only parameters varied in the numerical model calculations were those that were varied in the laboratory test (initial profiles, wave heights, wave periods, and duration of the tests). The major features of the measured profiles are reproduced in the numerical model results. The agreement between measured and calculated profiles is quite remarkable considering the great complexity of the fluid-sediment interaction process.

82. Comparisons also have been made between measured profile modification in the prototype and numerical model results. For example, a storm during the period 16-21 February 1980 at Santa Barbara, California, was documented (Gable 1981) in detail during the Nearshore Sediment Transport Study (NSTS). This was a large storm that produced approximately 40 m of shoreline erosion. Daily profile measurements were made by the NSTS in addition to complete directional spectral wave data. Figure 29 shows good agreement between measured profiles and the profile response model simulation over the 5-day period of the storm. The only inputs to the numerical model were the

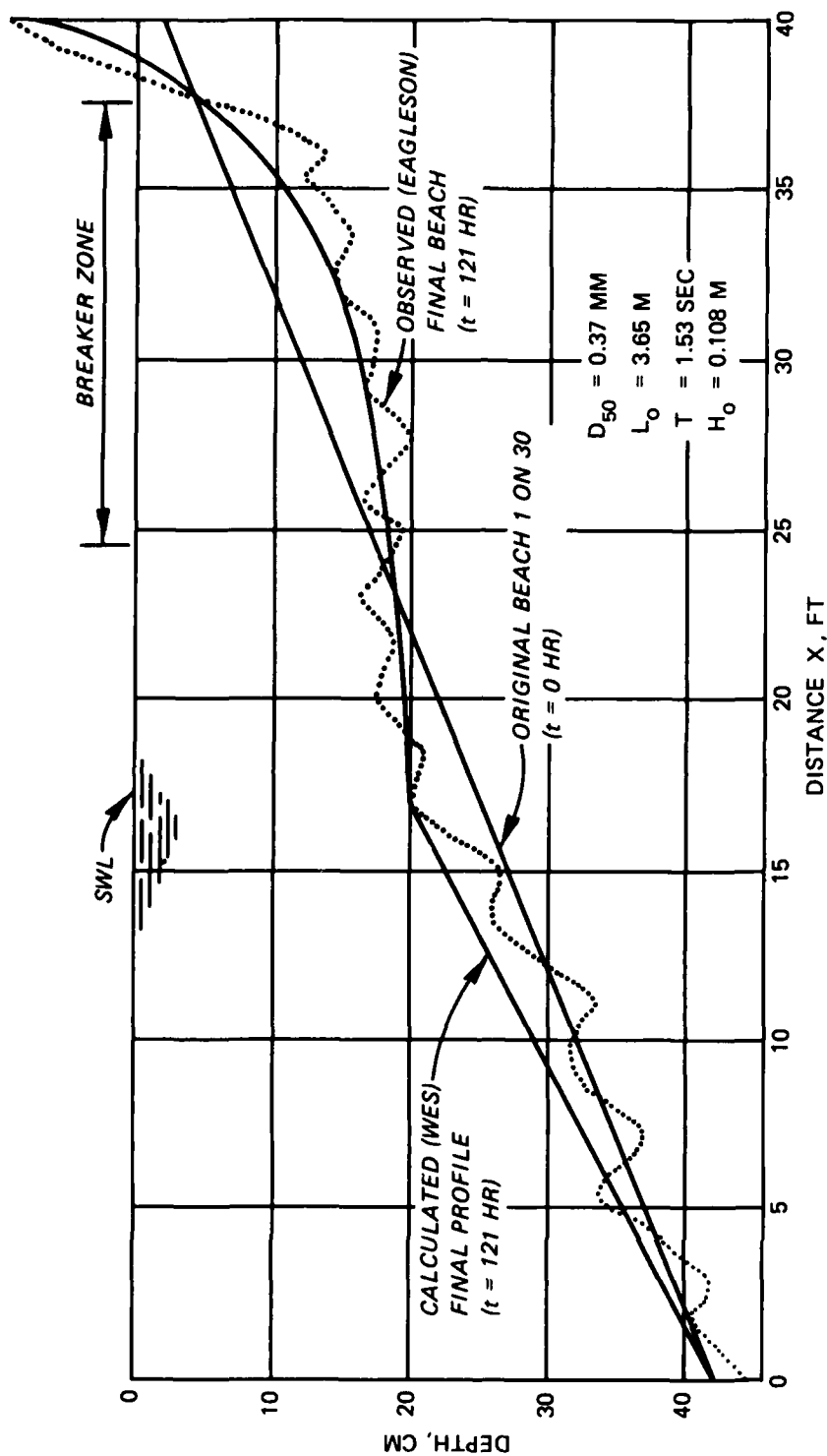


Figure 25. Comparison of experimental and calculated onshore-offshore profiles, Test 1
(Eagleson et al. 1963)

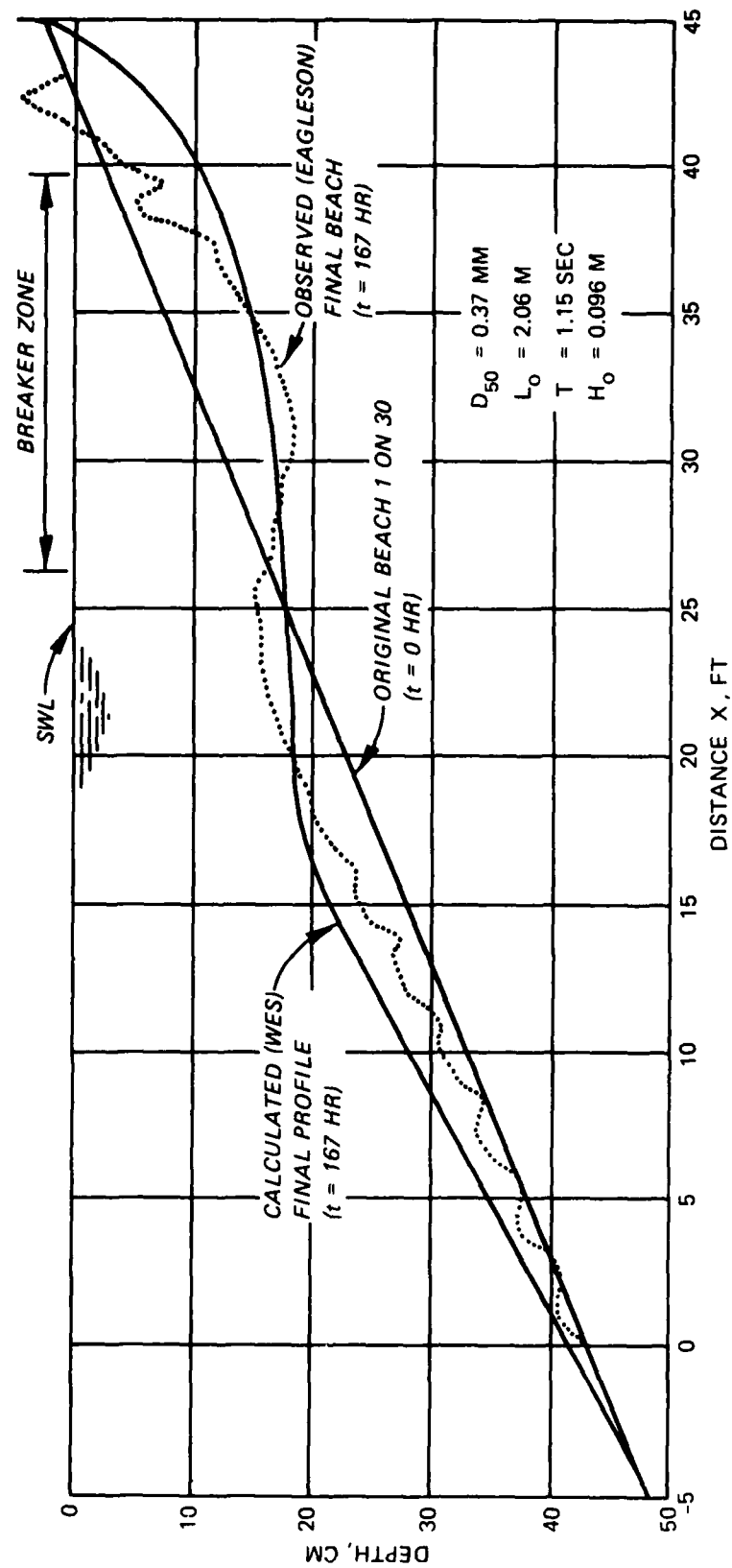


Figure 26. Comparison of experimental and calculated onshore-offshore profiles, Test 2 (Eagleson et al. 1963)

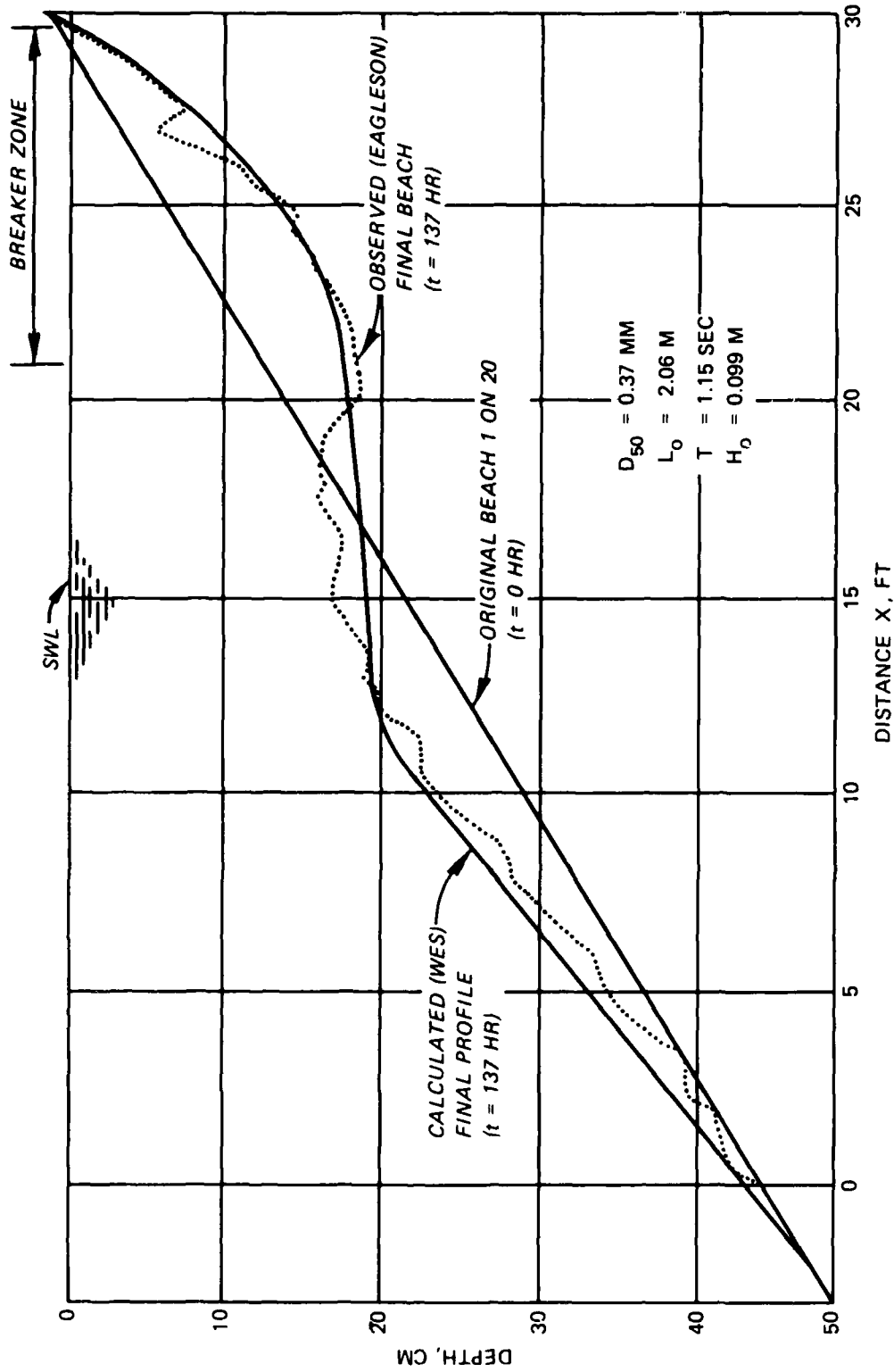


Figure 27. Comparison of experimental and calculated onshore-offshore profiles, Test 3
(Eagleson et al. 1963)

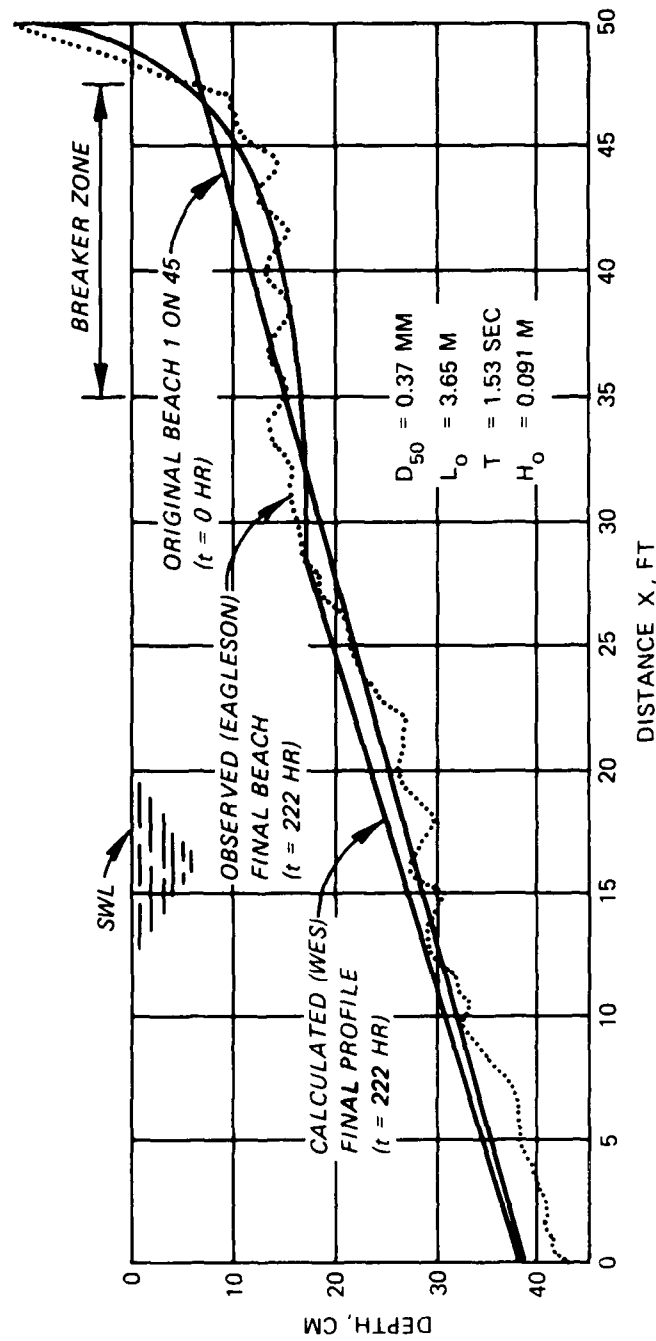


Figure 28. Comparison of experimental and calculated onshore-offshore profiles, Test 4
(Eagleson et al. 1963)

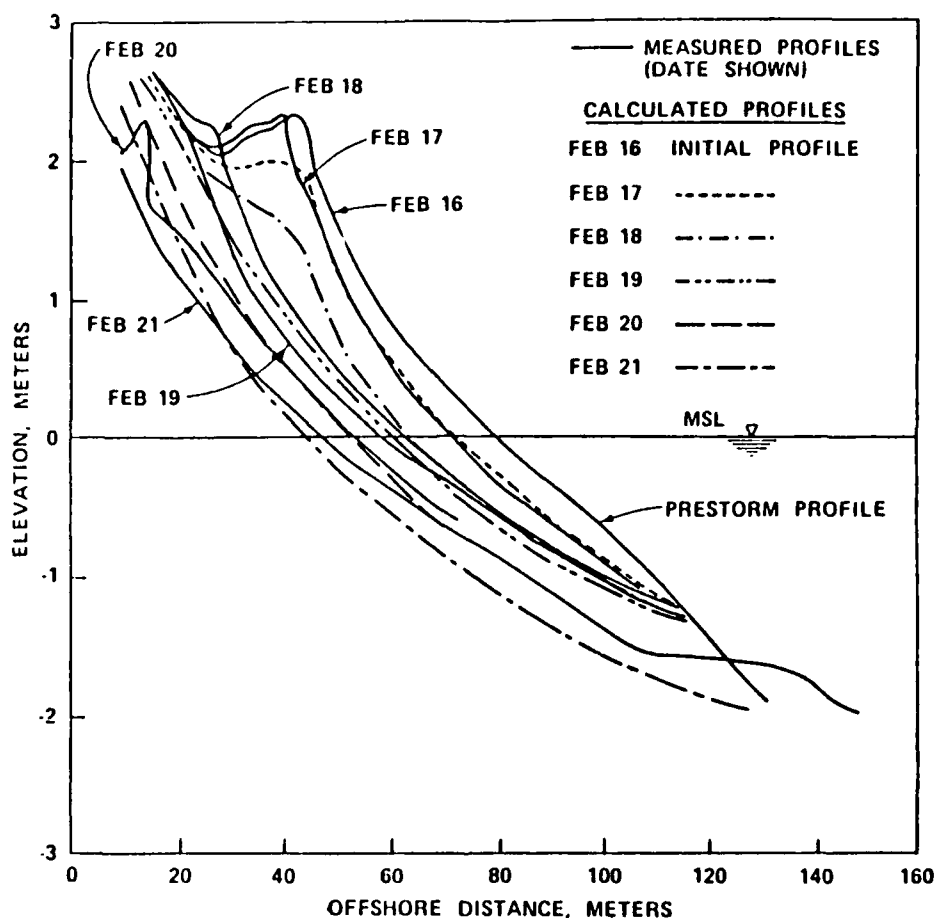


Figure 29. Comparison of calculated and measured beach profiles for Leadbetter Beach, California, 1980

initial profile (16 February 1980); the sand size; hourly values of significant wave height, period, and direction; and hourly tide levels. Tidal fluctuations played an important role in the mechanism of cross-shore transport (Swain and Houston 1984a). The sensitivity of the model to other important parameters is discussed elsewhere (Swain 1984).

83. A comparison has been made also between measured profile modification during the Currituck Sand-Bypass Study (Schwartz and Musialowski 1980) and the profile response model calculations. This study involved placement of 26,750 cu m of sediment on the coast near New River Inlet, North Carolina, using the split-hull dredge CURRITUCK. Since the dump area was relatively small, there were significant "end effects" so that the amount of sand in the

profiles was not constant. However, end effects were minimized by selecting a profile through the center of the dump. Wave characteristics were obtained during the study using Littoral Environment Observation (LEO) techniques. Figure 30 shows an initial profile measured after the dumping was completed (11 August 1976) and measured and calculated profiles at the end of the LEO measurements. The profile response model predicted that there would be little modification in the profile over this time period except for some erosion of the break point bar and filling of the adjacent trough. The measured profile confirms this numerical prediction. Figure 31 shows that the calculated and measured profiles differ at most by a few tenths of a metre in elevation. This difference is undoubtedly within the level of accuracy of the profile measurements. In addition, LEO measurements are not precise means of measuring wave conditions.

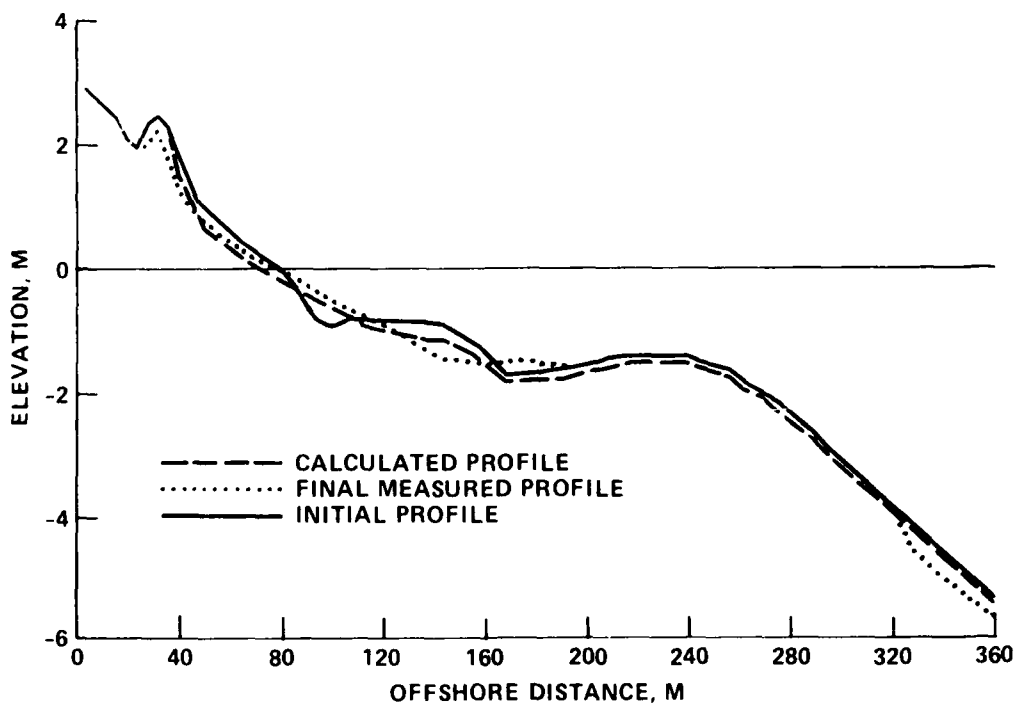


Figure 30. Comparison of calculated and measured shore-normal profiles for New River Inlet, North Carolina (dredged disposal sand movement)

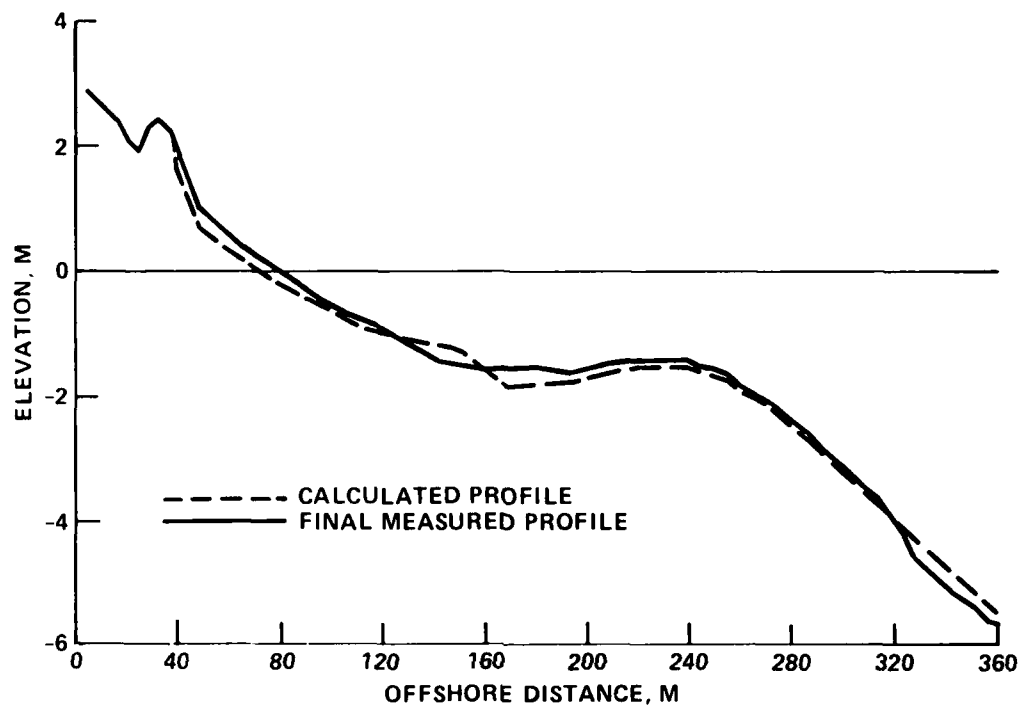


Figure 31. Comparison of calculated and measured final profiles for New River Inlet, North Carolina

PART III: APPLICATIONS

Ash Wednesday Storm

84. As a verification test of the numerical modeling system's ability to determine sediment transport near Oregon Inlet for an extreme storm event, the Ash Wednesday storm of 1962 was simulated. The storm lasted from 7 to 11 March 1962. This record northeaster caused severe beach erosion along Bodie Island and Pea Island on the north and south sides of the inlet, respectively. The erosion continued until it reached high dunes. On the northern part of Bodie Island, the land was low and flooded.

85. To run the simulation, the wave climate (significant wave height, period, and direction) in deep water was hindcast at 3-hr intervals throughout the storm using WESWIS. Simultaneously, the tidal and storm surge levels and currents during the storm were obtained using the numerical tide and surge model.

86. Since the major part of the net sediment transport during a severe storm is in the onshore-offshore direction, only the profile response model was run using the information on waves, astronomical tides, and storm surge levels. The measured shore-normal pre-storm profiles for the two islands were furnished by the National Park Service (NPS), US Department of the Interior (DOI), and were taken a year prior to the storm. The poststorm profiles were taken a few weeks after the storm and were furnished by the NPS. Thus the measured data do not represent just the erosion due to the storm. However, the erosion produced by the storm was much greater than normal yearly fluctuations. The measured profiles indicate that shoreline erosion varied from sixty to several hundred metres with higher erosion being near the inlet. Figures 32 and 33 present a comparison between measured shore-normal erosion and numerical model results. The agreement is remarkable, considering the uncertainties associated with the measured data.

Evaluation Of Nonstructural Solution

87. As an alternative to the inlet stabilization of Oregon Inlet that was authorized in the overall Manteo (Shallowbag) Bay project, DOI proposed a dredging and disposal procedure that would not require the construction of

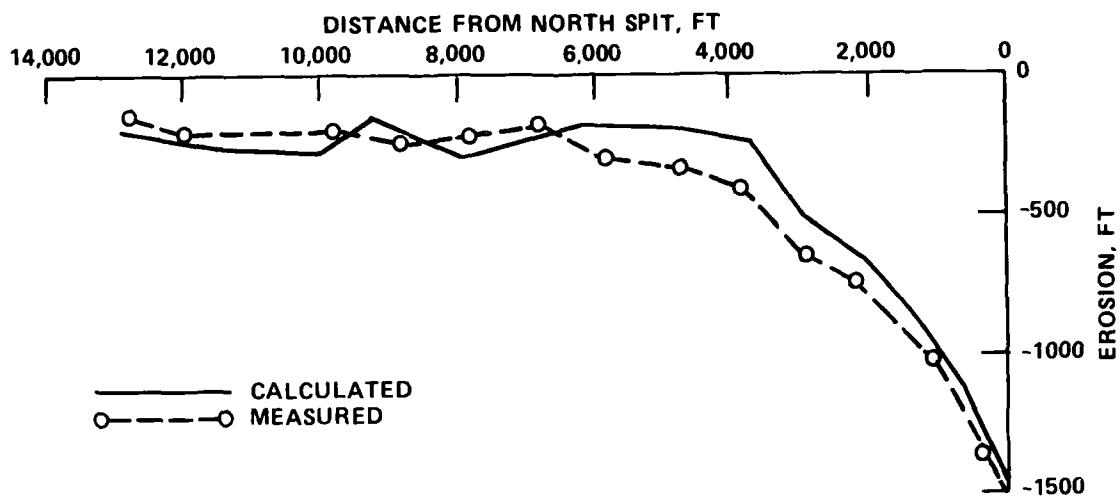


Figure 32. Comparison of calculated and measured shore-normal erosion for Bodie Island during 1962 Ash Wednesday storm

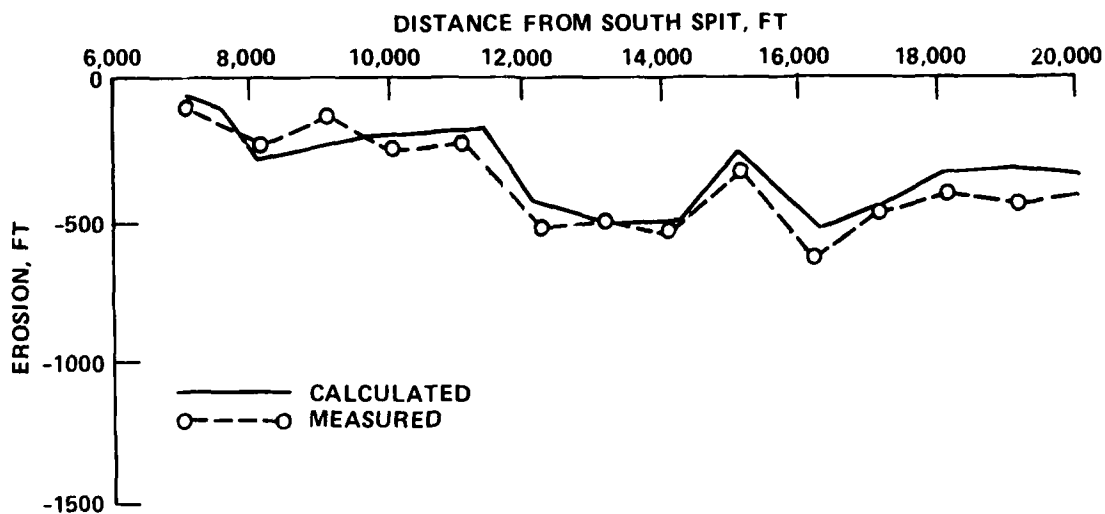


Figure 33. Comparison of calculated and measured shore-normal erosion for Pea Island during 1962 Ash Wednesday storm

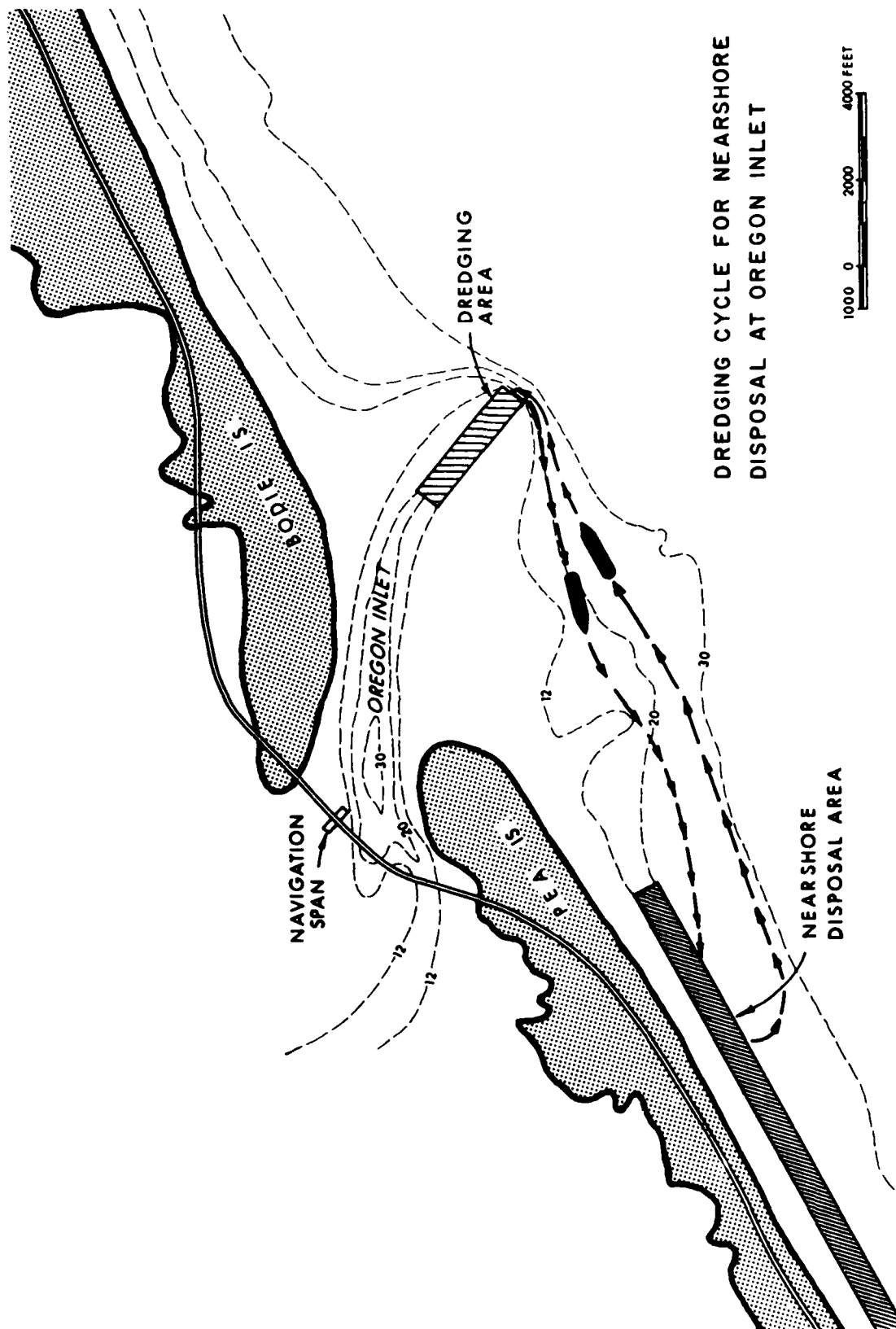
jetties at Oregon Inlet. DOI administers the Federal lands adjacent to Oregon Inlet on which the proposed jetties must be anchored.

88. The DOI plan attempted to minimize disturbance of park and refuge lands by proposing that material dredged from the inlet be placed in the near-shore zone as close to the beach as possible by small split-hull hopper dredges. This was in lieu of hydraulically transporting the dredged material from the inlet along the beach via a pipeline with disposal being accomplished in a manner similar to that in conventional beach nourishment. The DOI proposal assumed the dredged material placed in the nearshore zone would be dispersed shoreward by wave action at a rate sufficient to prevent dredging-induced beach erosion.

89. The only dredging plants that have the capability to quickly dispose dredged material in the shallow nearshore zone in the presence of waves are the CURRITUCK and ATCHAFALAYA/MERMENTAU class split-hull dredges. The split-hull design allows these dredges to dump their loads very rapidly and at the same time rise quickly to a shallow draft, thus avoiding the danger of striking the bottom. The CURRITUCK class dredge has a hopper capacity of 315 cu yd, an unloaded draft of 3 ft, and a loaded draft of 8 ft. The ATCHAFALAYA/MERMENTAU class has a hopper capacity of 1,300 cu yd, an unloaded draft of 5.7 ft, and a loaded draft of 14 ft.

90. The US Army Engineer District, Wilmington (SAW) (1983), performed a feasibility study for the plan proposed by the DOI. Material dredged from the inlet would be placed in a nearshore disposal area as shown in Figure 34. The disposal zone would begin at a point approximately 12,500 ft from the seaward end of the entrance channel. At this location, the ebb-tidal delta ceases to exist; and bottom contours are essentially parallel to the shore. Placement of material closer to the inlet than this point would cause the material to be in the ebb-tidal delta area. Material in the ebb-tidal delta typically would not be transported to adjacent beaches; thus erosion of the beaches would be accelerated. Much of the material also would move toward the inlet and quickly reenter the navigation channel. The farthest disposal point would be located approximately 65,000 ft from the seaward end of the ocean entrance channel.

91. The split-hull dredges would place material in the nearshore zone by dropping it in the pattern shown in Figure 34. Dimensions of the disposal mounds were determined by SAW based on the length and breadth of the vessel



DREDGING CYCLE FOR NEARSHORE
DISPOSAL AT OREGON INLET

Figure 34. Location of nearshore disposal area (SAW 1983)

hoppers and the loaded and unloaded drafts of each vessel. Disposal depths were -11 ft and -17 ft MLW for the CURRITUCK and ATCHAFALAYA/MERMENTAU classes, respectively (based upon a 3-ft clearance of each vessel to allow for vessel vertical motions that would occur as a result of steep shoaling waves in the nearshore area). The dredges would continue the dumping pattern until the end of the disposal area was reached. Then the pattern would begin again. If the material in the first disposal mound were sufficiently dispersed to allow the dredges to dump material once again, the second disposal mound would be located where the first mound was dumped. If not, a second row of material would be dumped immediately behind the first. This placement of mounds would continue indefinitely with attempts made to dump the material in the shallowest depth of water available (depending upon the dispersal of earlier mounds).

92. A key question about the feasibility of the DOI proposed nonstructural solution was whether the material placed in the nearshore area would be dispersed shoreward by wave action at a rate sufficient to prevent dredging-induced beach erosion. To address this question, only the profile response (onshore-offshore transport) model described in this report was used since the material to be deposited would be away from the area where tidal currents are significant and in an area where bathymetric contours are approximately straight and parallel. Changes in the rates of onshore-offshore sediment transport resulting from the disposal of the dredged material were determined from the differences between the sediment transport rates computed for a control profile (i.e. a profile without the dredged material) and the sediment transport rates computed with the dredged material in place on the profile. The calculations were accomplished using wave and tide conditions for 1975 which were determined to represent typical conditions in the Oregon Inlet area.

93. The hindcast wave conditions for 1975 were provided by the WESWIS in 10 m of water and at 3-hr intervals throughout the year. The astronomical tide for 1975 was generated using tidal constituents. SAW supplied an initial profile that was representative of the region where the dredged material would be dumped (Plate 1).

94. The profile was modified by making comparisons between the dumped-material profiles and the control profile every time-step. The width of the surf zone was determined by assuming that the breaking depth was the shoaled

wave height divided by 0.78. The dumped-material profile was compared with the control profile over this surf zone region. When the dumped-material profile had an excess of material relative to the control profile over any section of the surf zone region, the excess material was transported out of the dumped-material profile in the following manner. If the excess of material was less than the quantity of material that could be transported according to the longshore transport formula of the Coastal Engineering Research Center (CERC) given in the SPM (1984), all of the excess sediment was transported out of the profile; however, no additional sediment transport was computed as would arise from erosion of surf zone and beach line. Thus, the focus of the computations was restricted to the fate of dredge disposed material on entering the surf zone and not on erosion of the existing control profile landward of the breaker line. On the other hand, if the quantity of material entering the surf zone was greater than that which could be transported during the time-step according to the CERC formula, then the material transported out of the dumped material profile was limited to the quantity given by the CERC formula, thereby showing surf zone accretion. It was recognized that an excess of material over just a part of the surf zone would not be transported by the full power available in the surf zone. Thus, it was assumed that the material transported in the surf zone was distributed linearly over the surf zone with zero transport at the shoreline and maximum transport at the breaker line. If the excess of material was distributed over a section of the surf zone, only that power available over the section was used to transport material. Tests showed that the fate of the dumped material did not depend significantly on the assumed transport distribution across the surf zone. Virtually the same results were obtained when the transport distribution was assumed to be uniform over the surf zone. Apparently the quantity of excess material in the surf zone region during any time-step was usually less than the quantity of material that could be transported according to the CERC formula so that all of the material was transported during the time-step.

95. If there is to be shoreline stability, the dumped material must enter the nearshore region. During large storms, the surf zone can extend a very large distance seaward. Material in fairly deep water will be transported in a direction parallel to the coast during these large storms. However, if this material in deeper water does not move toward the shore, it will

not aid shoreline stability since once the storm is over this material will still be in deeper water and not in the normal littoral regime area. To include this effect in the calculations, material was transported out of the dumped material profile over a surf zone width that covered the normal near-shore transport zone. This normal nearshore transport zone was assumed to be contained within the surf zone which existed 95 percent of the time over the typical year. At Oregon Inlet, this zone extended to a water depth of approximately 2.6 m.

96. There were two depths at which the dredged material was dumped: 11 ft (3.4 m) and 17 ft (5.2 m). The shape of the dumps was trapezoidal, as provided by SAW (Plates 2 and 3). The dump in 11 ft of water was 11,000 ft long, and the dump in 17 ft was 9,800 ft long. Multiple rows of dumps were used. For example, an initial dump in 11 ft of water was made. The next month the profile was monitored to determine whether or not the material in the dump had moved out of the region sufficiently (no more than a 0.5-ft depth of material remaining) to allow another dump to be made. If a dump could not be made, a second row offshore from the first row was established. The next month the profile was monitored again. If the second row contained material that extended more than 0.5 ft above the base of the first dump location, then it was assumed that the dredge could not pass, and the material was dumped in a third row. The first row location was monitored if the dredge could pass the second row location. If the material could not be dumped in the first row location, it was dumped in the second row location again. A maximum of three rows was allowed for the dumps beginning in 17 ft of water, since it was desired not to dump material in water depths so great that the material would not be transported. Originally, the 17-ft dump was 4,900 ft long, and material was dumped once a month. However, three rows of material were not sufficient for the case (near the end of the year a dredge could not pass the third row and thus could not dump material). Therefore, the row was extended to a length of 9,800 ft, and dumps were made once every 2 months (so that the same total quantity of material was dumped). The 11-ft dumps were made once a month. Several dumping schedules were tested. First, a year was simulated with dumps beginning in January (both 11- and 17-ft depths). Then similar calculations were made for years starting in April, July, and October. Table 1 presents the percentage of dumped material transported into the active surf zone in 1 year. Somewhat more material was transported into the active

Table 1
Percentage of Dumped Material Transported
into the Active Surf Zone in 1 Year

<u>Starting Month</u>	<u>11-ft Depth, percent</u>	<u>17-ft Depth, percent</u>
January	27.6	25.5
April	27.3	25.5
July	25.8	23.4
October	28.8	24.8

surf zone for the 11-ft depths than for the 17-ft depths. The quantity of material transported into the active surf zone did not depend significantly on the initial month of placement. During the tests, there was no noticeable tendency for material to be transported to the nearshore region and remain there permanently. Material was dispersed by the littoral currents when it entered the nearshore region. This effect was noticed during the Currituck experiment also.

97. In addition to the extensive 1-year simulations, an overall 5-year simulation was made to determine the volume rate of shoreward transport of an initial 1-year dump of material over a consecutive 5-year time span. In this simulation, a 1-year supply (1.45 million cu yd) of dredged material was placed in a nearshore water depth of 17 ft. The results of this test, in terms of percent of the initial volume moving into the surf zone each year, were as follows: (a) 1st year--25.5 percent; (b) 2nd year--27.5 percent; (c) 3rd year--26.5 percent; (d) 4th year--18.8 percent; and (e) 5th year--1.4 percent. From this analysis, SAW adopted an overall annual shoreward volume rate of transport of 25 percent of a single year's volume of disposed material and evaluated the shoreline response for this rate of material transport. SAW found that this rate of onshore movement of dumped material was inadequate and would result in severe erosion occurring along the northernmost 3 miles of Pea Island. Accordingly, SAW recommended that no further consideration be given to the DOI dredging/nearshore disposal plan.

98. SAW contracted with Coastal and Offshore Engineering Research, Inc. (COER) to perform the same basic analyses described above, except an independent numerical model (Perlin and Dean 1983) developed by COER for CERC was used. In the COER model the bathymetry was represented by n-contour lines,

each of a specified depth. A requirement of the model is that depth must increase in the offshore direction. Therefore, the dumps placed in the DOI dredging plan were represented as a flat area of the bathymetry. To simulate the placement of dumped material at a depth of 11 ft, material was placed between the 7- and 11- ft contours. Material was placed also between the 11- and 14-ft contours.

99. The COER model predicted that between 15 and 35 percent of the material added between the 7- and 11-ft contours, and between 5 and 25 percent of the material added between the 11- and 14-ft contours would be dispersed into the nearshore transport system during the first year. These percentages of material that would move ashore during the first year are similar to those calculated by the model described in this report. Quantitative comparisons between the models are not possible since the COER model cannot simulate the actual bathymetry of the dumping plan.

Wave-Current Interaction

100. For cases with and without the jetties, SAW performed an ocean bar channel dredging analysis. A needed input to the analysis was the period of time that split-hull hopper dredges of the CURRITUCK and ATCHAFALAYA/MERMENTAU classes could operate in the channel under the influence of waves. Waves tend to be large near the ocean bar channel as a result of shoaling and refraction on the ocean bar and wave-current interactions. The wave climate at Oregon Inlet was known offshore at a water depth of 60 ft from WESWIS. The wave propagation model described in Part II was used to transform the wave climate at a water depth of 60 ft to the ocean bar channel (including the effects of wave-current interaction).

101. The wave propagation model was applied to Oregon Inlet using wave periods of 7, 9, and 12 sec, wave heights of 1 to 6 ft in 1-ft intervals, and the numerical grid shown in Figure 2. Tidal currents were obtained by using the tidal circulation numerical model described in Part II. Jetty spacings of 2,500, 3,500, and 5,000 ft and existing conditions without jetties were considered.

102. Figures 35-37 show some typical results produced by the wave propagation model. For example, Figure 35 shows the effect of ebb current magnitude on wave amplification for a 12-sec wave with an incident wave height of

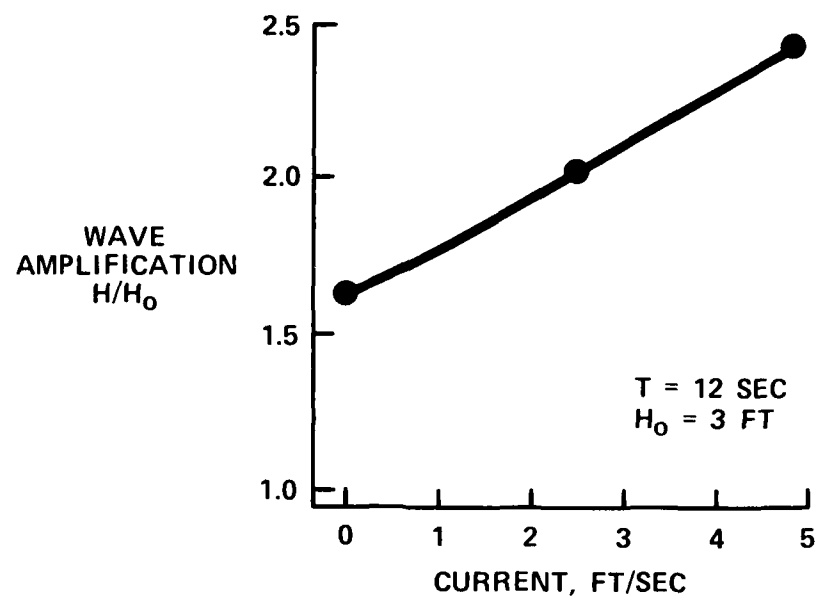


Figure 35. Effect of ebb current magnitude on wave amplification (no jetties)

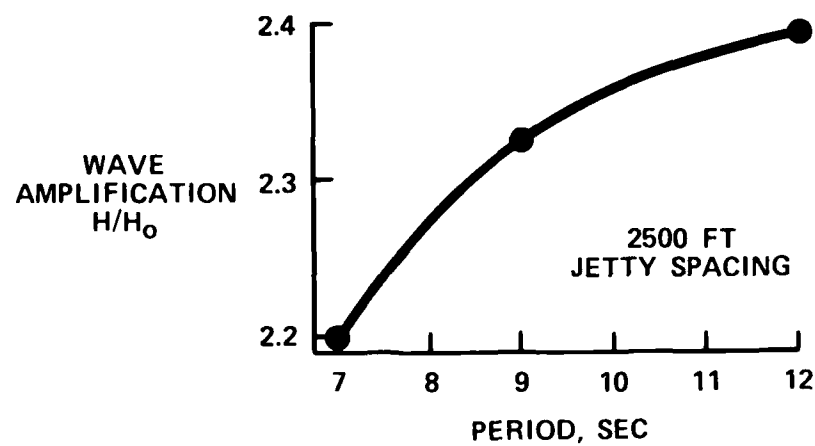


Figure 36. Dependence of wave amplification on wave period

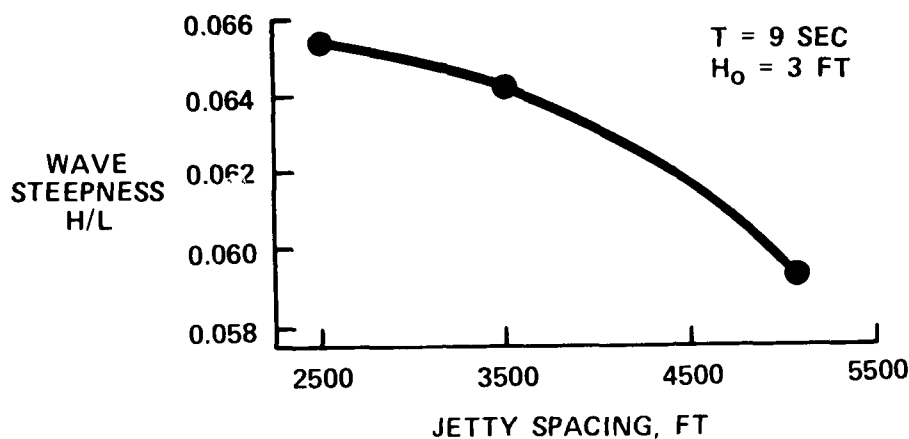


Figure 37. Effect of jetty spacing on wave steepness
($H/L = 0.057$ for no jetties)

3 ft (60-ft depth) and the condition of no jetties. The wave height increases with increasing ebb current, as expected. Figure 36 shows the dependence of wave amplification on wave period for a 2,500-ft jetty spacing. The wave amplification increases with increasing wave period, since the longer the wave period the sooner the wave interacts with the bottom and refracts and shoals. Figure 37 shows the effect of jetty spacing on wave steepness for a 9-sec wave with an incident wave height of 3 ft (60-ft depth). As expected, an increase in jetty spacing causes a decrease in the wave steepness since it reduces the ebb velocity. The decrease in wave steepness is not dramatic, however, since the jetty spacing does not change the ebb currents very much, as seen in Figures 38 and 39.

103. The wave climate at a water depth of 60 ft is in terms of significant wave height. Significant wave height is an average of the one-third highest waves of a given wave group. SAW determined that the controlling factor in vessel operation is the highest wave in a wave group. Thus SAW calculated the highest 1 percent wave for each spectrum represented by a significant wave height. Using the wave propagation model, these waves were then propagated to the ocean entrance channel.

104. The limiting wave heights for the operation of the two classes of split-hull dredge were determined by SAW based upon information from the

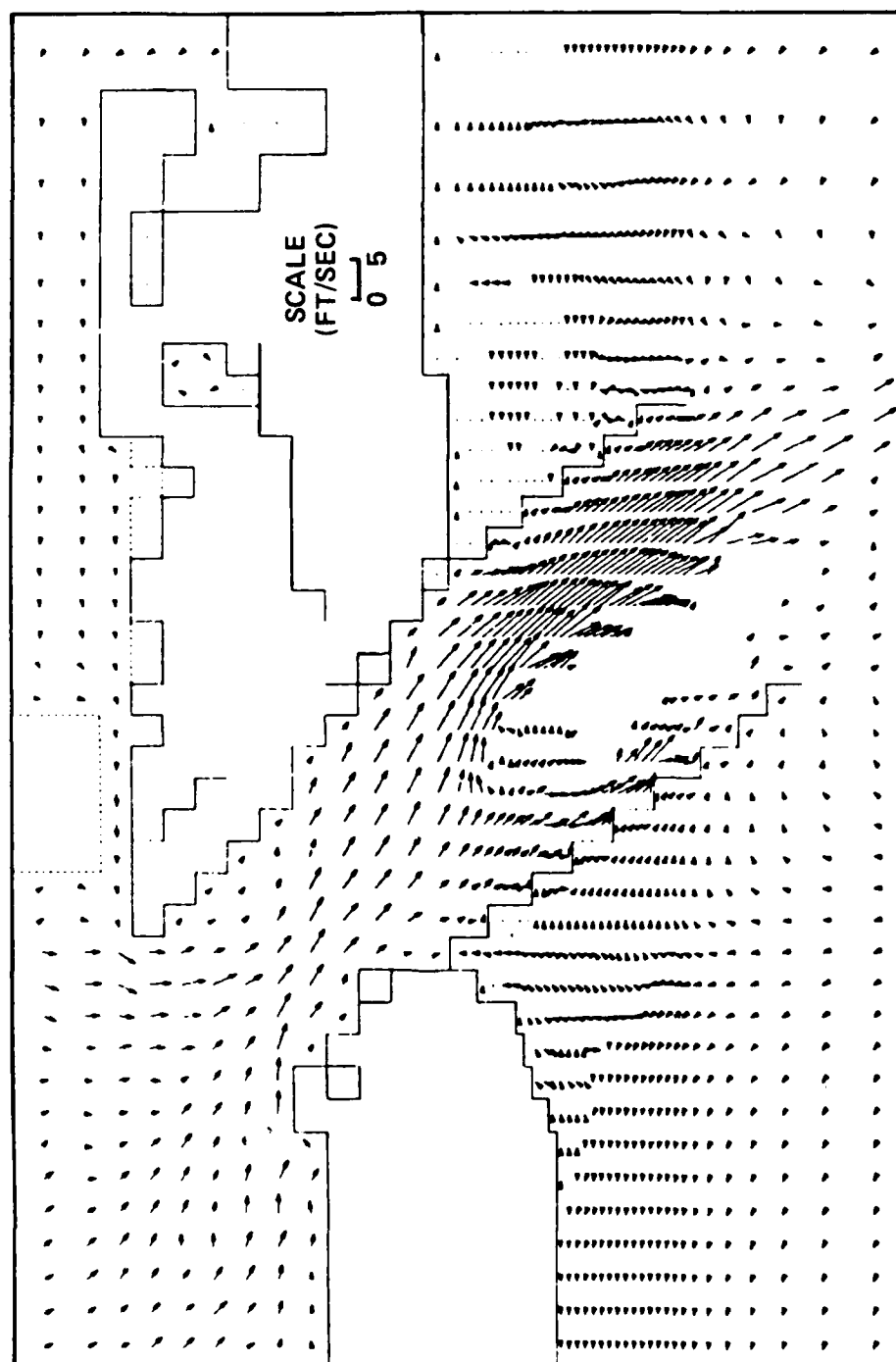


Figure 38. Ebb currents for 3,500-ft jetty spacing

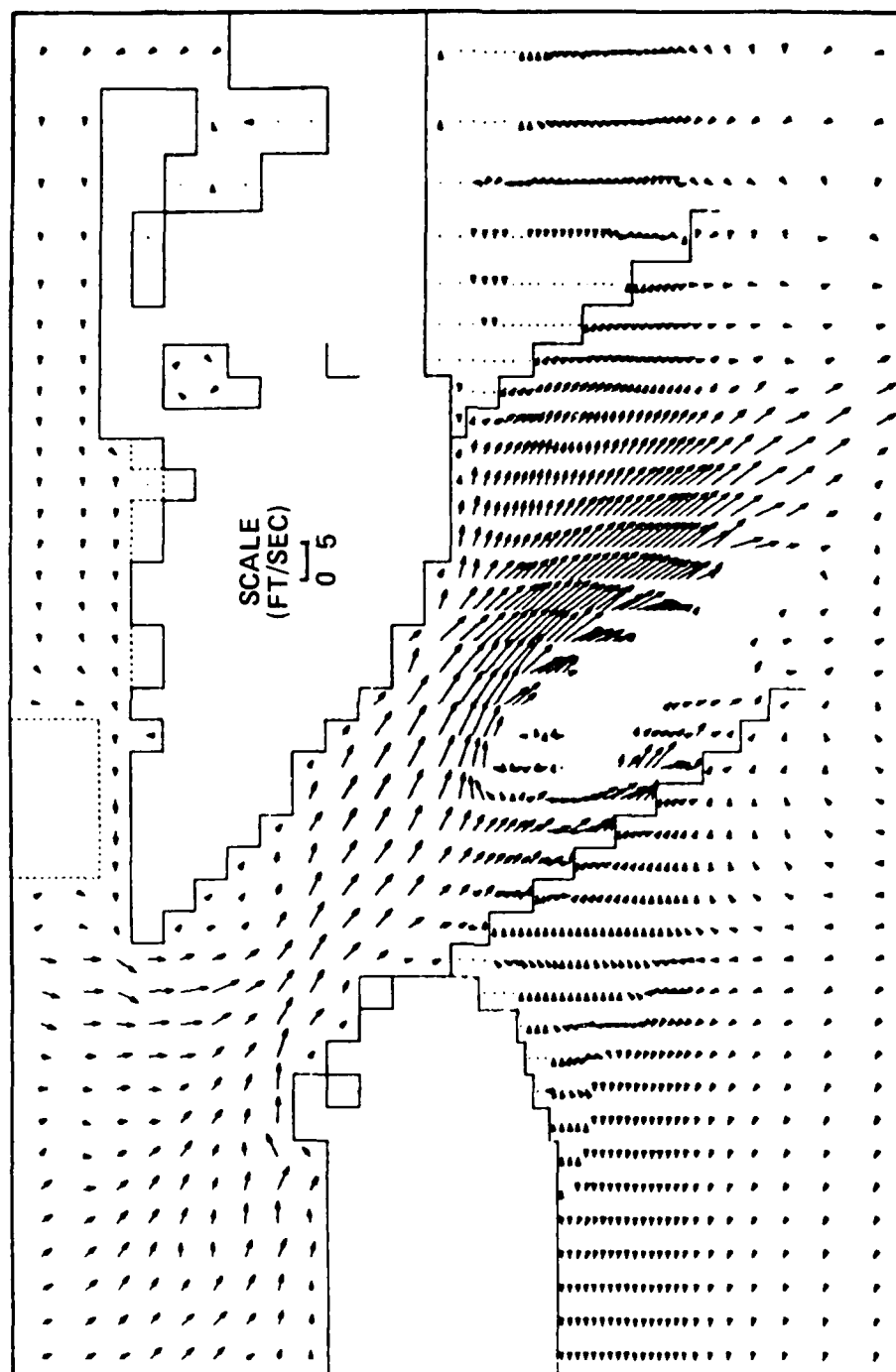


Figure 39. Ebb currents for 5,000-ft jetty spacing

operators of the vessels. In the case of the CURRITUCK, operations ceased when wave heights encountered were in the range of 6 to 8 ft, whereas the ATCHAFALAYA/MERMENTAU operated up to about 10-ft wave heights. Using the results of the wave propagation model calculations, SAW determined limiting wave heights for dredging operations in Oregon Inlet to be deepwater significant wave heights of 3.0 ft for the CURRITUCK and 4.0 ft for the ATCHAFALAYA/MERMENTAU classes.

105. The wave height limitations for the dredging operations predicted by the wave propagation model were substantiated by SAW which compared the daily logs of the dredge HYDE (which operated at Oregon Inlet during 1960-1971) to wave data recorded during most of this period. The HYDE was a seagoing trailer-suction hopper dredge with seakeeping qualities similar to those of the ATCHAFALAYA/MERMENTAU class dredge. The wave gage was located approximately 8 miles north of Oregon Inlet on a fishing pier at Nags Head. On the basis of the comparison, it was concluded that the HYDE ceased to operate when significant wave heights reached 4.0 ft at the wave gage.

Single Jetty Evaluation

106. The sediment transport model developed for transport within the surf zone and beyond was applied to Oregon Inlet for evaluating erosion and accretion in the ocean bar entrance channel and the lateral movement of the bar channel for the case in which just the south jetty was in place. This single jetty condition simulates a construction sequence in which construction of the south jetty would be completed prior to the beginning of construction of the north jetty.

107. The wave climate for an average year at a depth of 60 ft MLW near Oregon Inlet was obtained from WESWIS based on 20-year hindcast data. This information is given in the form of percent of occurrence of wave height, period, and direction combinations. For running the sediment model, the wave climate information was further consolidated into 35 combinations of wave height, period, and direction, and the percent of occurrence of each combination was determined. Table 2 shows the 35 combinations. The wave propagation model was run with the south jetty in place for these combinations, and the local wave information at each of the grid cells and the breaker line(s) was determined for each case. This information was used as

input to the wave-induced current model which computed and stored on files the steady-state wave-induced currents and setups for the single south jetty case.

108. To run the sediment transport model for an average year, the year was divided into blocks of 4-hr duration during each of which the wave climate was assumed to be constant. During the running of the sediment model, random numbers between 0 and 1.0 were generated every 4 hr of prototype time using a random number generator subroutine. Based on the value of the random number, one of the 35 combinations of wave climate listed in Table 2 was picked, and the corresponding file from the wave-induced current model was used. For example, if the value of the random number generated was between 0 and 0.2580, the first combination listed in Table 2 was selected. If the random number was between 0.2580 and 0.3725, the second combination of Table 2 was picked, and so on. In this way when the full year simulation was run, the percent of occurrence of each combination in the simulation was equal to the percent determined from WESWIS, and the wave climate for the average year was faithfully reproduced in the numerical model.

109. Tidal currents and elevations for the mean tide were obtained by applying the numerical tide and surge model to the nearshore processes grid. The tidal elevations and currents were available for this study at intervals of 10 min for one full tidal cycle. An examination of these data revealed that the tidal elevations and currents did not vary significantly during 1 hr of record. Therefore, tidal elevations were varied hourly in the sediment transport model. In addition, to be consistent with the wave-induced currents, tidal currents were varied every 4 hr in the sediment transport model. During the 1-year simulation, the results of the numerical tide model were repeated at the end of each tidal cycle.

110. For purposes of computation, the entrance channel for Oregon Inlet was defined on the basis of the maximum water depth. In addition to the cell having the maximum water depth in a given row of cells, two cells on either side were included in the channel, provided their depth exceeded 10 ft. Figure 40 shows the channel so defined. The sediment model was modified to simulate removal of 40,000 cu yd of dredged material per year from the channel.

111. The wave-induced current model provided the discharge on each cell face (longshore and cross-shore direction). The tidal velocities obtained from the numerical tide model were used to calculate the tidal discharge on

Table 2
Selected Wave Characteristics from 20-Year
Hindcast of WESWIS

Serial No.	Wave Height ft	Wave Period sec	Wav. Angle with the Shoreline deg	Percent of Occurrence	Σ Percent of Occurrence
1	0.82	8.0	45	25.80	25.80
2	2.46	7.5	45	11.45	37.25
3	4.10	7.5	45	3.50	40.75
4	5.74	7.5	45	1.15	41.90
5	7.38	7.5	45	0.50	42.40
6	9.02	7.5	45	0.20	42.60
7	10.66	8.5	45	0.05	42.65
8	0.82	7.5	75	2.70	45.35
9	2.46	7.5	75	3.45	48.80
10	4.10	12.0	75	2.05	50.85
11	5.74	12.0	75	0.80	51.65
12	7.38	7.5	75	0.35	52.00
13	9.02	7.5	75	0.35	52.35
14	10.66	8.5	75	0.15	52.50
15	12.30	9.5	75	0.05	52.55
16	0.82	7.5	105	2.85	55.40
17	2.46	7.5	105	5.30	60.70
18	4.10	8.5	105	3.55	64.25
19	5.74	8.5	105	1.85	66.10
20	7.38	7.5	105	1.20	67.30
21	9.02	7.5	105	0.75	68.05
22	10.66	8.5	105	0.45	68.50
23	12.30	9.5	105	0.20	68.70
24	13.94	10.5	105	0.10	68.80
25	15.58	10.5	105	0.05	68.85
26	18.04	12.0	105	0.05	68.90
27	0.82	7.5	135	11.05	79.95
28	2.46	7.5	135	8.50	88.45
29	4.10	7.5	135	4.90	93.35
30	5.74	7.5	135	2.95	96.30
31	7.38	7.5	135	2.20	98.50
32	9.02	7.5	135	0.95	99.45
33	10.66	9.5	135	0.30	99.75
34	12.30	9.5	135	0.10	99.85
35	13.94	10.5	135	0.05	99.90

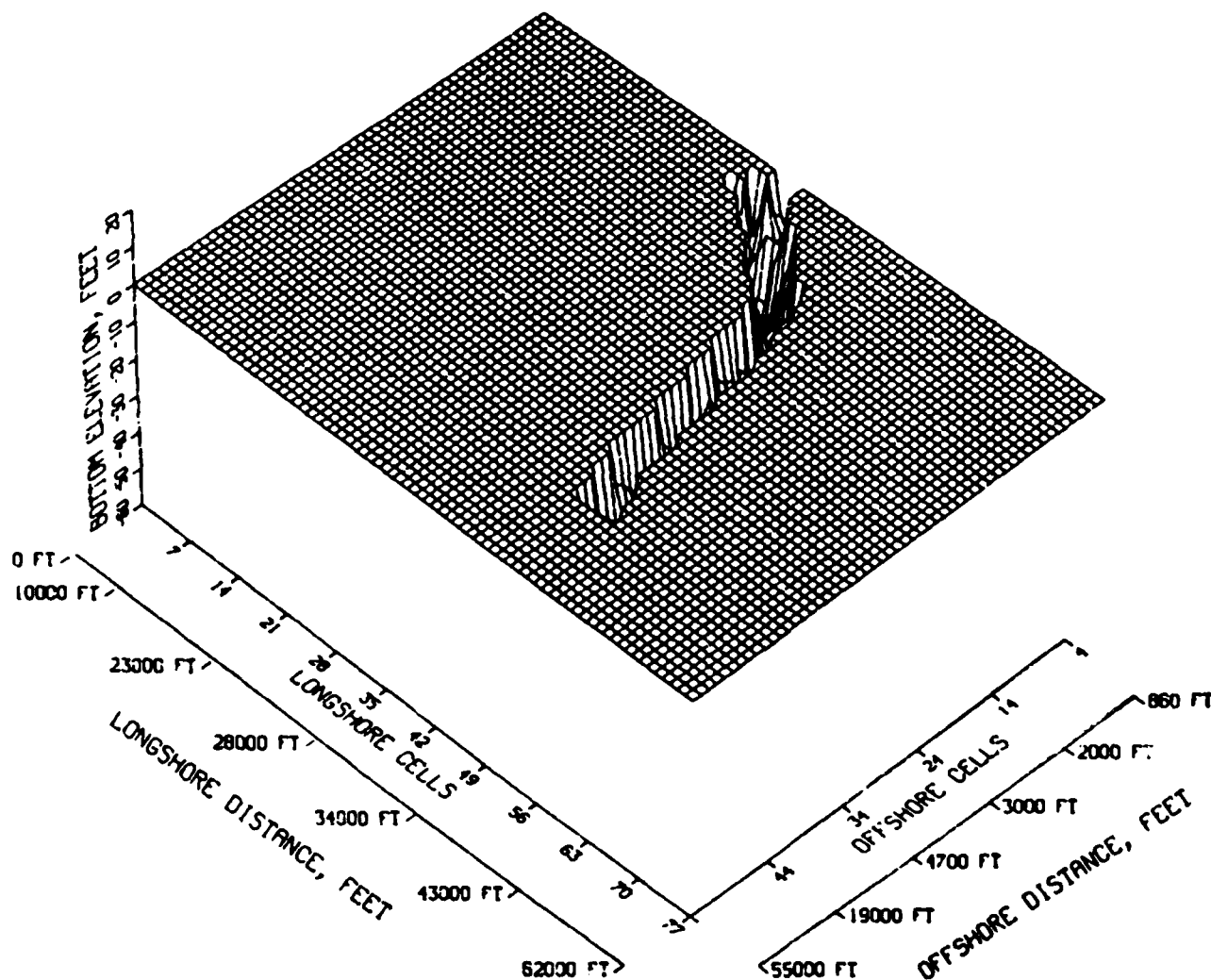


Figure 40. Location of entrance channel

each cell face. The sum of the two discharges (wave-induced and tidal) constituted the total water discharge.

112. The dimensionless sediment concentration for the surf zone and beyond the surf zone was calculated from equations described earlier. In the numerical model, the sediment concentration was defined at the center of a cell. The water discharge was then multiplied with the sediment concentration to obtain sediment discharge on a cell face.

113. For a given tidal and wave-induced flow condition the continuity equation (Equation 97) was solved to determine the change in the bed elevation Δh of a cell. A time-step Δt of 1 hr was used for the sediment transport model. A sensitivity analysis on time-step ($\Delta t = 10, 30, \text{ and } 60 \text{ min}$) showed

that the desired accuracy could be achieved with a 1-hr time-step. A porosity p of 40 percent was used for sand.

114. The new water depth d_{new} of a cell was calculated by adding Δh to water depth d_m of the previous time-step. If Δh was negative, the cell eroded; and if positive, the cell accreted. The next time-step began with the calculation of water depth d_m in each cell of the entire shore processes grid. This was accomplished by adding the change in tidal elevation to d_{new} . d_m was then used to calculate the dimensionless sediment concentrations beyond the surf zone using the modified Ackers and White formulation. The surf zone concentrations were kept constant because the wave field was constant. This procedure was followed for three time-steps.

115. Every fourth time-step a new set of records consisting of wave fields, wave-induced currents and setups, and tidal currents and elevations was read in accordance with the file sequence presented earlier. The techniques described in the previous paragraph were repeated between every fourth time-step.

116. The bathymetric changes in the Oregon Inlet area were calculated for 1 year. The location of the Oregon Inlet channel (defined earlier) at the beginning and end of each month was saved for analysis. In addition, the water depths over the entire shore processes grid were saved each month to determine monthly erosion and deposition.

117. The volume of sediment trapped in the Oregon Inlet channel was computed each month for a year. Table 3 shows the monthly deposition. A total of 1,055,990 cu yd of materials was trapped in the Oregon Inlet channel during the 12-month period. A calculation using the CERC formula given in the SPM (1984) revealed that 1,080,000 cu yd of materials could be transported during a year under an average wave condition applicable to Oregon Inlet.

118. Table 4 shows that erosion occurred between the south jetty and the channel boundary on the south side. A total of 660,000 cu yd of materials was eroded during the year. The material was either deposited in the channel or transported offshore by tidal and wave-induced currents.

119. Contour plots were made at intervals of 3 months to show erosion and accretion in the Oregon Inlet channel. Plates 4-8 show contours of erosion and accretion (in feet) at the end of the 1st, 3rd, 6th, 9th, and 12th months, respectively. Plates 9-13 present zones of erosion and accretion in the channel at the end of the 1st, 3rd, 6th, 9th and 12th months, respectively.

Table 3
Volume of Materials Trapped in the
Oregon Inlet Channel

<u>Month</u>	<u>Volume cu yd</u>
1	78,055
2	100,833
3	87,500
4	81,667
5	92,778
6	84,166
7	86,243
8	89,360
9	83,068
10	90,165
11	87,483
12	94,672
Total	1,055,990

Table 4
Volume of Materials Eroded between the South Jetty
and the South Channel Boundary

<u>Month</u>	<u>Volume Eroded cu yd</u>
1	53,333
2	50,833
3	51,944
4	55,000
5	55,833
6	51,667
7	57,248
8	56,556
9	60,373
10	56,845
11	59,778
12	50,590
Total	660,000

120. Flow cross sections taken at various locations along the Oregon Inlet channel (Plate 13) at the beginning and the end of the 1-year numerical simulation showed (Figure 41) that the part of the Oregon Inlet channel sheltered by the south jetty could move on the average about 150 ft per year toward the south jetty (for Figure 41, mean sea level (MSL) is considered to be a datum 1.0 ft above MLW).

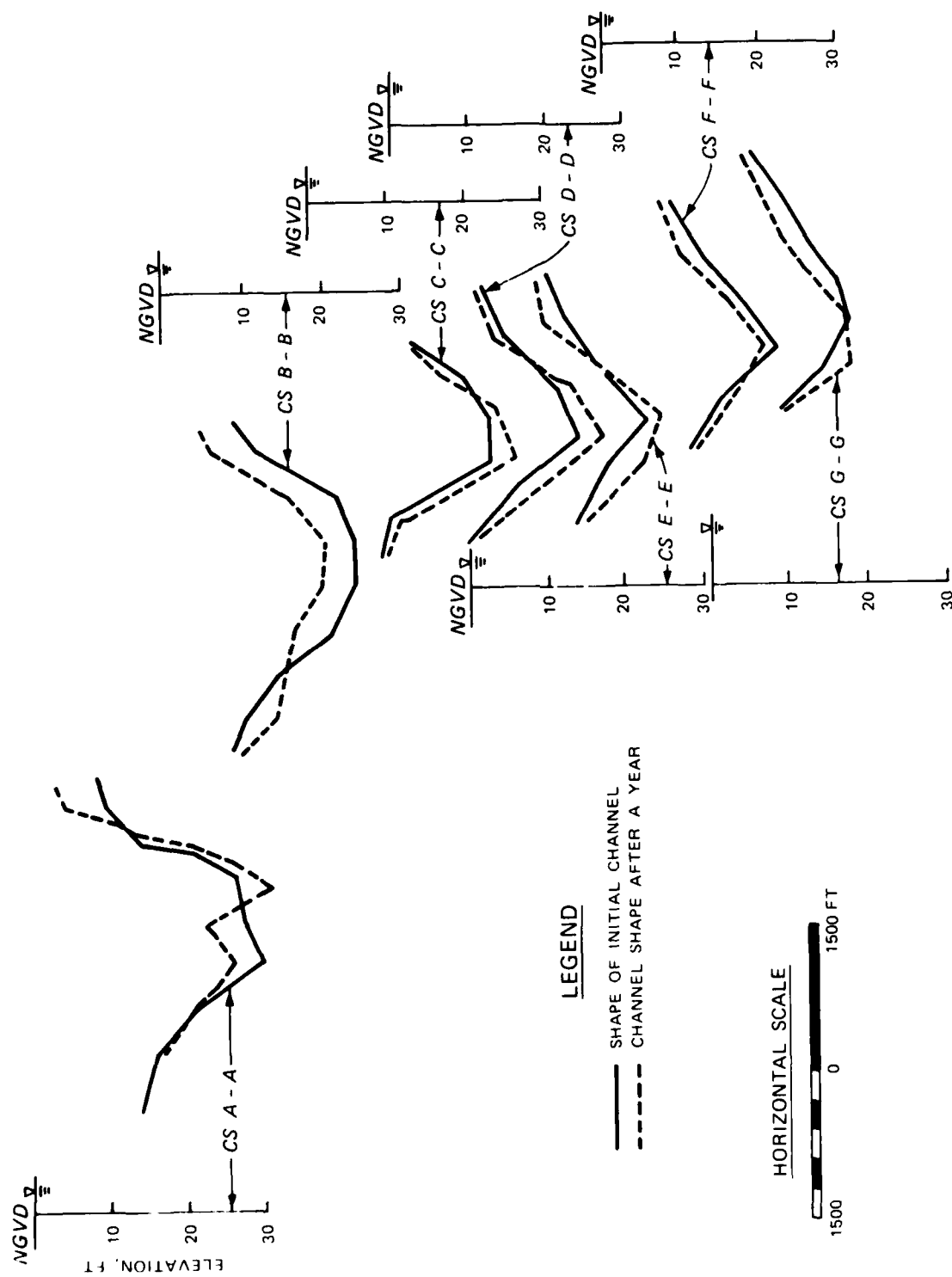


Figure 41. Flow cross sections at beginning and end of 1-year simulation

PART IV: SUMMARY AND CONCLUSIONS

121. A system of numerical models was developed to simulate coastal and inlet processes near Oregon Inlet, North Carolina. The system included models for wave propagation, wave-induced currents and setup, sediment transport within and beyond the surf zone, and profile response (onshore-offshore transport). Results from a separate study on numerical simulation of tides and storm surge for Oregon Inlet were utilized in the present investigation.

122. The emphasis in development of the models was on computational efficiency and the ability to handle complex bathymetries and large numerical grids encountered in practical engineering problems.

123. The models of the system were tested individually and validated against available analytical solutions as well as laboratory and field data. All of these tests and comparisons were successful.

124. The computational costs for the models of the system were relatively modest so that long-term simulations could be performed economically with the system.

125. As a test for an extreme event, the Ash Wednesday storm of March 1962 was simulated with the profile response model. The calculated erosion amounts of the shore-normal profiles for Bodie Island and Pea Island (on either side of Oregon Inlet) were compared with measured values. There was good agreement, especially considering the uncertainty of the measurements.

126. As an alternative to the stabilization of the Oregon Inlet entrance channel by construction of two jetties, a nonstructural solution proposed by DOI was evaluated using the profile response model. The DOI solution involved disposing the dredged material from the inlet channel in the nearshore region with the idea that the material would be dispersed shoreward by wave action at a rate sufficient to prevent dredging-induced beach erosion. On the basis of a feasibility study conducted by SAW, two disposal schemes involving placement of dredged material in depths of 11 and 17 ft were simulated using wave conditions for a typical year. Various scenarios were considered, and simulations were performed for 1- and 5-year durations. The results of these tests indicated that on the average only 25 percent of the material disposed in the nearshore migrated toward the shore in a year. This was not sufficient to prevent dredging-induced beach erosion. An independent analysis of the

disposal plan carried out by COER for SAW, using an n-line model, produced similar results.

127. In order to perform an ocean bar channel dredging analysis, SAW needed to know the period of time that dredges of the CURRITUCK and ATCHAFALAYA/MERMENTAU classes could operate in the entrance channel under the influence of waves. To study this problem, the wave propagation model was run, allowing for wave-current interactions. The tidal currents were calculated by the numerical tide model. The effects of jetty spacing on wave height and steepness were studied for a variety of typical wave conditions. Using these results, SAW determined the limiting wave heights for dredging operations in Oregon Inlet to be deepwater significant heights of 3.0 ft for the CURRITUCK and 4.0 ft for the ATCHAFALAYA/MERMENTAU classes. This was confirmed by SAW on review of the daily logs of the dredge HYDE which operated at Oregon Inlet.

128. The modeling system was used to study the erosion and accretion in the entrance channel, as well as the lateral movement of the channel in the presence of the south jetty alone, to simulate a construction sequence in which the south jetty was built before the north jetty. For this purpose, an average year's wave climate obtained from WESWIS was modeled. The wave propagation, wave-induced current, and longshore sediment transport models were run in succession. Also, information on tidal currents and elevations for the mean tide condition obtained from the numerical tide model were used. The sediment transport model simulated an average year, using a time-step of 1 hr. Computer plots showing contours and zones of erosion and accretion were made at intervals of 3 months.

129. The results of the 1-year simulation showed that a total of 1,055,990 cu yd of materials was trapped in the entrance channel during the 12-month period, whereas 660,000 cu yd of materials were eroded between the southern boundary of the channel and the south jetty.

130. On the basis of flow cross sections taken at various locations along the channel at the beginning and end of the numerical simulation, it was determined that the entrance channel could move on the average about 150 ft/yr toward the south jetty.

REFERENCES

- Ackers, P., and White, W. R. 1973. "Sediment Transport: New Approach and Analysis," Journal of the Hydraulics Division, American Society of Civil Engineers, Vol 99, No. HY11, pp 2041-2060.
- Bagnold, R. A. 1963. "Mechanics of Marine Sedimentation," The Sea, M. N. Hill, ed., Interscience Publishers, Wiley, New York, Vol 3, pp 507-528.
- Bijker, E. W. 1967. "Some Considerations About Scales for Coastal Models with Movable Bed," Delft Hydraulics Laboratory, Publication 50, Delft, The Netherlands.
- Birkemeier, W. A., and Dalrymple, R. A. 1975. "Nearshore Water Circulation Induced by Wind and Waves," Proceedings, Modeling 75 Conference, American Society of Civil Engineers, Vol II, pp 1062-1081.
- Bowen, A. J. 1969. "The Generation of Longshore Currents on a Plane Beach," Journal of Marine Research, Vol 27, pp 206-215.
- Bowen, A. J., et al. 1968. "Wave 'Setdown' and Setup," Journal of Geophysical Research, Vol 73, No. 8, pp 2569-2577.
- Butler, H. L. 1980. "Evolution of a Numerical Model for Simulating Long Period Wave Behavior in Ocean-Estuarine Systems," Estuarine and Wetlands Processes with Emphasis on Modeling, Marine Science Series, Vol 11, Plenum, New York.
- Dally, W. R. 1980. "A Numerical Model for Beach Profile Evolution," Master's thesis, University of Delaware, Newark, Del.
- Eagleson, P. S., et al. 1963. "Equilibrium Characteristics of Sand Beaches," Journal of the Hydraulics Division, American Society of Civil Engineers, Vol 89, No. HY1, pp 35-58.
- Ebersole, B. A. 1980. "A Numerical Model for Nearshore Circulation Including Convective Accelerations and Lateral Mixing," Master's thesis, University of Delaware, Newark, Del.
- Ebersole, B. A., and Dalrymple, R. A. 1980. "Numerical Modeling of Nearshore Circulation," Proceedings, Seventeenth Coastal Engineering Conference, American Society of Civil Engineers, Sydney, Australia, pp 2710-2725.
- Gable, C. G. 1981. "Report on Data from the Nearshore Sediment Transport Study Experiment at Leadbetter Beach, Santa Barbara, Calif., January-February 1980," IMR Ref No. 80-5, Scripps Institution of Oceanography, La Jolla, Calif.
- Galvin, C. 1983. "Sea Level Rise and Shoreline Recession," Proceedings, Third Symposium on Coastal and Ocean Management, San Diego, Calif., pp 2684-2776.
- Jonsson, I. G. 1966. "Wave Boundary Layers and Friction Factors," Proceedings, Tenth Coastal Engineering Conference, American Society of Civil Engineers, Tokyo, Japan, pp 127-148.
- Jonsson, I. G., et al. 1974. "Computation of Longshore Currents," Proceedings, Fourteenth Coastal Engineering Conference, American Society of Civil Engineers, Copenhagen, Denmark, pp 699-714.

- Komar, P. D. 1974. "Longshore Currents and Sand Transport on Beaches," Proceedings, Civil Engineering in the Oceans/III, American Society of Civil Engineers, Vol 1, pp 333-354.
- Komar, P. D. 1978. "Relative Quantities of Suspension Versus Bedload Transport on Beaches," Journal of Sedimentary Petrology, Vol 48, No. 3, pp 921-932.
- Leenknecht, D. A., Earickson, J. A., and Butler, H. L. 1984. "Numerical Simulation of Oregon Inlet Control Structures' Effects on Storm and Tide Elevations in Pamlico Sound," Technical Report CERC-84-2, US Army Engineer Waterways Experiment Station, Vicksburg, Miss.
- Liu, P. L-F., and Lennon, G. P. 1978. "Finite Element Modeling of Nearshore Currents," Journal of the Waterway, Port, Coastal and Ocean Division, American Society of Civil Engineers, Vol 104, No WW2, pp 175-189.
- Longuet-Higgins, M. S. 1970. "Longshore Currents Generated by Obliquely Incident Sea Waves, 1 and 2," Journal of Geophysical Research, Vol 75, No. 33, pp 6778-6789 and pp 6790-6801.
- Longuet-Higgins, M. S., and Stewart, R. W. 1964. "Radiation Stresses in Water Waves; a Physical Discussion with Applications," Deep-Sea Research, Vol 11, pp 529-562.
- Noda, E. K. 1974. "Wave-Induced Nearshore Circulation," Journal of Geophysical Research, Vol 79, No. 27, pp 4097-4106.
- Noda, E. K., et al. 1974. "Nearshore Circulations under Sea Breeze Conditions and Wave-Current Interactions in the Surf Zone," Tetra Tech Report TC-149-4, Tetra Tech, Inc., Pasadena, Calif.
- Perlin, M., and Dean, R. G. 1983. "A Numerical Model to Simulate Sediment Transport in the Vicinity of Coastal Structures," CERC Miscellaneous Report 83-10, US Army Engineer Waterways Experiment Station, Vicksburg, Miss.
- Phillips, O. M. 1969. The Dynamics of the Upper Ocean, Cambridge University Press, Cambridge.
- Schwartz, R. K., and Musialowski, F. R. 1980. "Transport of Dredged Sediment Placed in the Nearshore Zone - Currituck Sand-Bypass Study (Phase I)," CERC Technical Paper 80-1, US Army Engineer Waterways Experiment Station, Vicksburg, Miss.
- Shore Protection Manual. 1984. 4th ed., 2 vols, US Army Engineer Waterways Experiment Station, Coastal Engineering Research Center, US Government Printing Office, Washington, DC.
- Sunamura, T. 1980. "A Laboratory Study of Offshore Transport of Sediment and a Model for Eroding Beaches," Proceedings, Seventeenth Coastal Engineering Conference, American Society of Civil Engineers, Sydney, Australia, pp 1051-1100.
- Swain, A. 1984. "Additional Results of a Numerical Model for Beach Profile Development," Proceedings, National Engineering Conference, Canadian Society for Civil Engineering, Halifax, Canada, pp 651-663.
- Swain A., and Houston, J. R. 1983. "A Numerical Model for Beach Profile Development," Proceedings, 6th Canadian Hydrotechnical Conference, Canadian Society for Civil Engineering, Ottawa, Canada, Vol 2, pp 777-785.

AD-A162 419

COASTAL AND INLET PROCESSES NUMERICAL MODELING SYSTEM
FOR OREGON INLET NORTH CAROLINA(U) COASTAL ENGINEERING
RESEARCH CENTER VICKSBURG MS S R VEMULAKONDA ET AL

2/2

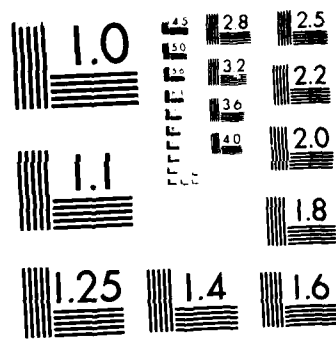
UNCLASSIFIED

SEP 85 CERC-RR-85-6

F/G 8/3

NL

END



MICROCOPY RESOLUTION TEST CHART
NATIONAL BUREAU OF STANDARDS-1963-A

- Swain, A., and Houston, J. R. 1984a. Discussion on "The Nearshore Sediment Transport Study," by R. J. Seymour, Journal of Waterway, Port, Coastal and Ocean Engineering, American Society of Civil Engineers, Vol 110, No 1, pp 130-132.
- Swain, A., and Houston, J. R. 1984b. "Onshore-Offshore Sediment Transport Numerical Model," Proceedings, Nineteenth Coastal Engineering Conference, American Society of Civil Engineers, Houston, Tex., pp 1245-1251.
- Swart, D. H. 1974a. "Offshore Sediment Transport and Equilibrium Beach Profiles," Delft Hydraulics Laboratory, Publication No. 131, Delft, The Netherlands.
- Swart, D. H. 1974b. "A Schematization of Onshore-Offshore Transport," Proceedings, Fourteenth Coastal Engineering Conference, American Society of Civil Engineers, Copenhagen, Denmark, pp 884-900.
- Swart, D. H. 1976. "Predictive Equations Regarding Coastal Transports," Proceedings, Fifteenth Coastal Engineering Conference, American Society of Civil Engineers, Honolulu, Hawaii, pp 1113-1132.
- Swart, D. H., and Fleming, C. A. 1980. "Longshore Water and Sediment Movement," Proceedings, Seventeenth Coastal Engineering Conference, American Society of Civil Engineers, Sydney, Australia, pp 1275-1294.
- Thornton, E. B. 1970. "Variation of Longshore Current Across the Surf Zone," Proceedings, Twelfth Coastal Engineering Conference, American Society of Civil Engineers, Washington, DC, pp 291-308.
- Thornton, E. B. 1972. "Distribution of Sediment Transport Across the Surf Zone," Proceedings, Thirteenth Coastal Engineering Conference, American Society of Civil Engineers, Vancouver, Canada, pp 1049-1068.
- Van de Graaff, J., and Van Overeem, J. 1979. "Evaluation of Sediment Transport Formulae in Coastal Engineering Practice," Coastal Engineering, Vol 3, pp 1-32.
- Wang, H. 1981. "Beach Profile Modeling," Proceedings of the Conference on Physical Modeling, University of Delaware, Newark, Del.
- Wanstrath, J. J. 1977. "Nearshore Numerical Storm Surge and Tidal Simulation," Technical Report H-77-17, US Army Engineer Waterways Experiment Station, Vicksburg, Miss.
- Willis, D. H. 1978. "Sediment Load Under Waves and Currents," Proceedings, Sixteenth Coastal Engineering Conference, American Society of Civil Engineers, Hamburg, West Germany, pp 1626-1637.
- US Army Engineer District, Wilmington. 1983. "Feasibility Study: Dredging/ Nearshore Disposal Plan, Oregon Inlet, N. C.," Wilmington, N. C.
- Yang, W. 1981. "Surf Zone Properties and On/Offshore Sediment Transport," Ph. D dissertation, University of Delaware, Newark, Del.

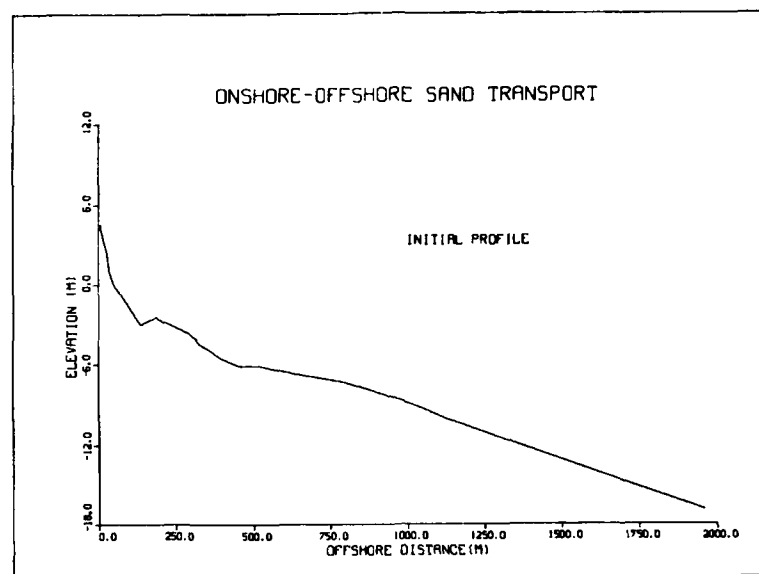


PLATE 1

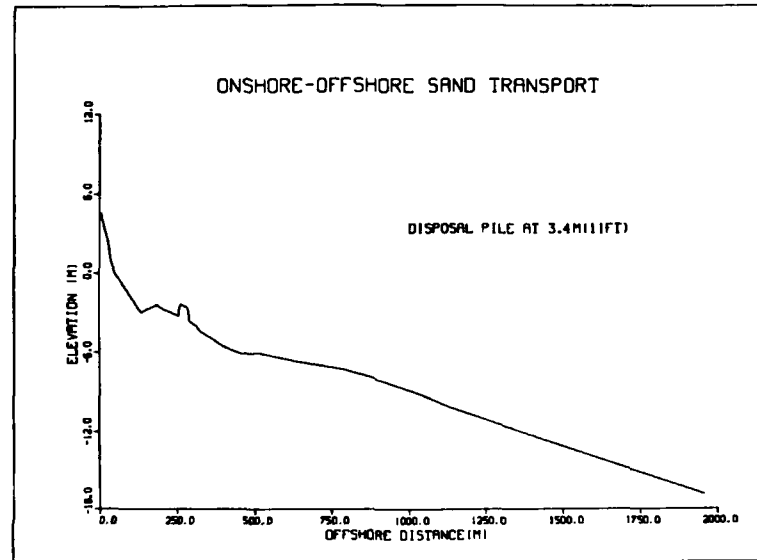


PLATE 2

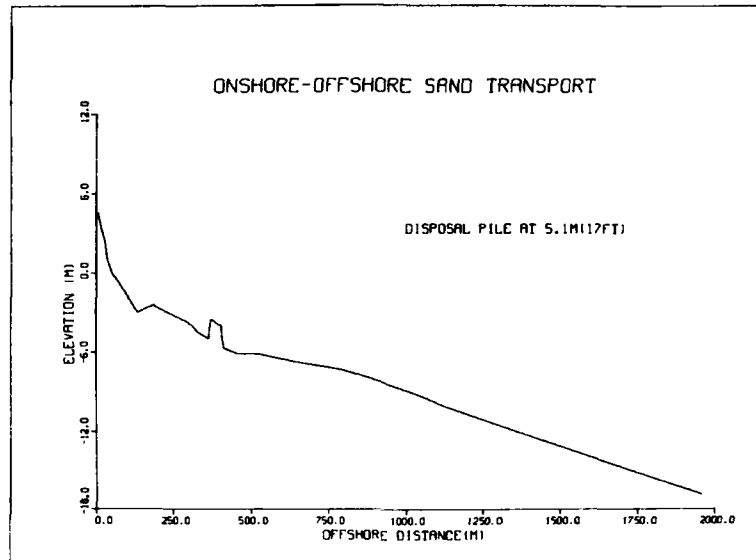
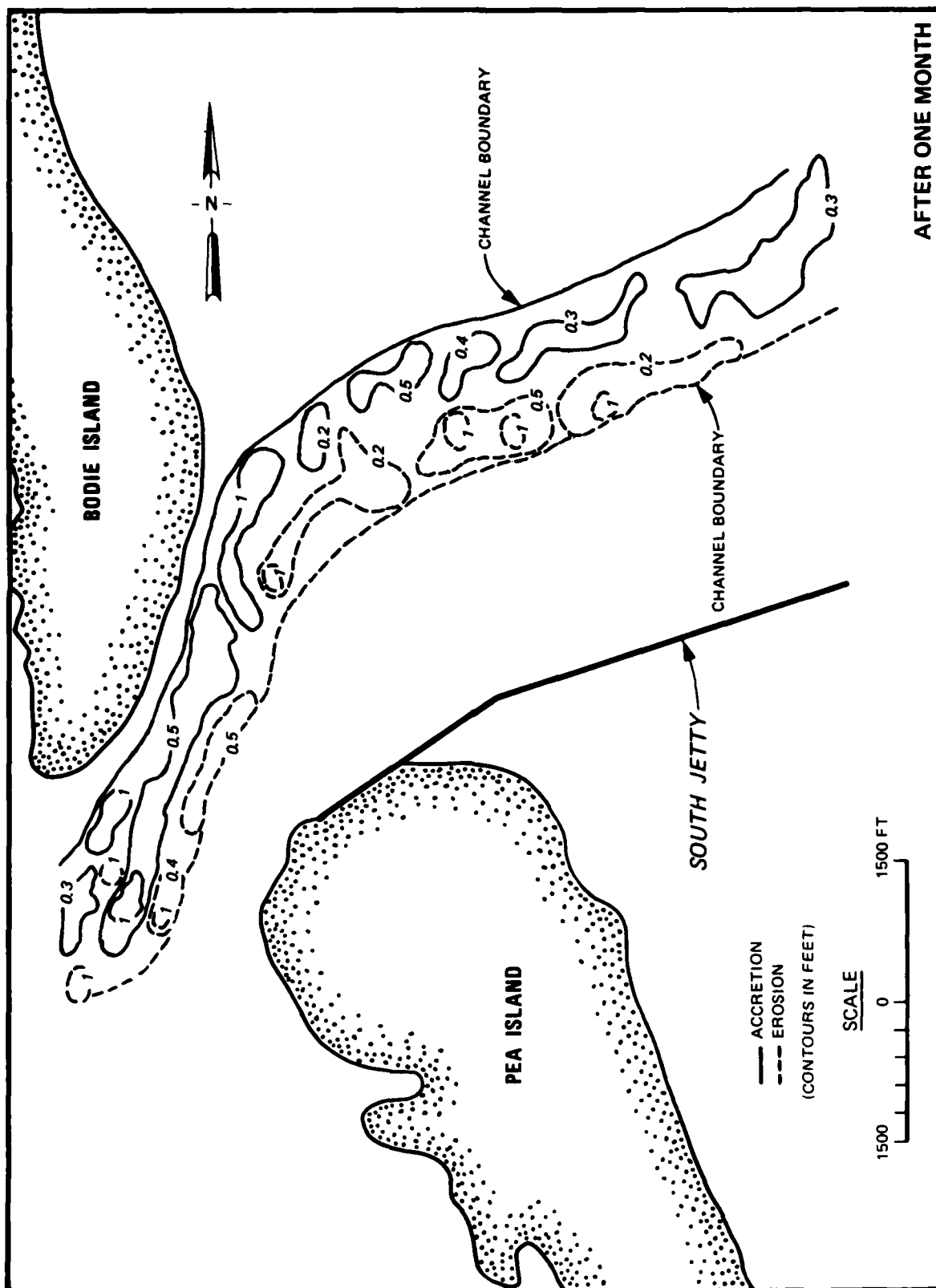
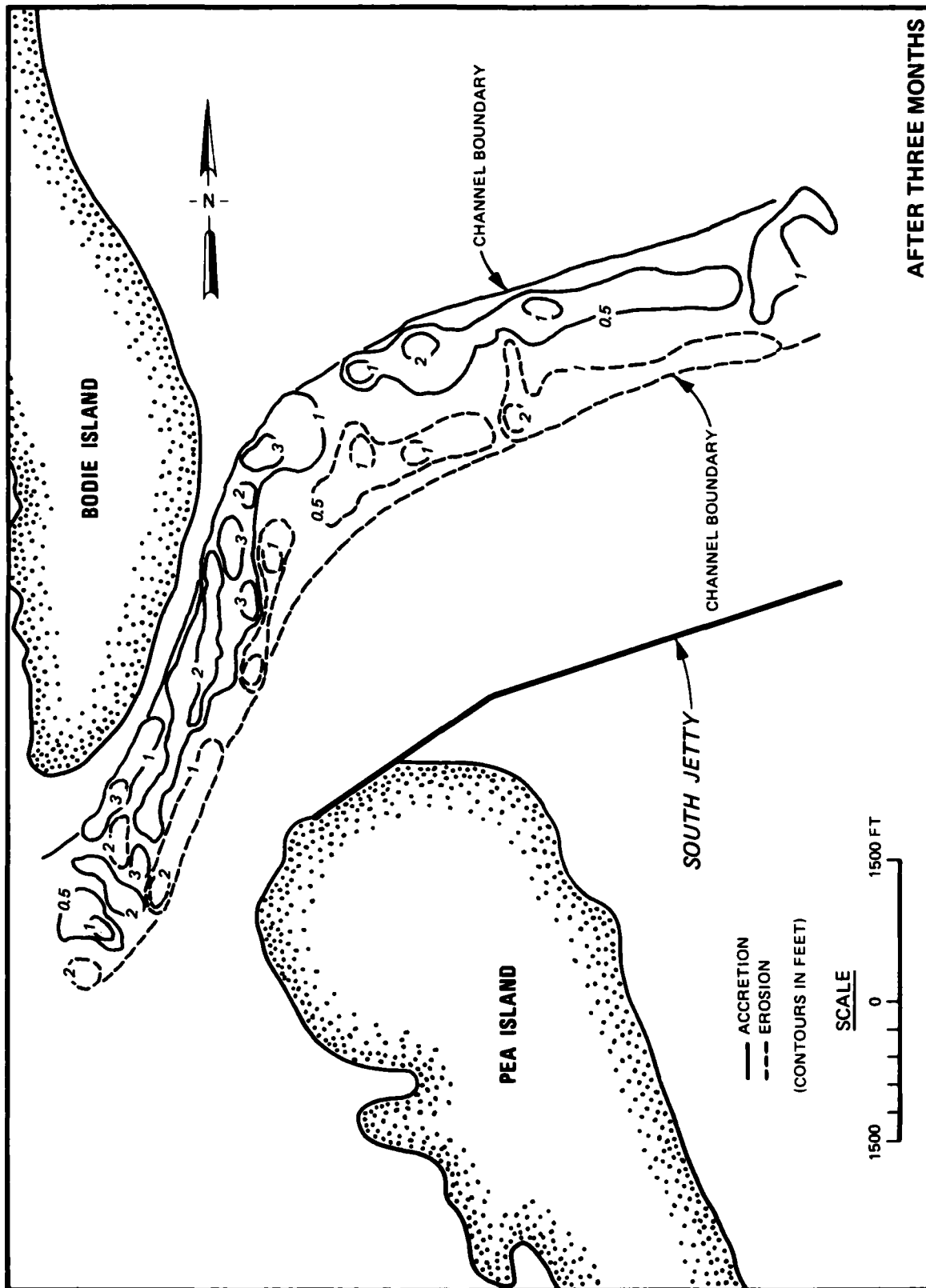


PLATE 3



AFTER ONE MONTH

PLATE 4



AFTER THREE MONTHS

PLATE 5

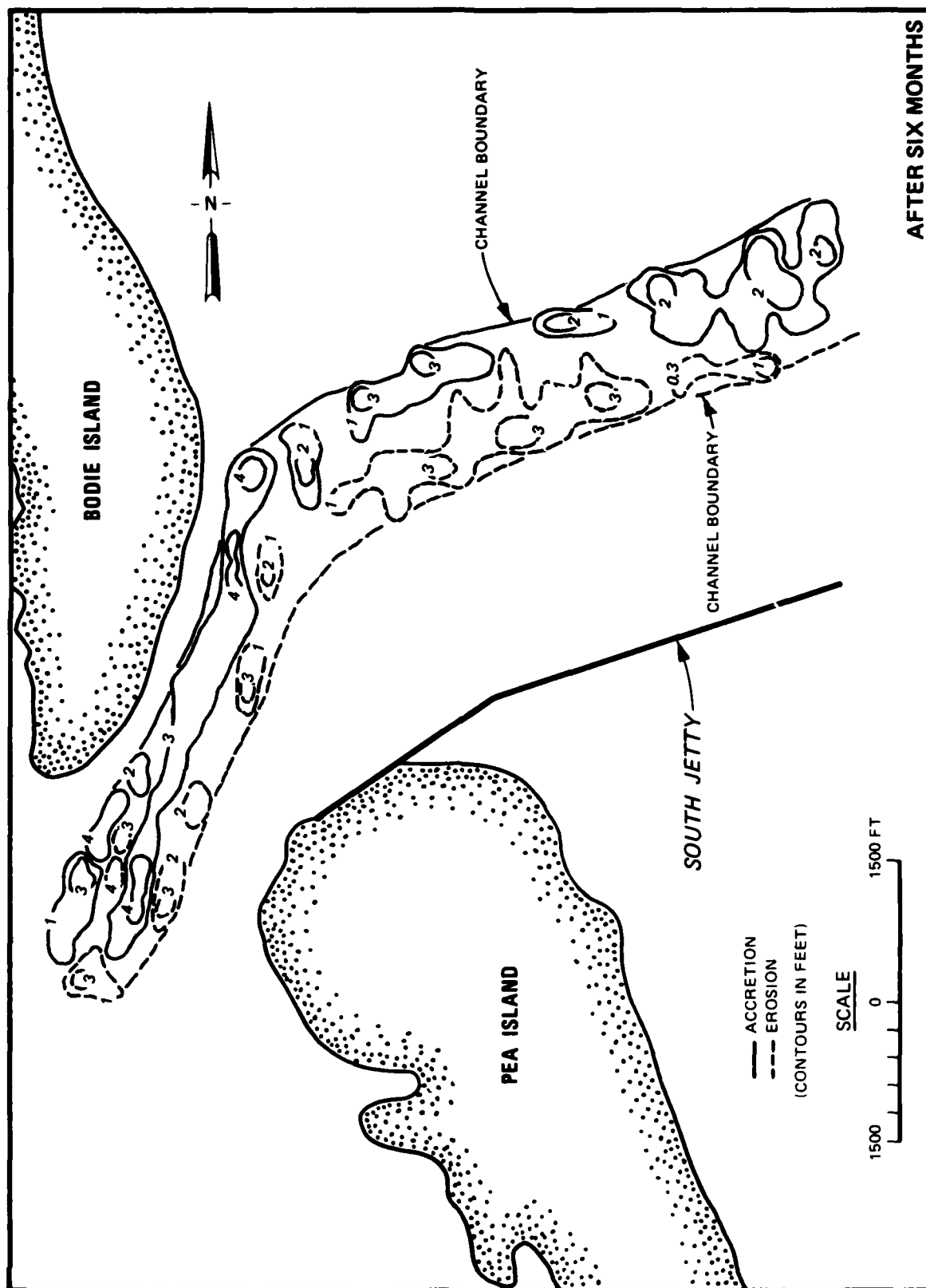
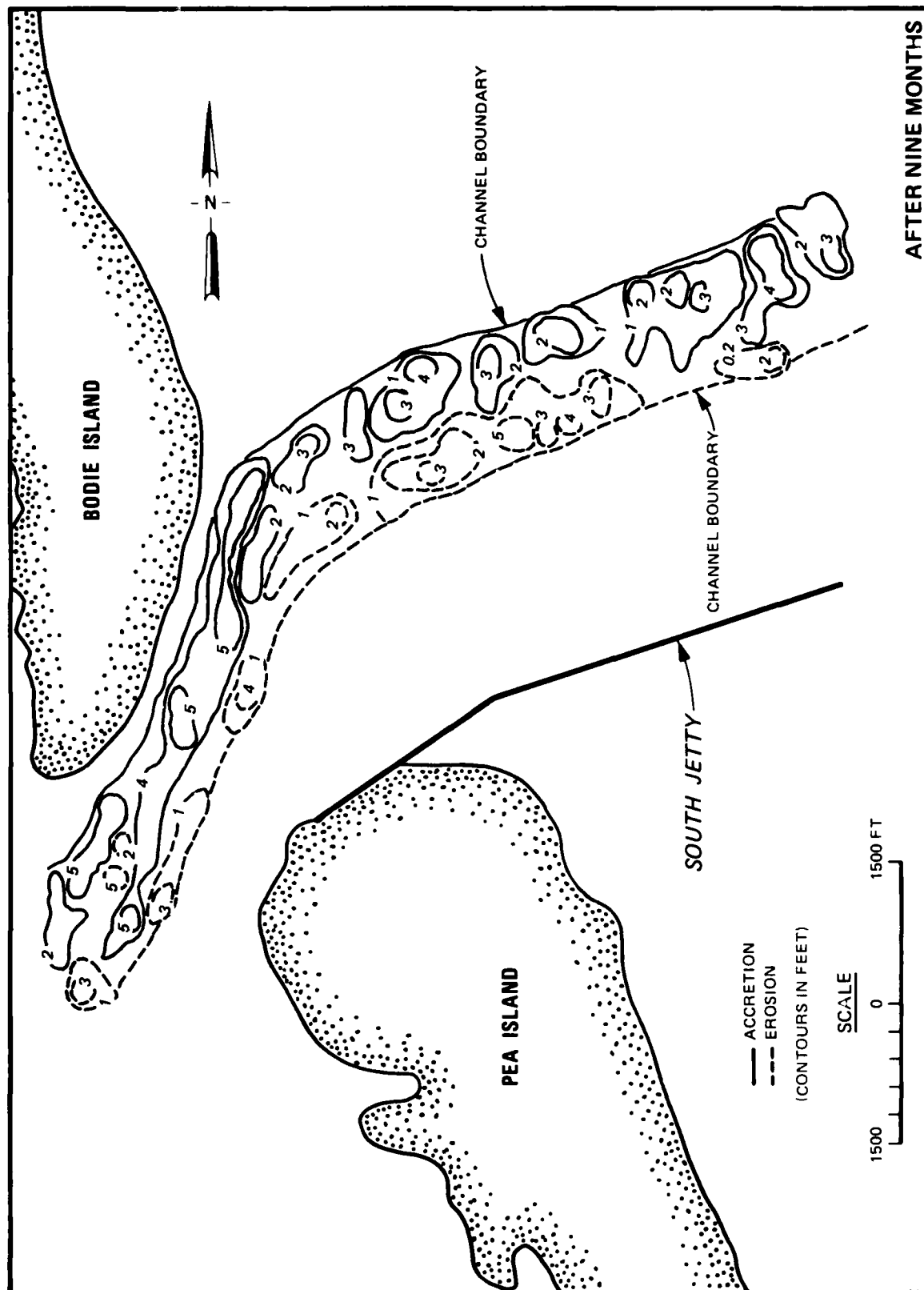


PLATE 6



AFTER NINE MONTHS

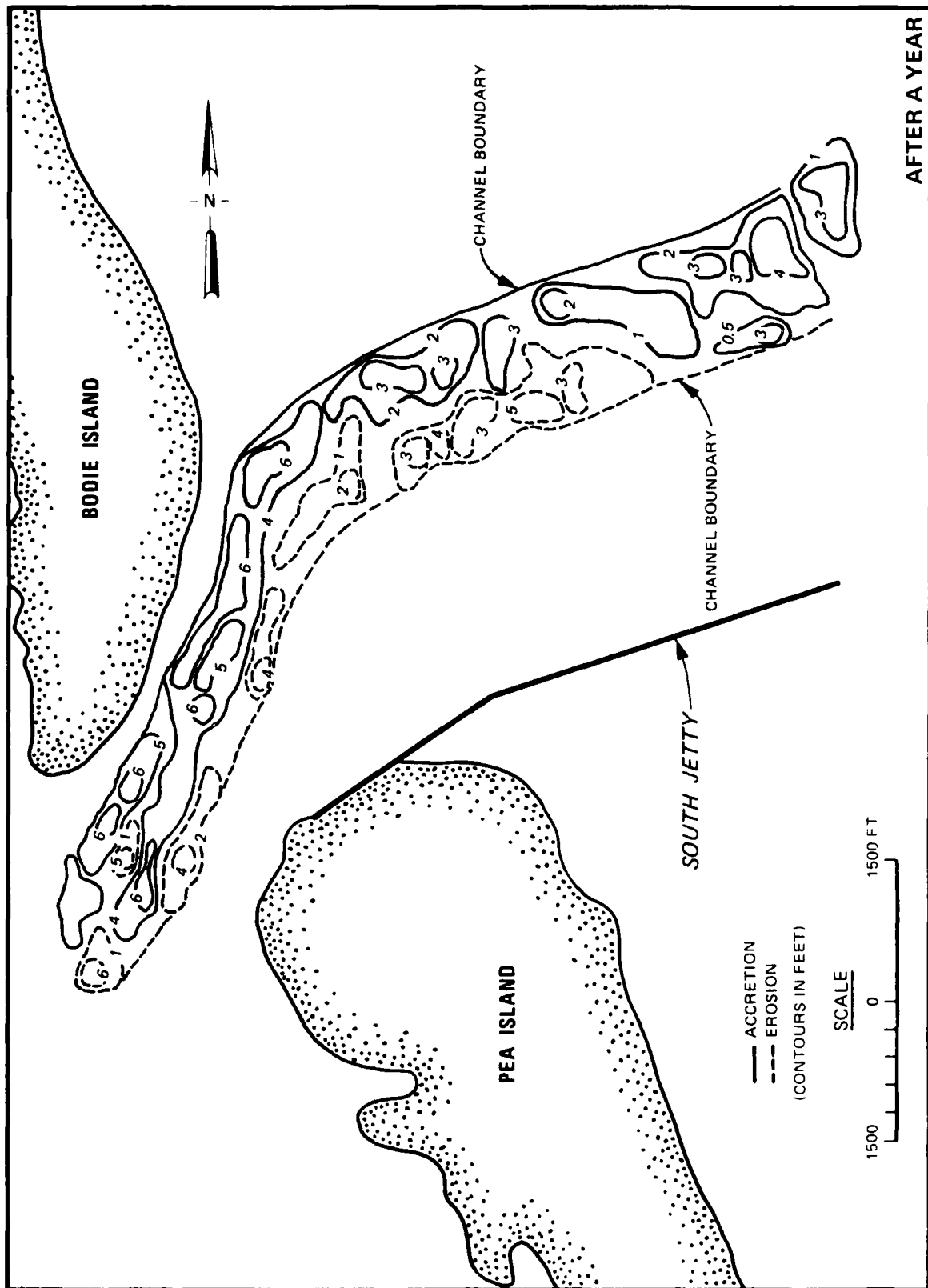
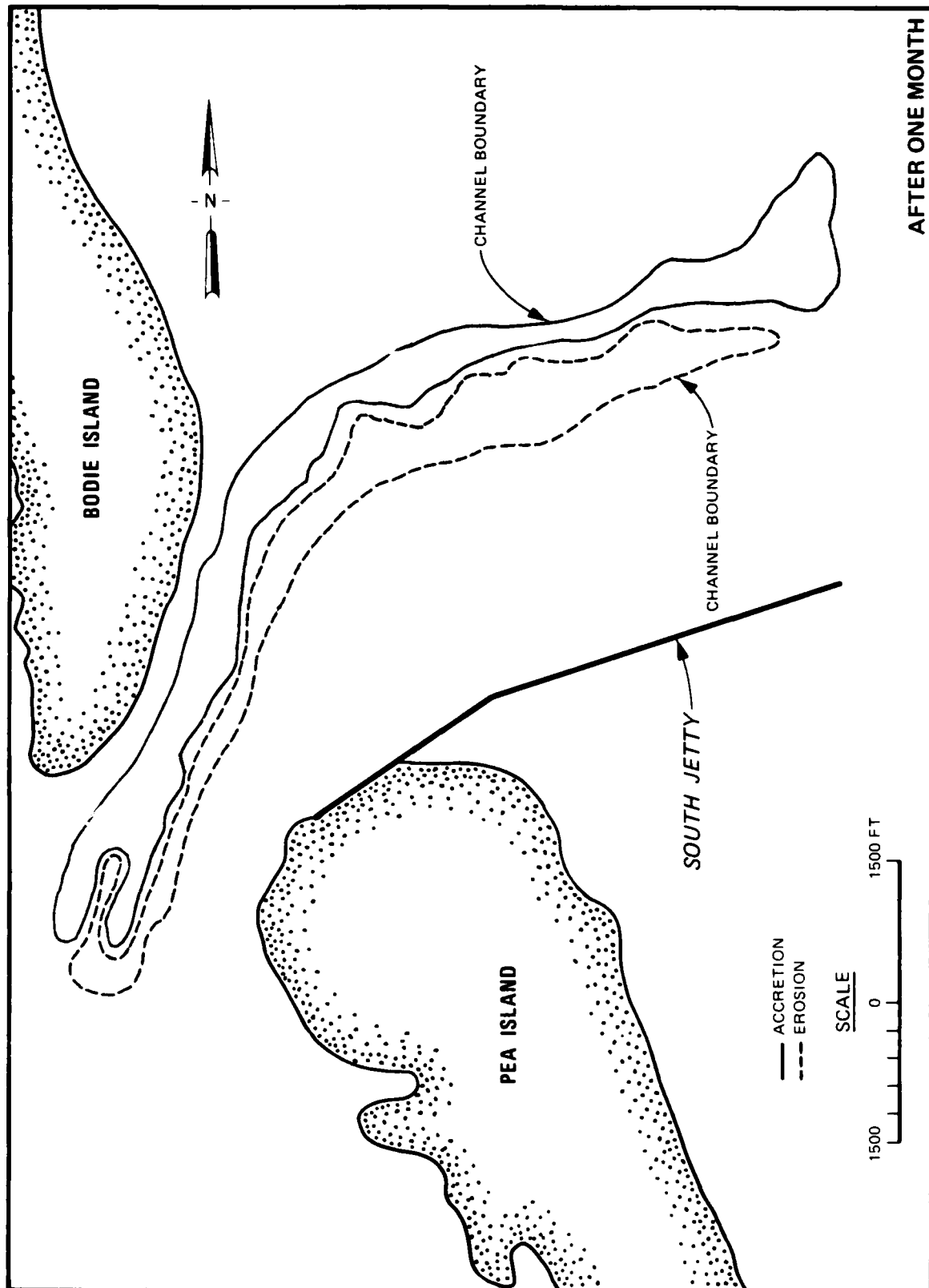


PLATE 8



AFTER ONE MONTH

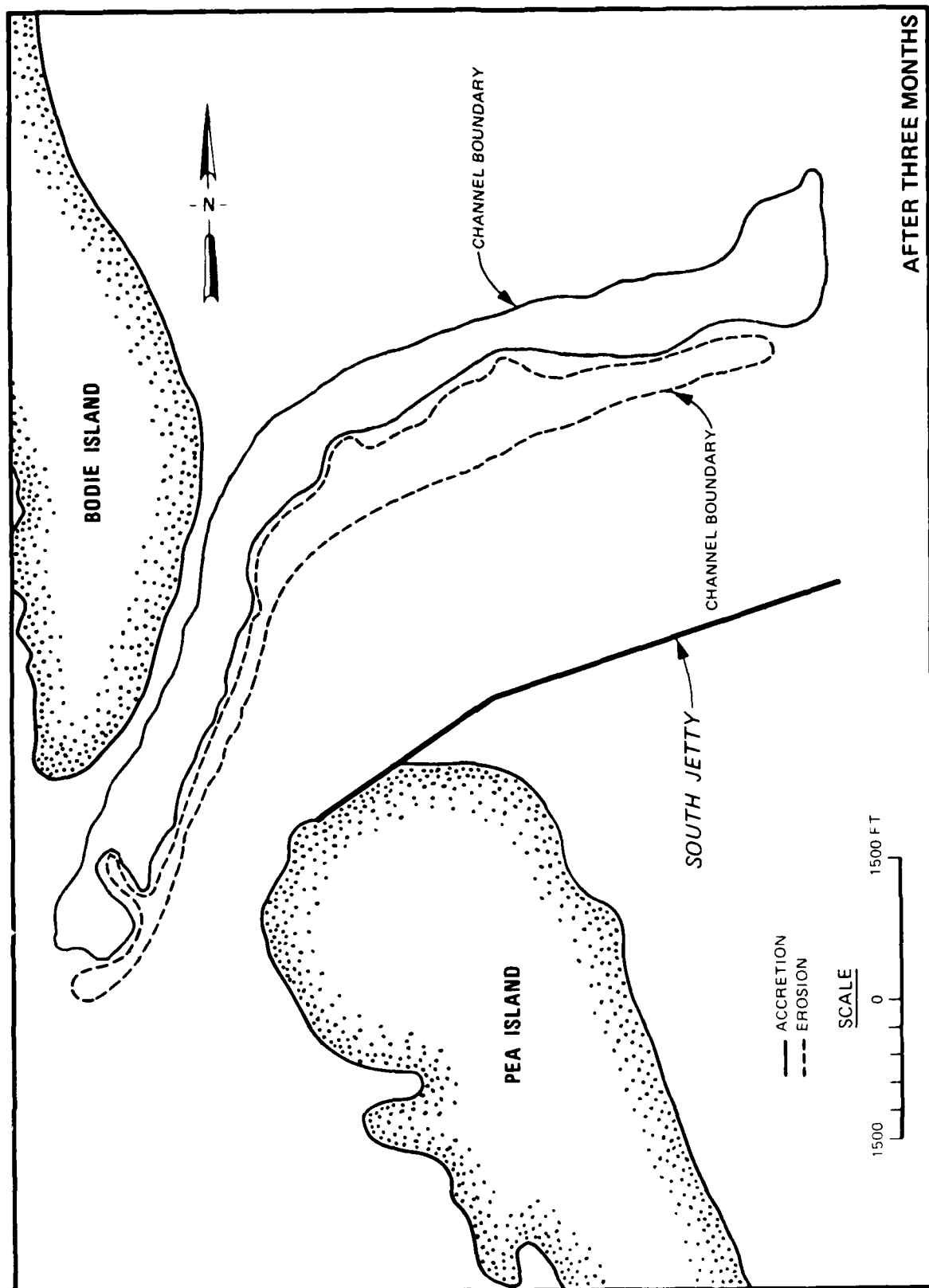


PLATE 10

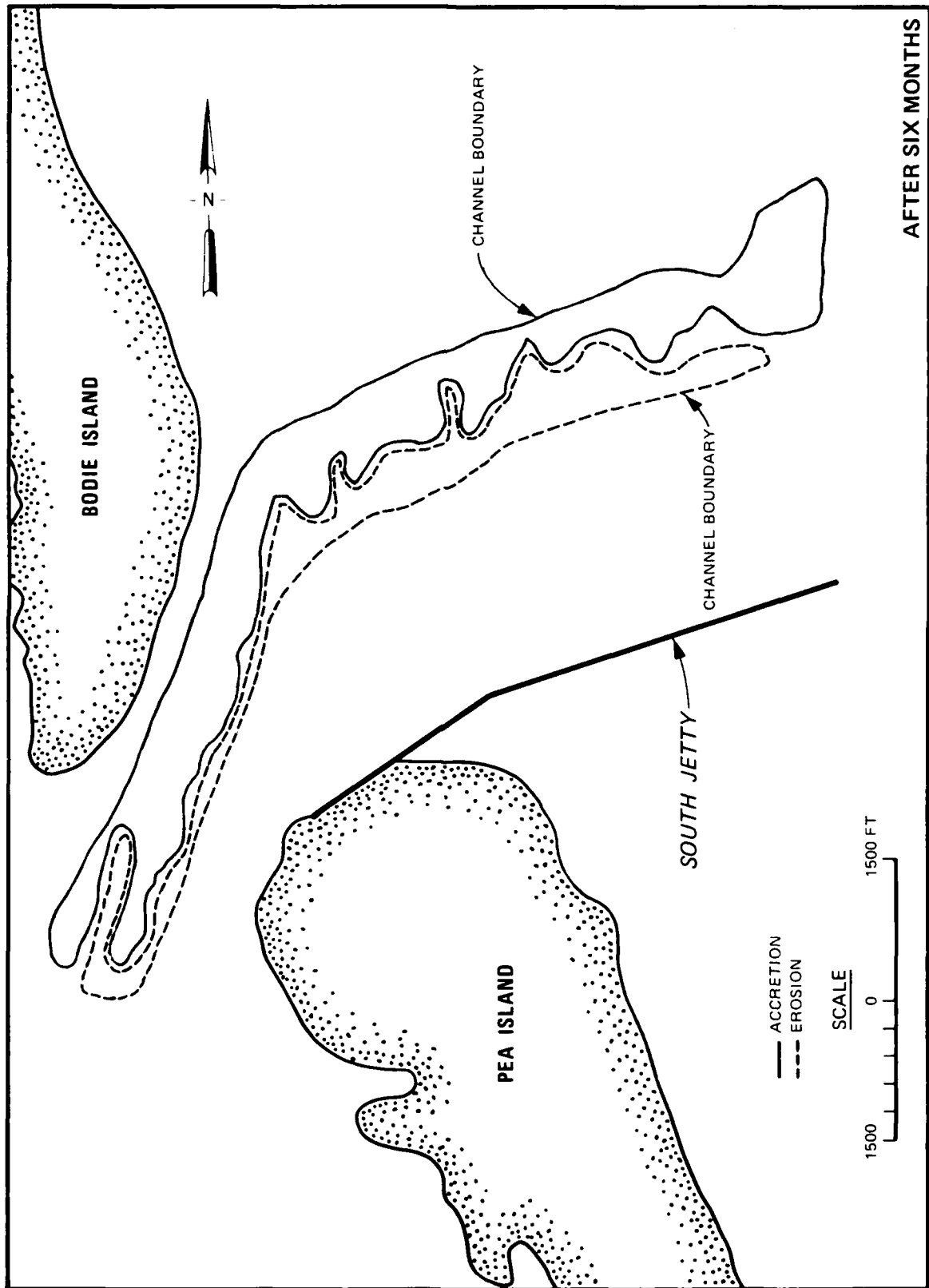
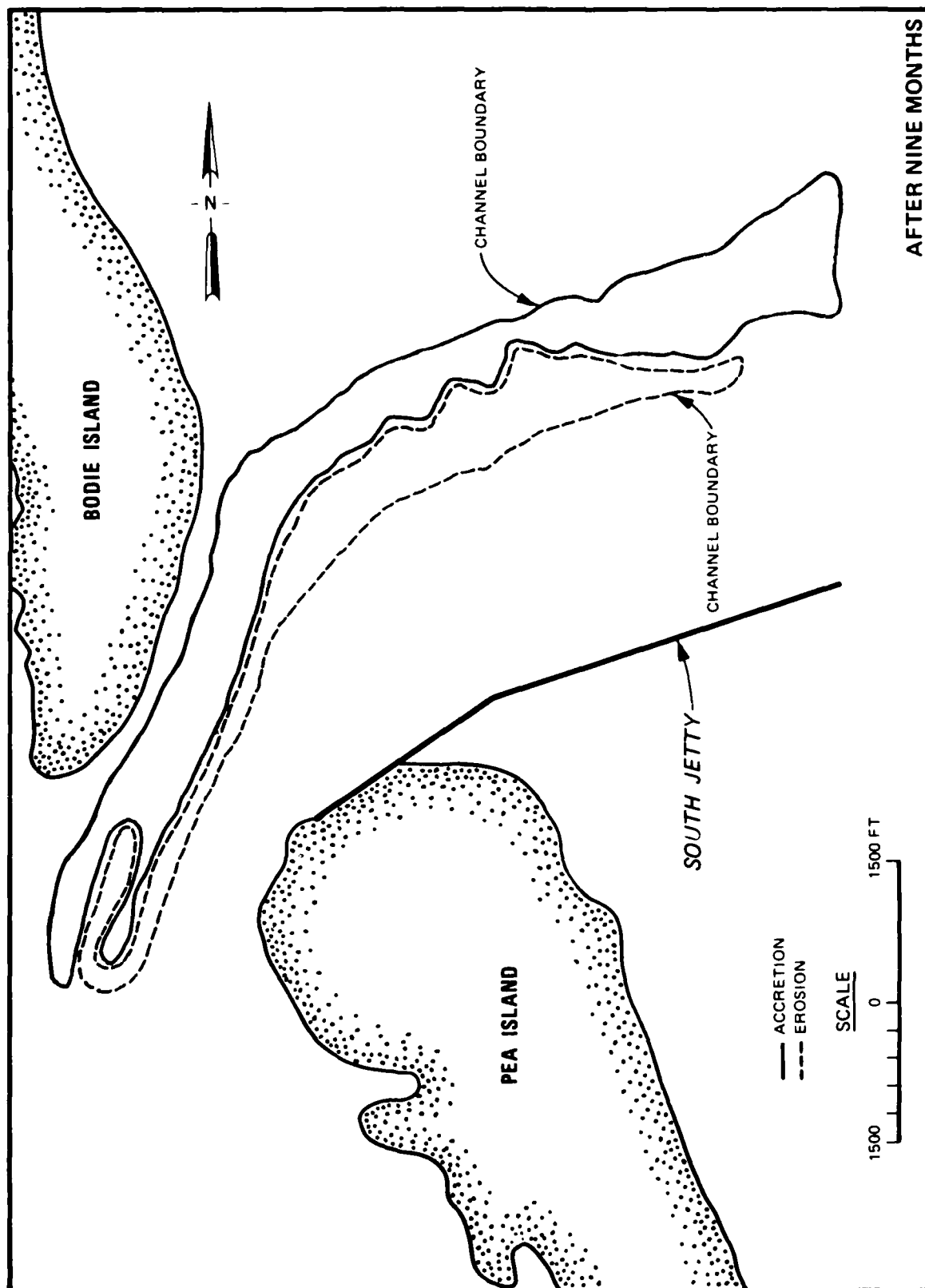


PLATE 11



AFTER NINE MONTHS

PLATE 12

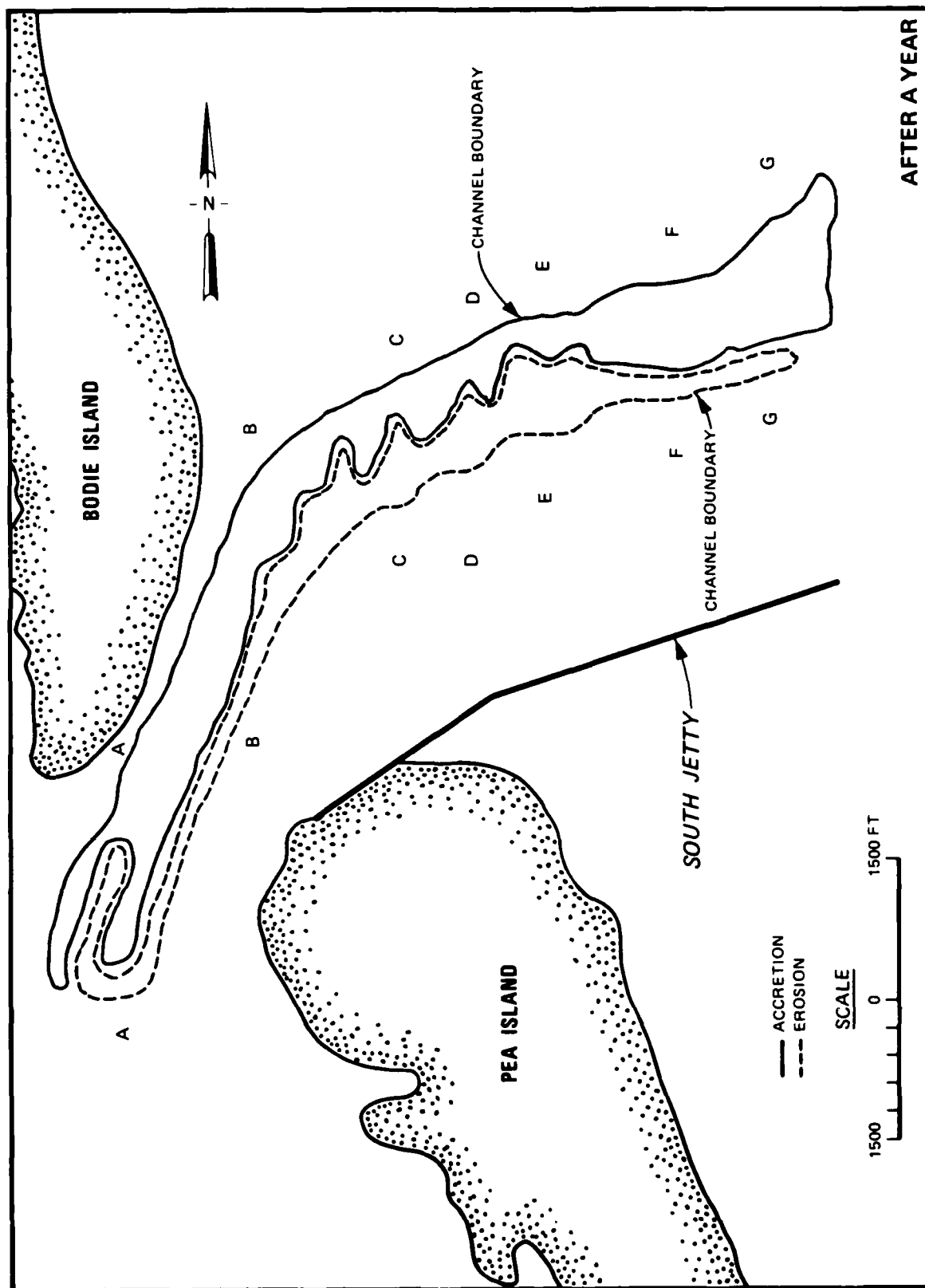


PLATE 13

APPENDIX A: NOTATION

a_p, b_p, c_p	Mapping constants for region p in x-direction
a_q, b_q, c_q	Mapping constants for region q in y-direction
A_c	Area off cell
c	Drag coefficient, wave celerity
C	Wave celerity, coefficient
C_g	Wave group velocity
C_h	Chezy coefficient
C_s	Average sediment concentration (dimensionless)
d	Local water depth
d_{new}	New water depth of a cell
D	Sediment diameter exceeded in size by 65 percent (by weight) of sediment sample
D_{50}	Median diameter of sediment
E	Wave energy density = $\rho g H^2 / 8$
f_w	Wave friction factor
f_{w1}	Wave friction factor based on bed roughness
f_{w2}	Wave friction factor with D as bed roughness
g	Acceleration due to gravity
h_i	Local still-water depth
h_m	Depth of point dividing the lower limit of D-profile and the upper limit of transition area
h_o	Position of maximum runup
H	Wave height
H_{mo}	Maximum wave height in the spectrum
i, j	Cell indices
k	Wave number
\vec{k}	Wave number vector

k_x, k_y	Components of wave number vector
L_{1i}	Length of onshore profile
L_{2i}	Length of offshore profile
m, n	Indices for cell center
$m-1/2$	
$m+1/2$	
$n-1/2$	
$n+1/2$	Indices for cell faces
M, N	Cell indices in FORTRAN
n	Ratio of group velocity to wave celerity, C_G/C
N	Empirical mixing coefficient of Longuet-Higgins
p	Porosity of sediment
P	Mixing parameter of Longuet-Higgins
P, Q, R, S	Recursion coefficients
Q_1	Total sediment transport rate across surf zone
r_1	Bed roughness
s	Arbitrary variable, mass density of sediment relative to that of fluid
S	Total sediment transport rate per unit width
$S_{i,j}$	Radiation stress
S_{xx}, S_{xy}, S_{yy}	Radiation stresses
S_{in}, S_{out}	Total sediment transport rates into and out of a cell
$(S_y)_{it}$	Sediment transport rate at position i at time t
t	Time
T	Wave period
T_0	Period of wave when there is no current
u_0	Wave orbital velocity at the bottom
$\langle u_{orb} \rangle$	Time average of the absolute value of the wave orbital velocity at bottom

u, v	Velocity components in x- and y-directions
\bar{v}	Mean velocity of flow, longshore current velocity at x
v_*	Shear velocity
\vec{v}	Current velocity vector
W_i	Value of $L_{2i} - L_{1i}$ for equilibrium
W_r	Value of W_i at still-water line
x, y	Coordinates in real space
x_b	Width of surf zone
X	Dimensionless coordinate, x/x_b
Y	Dimensionless grain diameter
Z	Arbitrary variable
α_1, α_2	Coordinates in computational space
β	Angle beach makes with the horizontal
γ	Breaking index
δ	Difference operator, total depth of D-profile
Δh	Change in bed elevation of a cell
Δ_r	Dimensionless position in D-profile
Δt	Time-step
$\Delta x, \Delta y$	Cell dimensions in real space
$\Delta \alpha_1, \Delta \alpha_2$	Cell dimensions in computational space
ϵ_x, ϵ_y	Eddy viscosities in x- and y-directions
$\bar{\eta}$	Mean free surface displacement
θ	Angle of wave propagation
θ_o	Wave direction in deep water
λ_o	Deepwater wave length
μ_x, μ_y	Grid expansion coefficients
ν	Kinematic viscosity of fluid

π	3.14159...
ρ	Mass density of sea water
$\bar{\sigma}_{xx}, \bar{\sigma}_{xy}$	
$\bar{\sigma}_{yx}, \bar{\sigma}_{yy}$	Dimensionless radiation stresses
τ_{bx}, τ_{xy}	Bottom friction stresses in x- and y-directions
τ_{xy}	Lateral shear stress due to turbulent mixing
ω	Radian frequency as it appears to a stationary observer
ω_0	Radian frequency when there is no current, $2\pi/T_0$

Superscripts

r-1	Previous time level
r	Present time level
r+1	Next time level
*	Intermediate time level

Subscripts

b	At breaking
t	Partial derivative with respect to time
α_1	Partial derivative with respect to α_1
α_2	Partial derivative with respect to α_2

END

FILMED

2-86

DTIC